Impacts of snow and surface conditions on radiation fluxes through Arctic sea ice during different seasons

Dissertation submitted by

Philipp Anhaus

in partial fulfilment of the requirements

for the degree of

Doctor of Natural Sciences (Dr. rer. nat.)

to

Faculty 01

Physics and Electrical Engineering

University of Bremen

Submission: 11 October 2021

Colloquium: 31 January 2022

Universität Bremen

ALFRED-WEGENER-INSTITUT
HELMHOLTZ-ZENTRUM FÜR POLAR- UND MEERESFORSCHUNG

1. Reviewer:

Prof. Dr. Christian Haas

Alfred Wegener Institute, Helmholtz Centre for Polar and Marine Research, Bremerhaven

University of Bremen

2. Reviewer:

Prof. Dr. Torsten Kanzow

Alfred Wegener Institute, Helmholtz Centre for Polar and Marine Research, Bremerhaven

University of Bremen

This dissertation was written at the Sea Ice Physics section of the Alfred Wegener Institute, Helmholtz Centre for Polar and Marine Research, Bremerhaven.

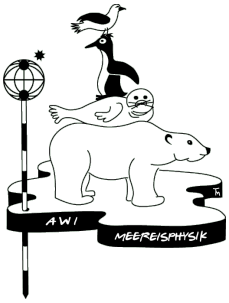

Abstract

Sea ice and its snow cover play a key role within the climate and ecosystem. Due to global environmental changes which are amplified in the Arctic Ocean, its sea-ice cover will primarily consist of thin and young sea ice with a reduction in extent. In particular, the area where snow accumulates reduces and the fraction of melt-pond covered sea ice and of openings in the sea-ice cover such as leads increase. Those changes of the surface conditions strongly influence the partitioning of solar radiation.

The main objective of this dissertation was to establish relationships between the surface conditions that are observed and expected to dominate in the future Arctic and under-ice radiation. A deeper and broader knowledge of such relationships is especially necessary in spring and autumn during which the under-ice radiation can have significant impacts on the annual energy budget. To achieve that, field measurements collected using a variety of instruments during three campaigns for three different sea-ice types, locations, and seasons were analysed and interpreted.

A main result was to derive a new parametrization for snow depth retrieval from spectral under ice-radiation measurements. This was successfully achieved with an accuracy of approximately 5 cm for two ice types, in two locations, during two seasons.

In contrast to the established theory that melt ponds act as bright windows to the underlying ocean, it was possible to document and analyse cases where a thicker snow cover accumulated on melt ponds compared to on adjacent bare ice. This resulted, surprisingly, in lower levels of under-ice radiation underneath the melt ponds than underneath bare ice.

New analyses of relationships between thermodynamics and optics of a refreezing lead and thin ice suggest that radiative transfer in thin ice is often not accurately accounted for using bulk formulations, as they are applicable for thicker ice. The initial states of the lead's opening and refreezing need to be treated separately and cannot generally be considered windows into the ocean. This dissertation extended our knowledge of the relationships between snow and surface conditions and under-ice radiation. The results point towards impacts on sea-ice energy balance, ocean heat content, thermodynamic ice growth, and ice-and ocean-associated ecosystem activity.

Contents

1. Dissertation - Motivation and outline

1.1 Arctic sea ice

Sea ice (**Figure 1.1**) forms from the saline seawater in the polar seas when sufficient heat is extracted from the ocean towards the atmosphere (Petrich and Eicken, 2017). The inclusion of salts makes the physical properties of sea ice different from those of lake ice. Due to its lower density compared to the surrounding seawater, sea ice floats partly above the sea level (freeboard) and partly below (draft). Studies concerning sea ice covering the Arctic Ocean and the surrounding seas have increased dramatically in the last 20 years. The more knowledge is gathered the more crucial those studies become.

Sea ice is playing an important role in the Earth's climate. Its surface reflects much more solar radiation back towards the atmosphere than dark open water or most land areas (Roedel and Wagner, 2011). The amount of radiation that is reflected increases significantly when a snow cover overlies the sea-ice surface (e.g., Grenfell and Maykut, 1977). Thus, sea ice plays a key role in partitioning of radiation and therefore in the energy balance of the Earth (e.g., Church et al., 2011; Persson and Vihma, 2017). Amongst the heat and energy fluxes at its interfaces with the ocean and the atmosphere, sea ice also controls salt, mass, moisture, and momentum fluxes across those interfaces (Kaartokallio et al., 2017; Persson and Vihma, 2017; Petrich and Eicken, 2017).

Sea ice regulates deep water formation through salt rejection, which is important to maintain the thermohaline circulation of the world's oceans (e.g., Aagaard et al., 1985). Heat input to the Arctic Ocean, ocean circulation, and mixing are also affected by sea ice (e.g., Carmack et al., 2015). The Arctic sea ice is habitat to a diverse number of animals such as polar bears and whales, seals, fishes, and birds as well as flora (e.g., Hovelsrud et al., 2008; Kovacs and Lydersen, 2008; Kovacs et al., 2012; Sahanatien and Derocher, 2012; Meier et al., 2014). Sea ice is also very important for the sea-ice- and ocean associated ecosystem such as algae and phytoplankton. These mostly live at the very bottom of the ice where growing takes place and where the

Figure 1.1: *Sea ice in different locations and seasons. (**A**) Central Arctic, March, (**B**) Baffin Bay, July, (**C**) Marginal Ice Zone, May, and (**D**) Central Arctic, September.*

conditions for life are most suitable (Arrigo, 2014; Meier et al., 2014). Indigenous peoples living in the Arctic depend on sea ice as a platform for hunting, fishing, and transportation, and thus, rely on the sea-ice properties and their changes (e.g., Hovelsrud et al., 2008; Pearce et al., 2010; Ford and Goldhar, 2012). In an economic view, sea ice influences shipping, off-shore infrastructure, fishing, tourism, and fossil resource extraction (oil and gas) (e.g., Meier et al., 2014; Eguiluz et al., 2016; Aksenov et al., 2017). Considering the recent loss in the sea-ice cover, it may be possible to open up a new trading route from Europe to Asia and get access to the reservoir of fossil resources (e.g., Meier et al., 2014).

1.2 The changing Arctic sea-ice cover

The sea-ice cover in the Arctic Ocean has experienced a dramatic decline in the last decades (e.g., Perovich, 2011; Meier et al., 2014; Meredith et al., 2019). Sea-ice extent is shrinking (Serreze et al., 2007; Stroeve et al., 2007, 2012), thickness is decreasing (e.g., Haas et al., 2008; Kwok and Rothrock, 2009), and perennial old multi-year ice (MYI) is replaced by seasonal first-year ice (FYI) (e.g., Maslanik et al., 2007; Stroeve and Notz, 2018). Because of the shift from old, thick MYI to seasonal, thin FYI, the sea-ice cover has become less robust and more sensitive to thermodynamic and dynamic forcing (e.g., Maykut, 1986; Rampal et al., 2009).

The changes in the Arctic sea-ice cover are the most prominent signals of global warming (e.g., Meredith et al., 2019). Those changes are responses to warm anomalies in the Arctic (e.g.,

Overland et al., 2008), to the preconditioning of the ice (e.g., Lindsay et al., 2009), to changes in atmospheric circulation (e.g., Makshtas et al., 2003) and ice motion (e.g., Rampal et al., 2009), to shifts in the cloud cover (e.g., Schweiger et al., 2008), to advected ocean heat (e.g., Polyakov et al., 2010), and to the ice albedo feedback (Perovich et al., 2008).

The ice albedo feedback is a highly relevant mechanism for the partitioning of solar radiation and amplifies the decline of the sea-ice cover. Due to the shrinking sea-ice extent, the fraction of open water areas increases. This leads to a higher amount of radiation being absorbed by open water due to the low albedo (Perovich, 1996). By the same token, enhanced ocean warming increases melting and extends the areas of open water even further (e.g., Perovich et al., 2008). In general, the amount of heat deposited into the ocean compared to the total heat input into the ice-ocean system has been observed to increase (Perovich, 2011; Arndt and Nicolaus, 2014). At the same time, the area where snow deposits and accumulates is shrinking. Due to the snow's important role as a strong reflector (Grenfell and Maykut, 1977) and insulator (e.g., Sturm et al., 1997), both the sea-ice energy and mass balance are influenced. Especially because of its important role in partitioning radiation, snow plays a key role in the sea-ice and global climate. Thus, the need to monitor and assess the snow depth distribution, which is constantly changing through space and time, is steadily increasing, in particular during autumn when most snow fall occurs and during spring where snow depth is maximal (Warren et al., 1999).

During summer, Arctic sea ice is covered with melt ponds of different sizes and depths which develop as a response to surface melt (e.g., Webster et al., 2015). The melt pond coverage has been observed to increase (Perovich et al., 2009; Schröder et al., 2014). Melt ponds also play an important role in the partitioning of solar radiation as they absorb and transmit a considerable amount of radiation (Light et al., 2008; Ehn et al., 2011; Frey et al., 2011; Nicolaus et al., 2012; Katlein et al., 2015; Light et al., 2015). This enhances the need for further investigations on the effects of melt ponds on the energy budget of sea ice in the changing Arctic Ocean.

Due to the, in a mechanical sense, weaker sea-ice cover and increasing drift speed of sea ice, more frequent and severe dynamic events are observed (Itkin et al., 2017). This fosters the sea-ice to break and diverge, and subsequently result in an increase in the occurrence of openings in the sea-ice cover, such as leads, polynyas, and cracks. Leads are linear features of open water that can occur in every season when the sea-ice cover breaks. Their existence is short as new sea ice forms quickly. Besides high transmittance of leads (e.g., Perovich, 2005; Taskjelle et al., 2016; Kauko et al., 2017) which is relevant for the ecosystem and mass and energy balance of the sea ice, leads are very important for exchanges of fluxes between the ocean and the atmosphere (Maykut, 1982; Perovich et al., 2011a). Thus, the dependencies between physical properties, such as ice thickness, and optical properties, such as transmittance, for refreezing leads need to be investigated to be able to assess and monitor the effects of leads on sea ice in a changing Arctic Ocean in more detail.

1.3 Scope and outline

In the changing Arctic Ocean, the snow cover shrinks in response to the declining sea-ice extent, the fraction of sea ice covered by melt ponds increases, and the occurrence of leads and subsequently thin ice becomes more frequent. Driven by the strong influence of snow depth, melt ponds, and leads and thin ice on the under-ice radiation, this dissertation takes on the task to establish and investigate the relationships between those surface conditions and properties and under-ice radiation. Another focus lies on the shoulder seasons spring and autumn in which in particular the timing of the seasonal progression in the under-ice radiation can have significant impacts on the annual energy budgets (Arndt and Nicolaus, 2014; Schröder et al., 2014; Flocco et al., 2015; Perovich, 2017; Katlein et al., 2019). While measurements of the optical properties of sea ice are abundant in summer in the central Arctic, gaps exist especially in spring and in areas outside the central Arctic. This emphasizes the need for a better understanding of spring and autumn sea-ice processes.

The **overarching goal** of this dissertation is to broaden and deepen our knowledge of the relationships between sea-ice surface conditions and properties that are predicted to dominate in the future Arctic Ocean and under-ice radiation during spring and autumn. In particular, three objectives are outlined which guide in achieving this goal:

First objective (Chapter 3): Establish relationships between snow depth and spectral under-ice radiation, which are applied and validated to retrieve snow depth from spatial and continuous measurements of under-ice radiation.

Second objective (Chapter 4): Document and investigate the effect of refrozen and snow-covered melt ponds on the under-ice radiation and compare results to the situation for adjacent bare ice.

Third objective (Chapter 5): Examine the connection between thermodynamics and optics of a refreezing lead and thin ice in comparison to the under-ice radiation of heavily snow-covered and thick second-year ice (SYI).

Chapter 4 of this dissertation provides an overview of the theoretical background on solar radiation partitioning, sea-ice optical properties, and sea-ice mass balance as well as an introduction to the key instruments used. **Chapter 3** addresses the relationship between snow depth and under-ice radiation. Investigations are performed for land-fast FYI in the Lincoln Sea in late spring 2018 and for drifting, melt-pond covered MYI in the central Arctic close to the geographic North Pole in the transition from summer to autumn in 2018. In particular, two new inverse methods are developed to retrieve the snow depth from under-ice radiation measurements. Those methods can be applied to remotely and autonomously measured under-ice radiation

for which simultaneous measurements of snow depth are often lacking. **Chapter 4** investigates the effect of snow-covered refrozen melt ponds on the transmitted radiation for a drifting, melt-pond covered MYI floe in the central Arctic close to the geographic North Pole in the transition from summer to autumn in 2018. Melt ponds usually have a recessed topography compared to adjacent bare ice. Within those surface depressions, more snow can accumulate than on adjacent bare ice once the melt ponds are refrozen. Such scenarios have been observed in the past, however, no documentations exist describing the influence of the thicker snow cover of melt ponds on the under-ice radiation. The research performed in Chapter 4 closes this gap and presents relevant measurements under the hypothesis that the thicker snow cover on the melt ponds lead to a reduction in the under-ice radiation. Additionally, a discussion is led about potential implications of this hypothesis on the autumn ecosystem activity, oceanic heat budget, and thermodynamic ice growth. **Chapter 5** presents the evolution of a refreezing lead and of thin ice in the central Arctic in spring 2020. The thinning and younger seasonal ice of the new Arctic is more vulnerable to dynamic events. It is expected that the occurrence of leads increases. The solar heat input into the ocean through the leads is enhanced. Thin ice can strongly affect the ecosystem, decrease the albedo, and trigger bottom melt of adjacent sea ice. Thus, it is important to establish relationships between the refreezing, thickening ice formed in the lead and the transmittance. In **Chapter 6**, this dissertation is closed, the key findings are presented, and ideas for possible future field campaigns and research that can extend this dissertation are provided.

1.4 Publications within this dissertation

Chapters 3 and 4 of this dissertation represent publications in leading scientific journals. Slight modifications in those chapters have been made compared to the submitted versions to follow a uniform layout and structure within this dissertation. This included re-organizing references within the text, correcting typos, and adjusting text and figures so that they are aligned with the structure of this dissertation, e.g. British English. In particular, DOIs of some data sets used in Chapters 3 and 4 are now available. Supplementary figures and tables used in the published version of Chapter 4 were included in the main text in this dissertation.

Publication 1 (Chapter 3)

Anhaus, P., Katlein, C., Nicolaus, M., Arndt, S., Jutila, A., and Haas, C. (2021): Snow Depth Retrieval on Arctic Sea Ice Using Under-Ice Hyperspectral Radiation Measurements, *Frontiers in Earth Science, 9*, doi:10.3389/feart.2021.711306.

Publication 2 (Chapter 4)

Anhaus, P., Katlein, C., Nicolaus, M., Hoppmann, M., and Haas, C. (2021): From bright windows to dark spots: Snow cover controls melt pond optical properties during refreezing, *Geophysical Research Letters, 48*(23), doi:10.1029/2021GL095369.

Planned publication 3 (Chapter 5)

Preliminary author list: Anhaus, P., Katlein, C., Nicolaus, M., Arndt, S., and Haas, C.: Evolution of the light field under a refreezing lead in spring. The content of this chapter was presented during the international MOSAiC conference/workshop which took place online.

2. Theoretical background

2.1 Solar radiation partitioning and sea-ice optical properties

This section describes the partitioning of solar radiation due to sea ice, the radiative transfer within sea ice, the optical properties of sea ice, and the surface energy budget of sea ice. It closely follows the summaries from Mobley (1994), Perovich (1996), and Perovich (2017).

2.1.1 Overview

In sea-ice optics, only the electromagnetic radiation from the sun in the wavelength (λ) range from 200 nm to 2500 nm (short-wave) is considered. This part of the spectrum is further divided into five sub-ranges: Ultraviolet-C (UV-C, 200-280 nm), Ultraviolet-B (UV-B, 280-320 nm), Ultraviolet-A (UV-A, 320-400 nm), visible (380-780 nm), near-Infrared (near-IR, 750-2500 nm). The radiometers used in this dissertation measure radiation for the wavelengths 320 nm to 950 nm. However, the radiation measurements presented are either for 350 nm to 920 nm or for 400 nm to 700 nm, with the latter range defining the photosynthetically active radiation (PAR). The partitioning of incident solar radiation by the sea ice, different sea-ice types and surface conditions as well as relevant processes for the energy and mass balance are exemplified in **Figure 2.1**. Solar radiation reaches the Earth´s surface both as a direct beam component from the sun and a diffuse component from the sky and clouds. The sky and surface conditions highly influence the partitioning of the radiation. Incident radiation is specularly and diffusely reflected by the sea ice, snow, and open water. It is also scattered by a surface-scattering layer (SSL) (Perovich and Grenfell, 1982) and snow (Perovich, 1990). In turn, the radiation warms the surfaces contributing to surface and bottom melting also due to absorption by melt ponds. Radiation penetrating into the sea ice is further scattered by inclusions such as soot and sediments as well as air bubbles and brine (Light et al., 2008). Ice-algae, which are mainly present in the middle of the sea ice and at its bottom absorb radiation and thereby warm the interior ice (Arrigo, 2014).

Due to the processes at the surface and within the sea ice, the magnitude of the radiation is attenuated and its spectral shape changed, before it is transmitted through the sea ice

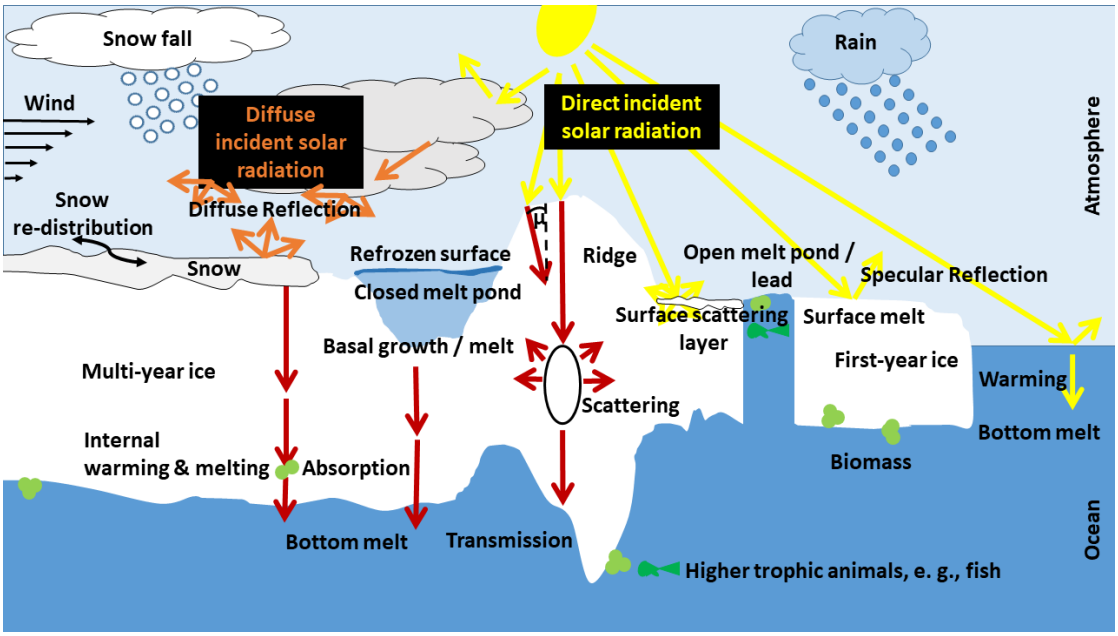

Figure 2.1: *Schematics of the snow and sea ice processes on Arctic sea ice and the radiative transfer in sea ice. μ is the cosine of the zenith angle Θ of the sun.*

into the underlying ocean. The transmitted radiation affects the ice mass balance through warming and melting the bottom sea ice, through warming the upper ocean, and influences primary productivity and other biological and biogeochemical processes in and under the sea ice (SooHoo et al., 1987).

In the following paragraphs, details on how solar radiation is measured and how the shortly outlined processes and dependencies above partition solar radiation are described.

2.1.2 Radiometry

Radiometry aims to describe how electromagnetic radiation can be measured. The solar radiation enters the Earth´s surface from all directions so that the total energy per unit time is proportional to the spherical surface of the Earth, that is $4\,\pi\,r^2$. The energy per unit time per unit area of our spherical Earth is the irradiance. It decreases with the inverse of the radius, r^{-2}. The magnitude and spectral composition of the incident spectral solar irradiance $E_S\,(\lambda)$ that the Earth´s surface receives from the sun depend on the zenith angle (time of day, latitude) and atmospheric condition and composition (humidity, dustiness, number and concentration of aerosols, cloud cover).

The irradiance highly depends on the sun's position relative to the horizon which is determined by season and geographic location. **Figure 2.2** shows incident irradiance spectra as measured in different locations and seasons in the Arctic. The maximum irradiances are received at

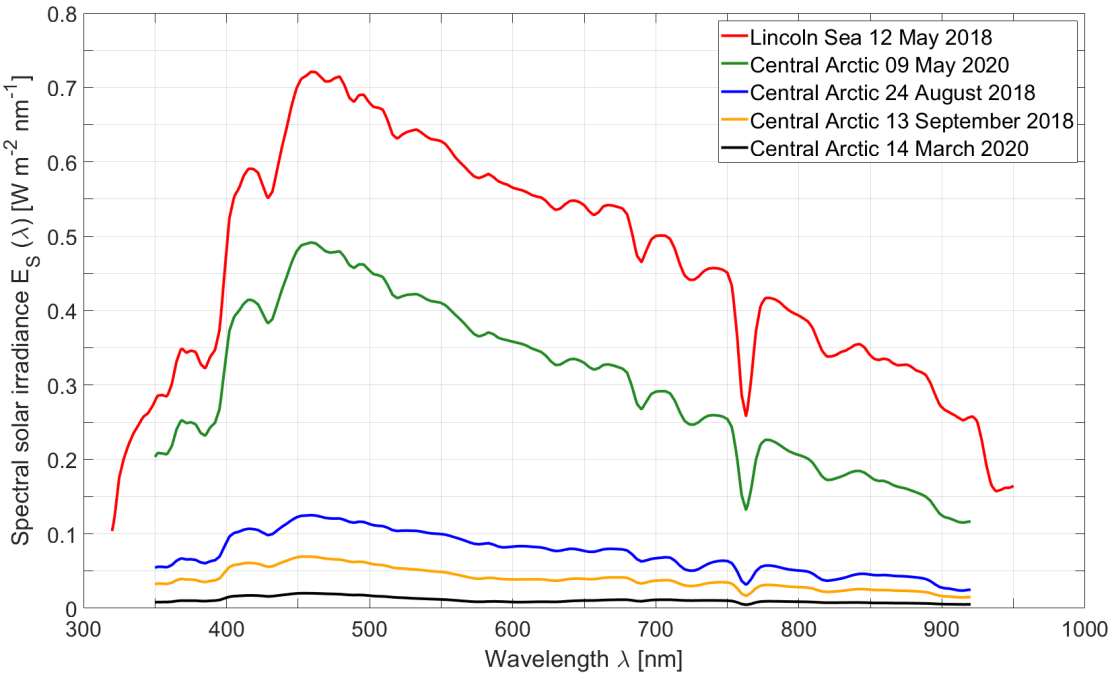

Figure 2.2: *Measured spectral solar irradiance during day time in different locations and seasons in the Arctic. The resolution on the x-axis is 1 nm.*

wavelengths between 400 nm and 480 nm. A prominent feature in the spectral irradiance at around 760 nm is one of the water vapour absorption bands (Roedel and Wagner, 2011).
In those examples, the irradiance integrated over all wavelengths (broadband) ranges from 6 W m^{-2} to 290 W m^{-2}. In the beginning of March, sunlight in the Arctic has just started to come back. While from May to July, the Arctic receives a maximum in irradiance, the irradiance decreases again throughout August and September towards zero in the Arctic winter. The Lincoln Sea is further south and thus, receives more irradiance in May than the central Arctic.

The irradiance can be detected and measured with quantum devices that react directly on the number of photons. In this dissertation, photoelectric devices with a photodiode are used. A silicon photodiode exists of a pn-junction (p: positive, n: negative) with the p-type silicon serving as an anode and the n-type as a cathode. The irradiance incident on the junction frees electrons from the silicon atoms. This results in positively charged silicon ions that cannot move whereas the free electrons move and thereby generate a current which is measured by a current meter. The electronic signal that is measured is converted into a physical units using calibration and conversion factors.

The mathematics in this thesis are described in the three-dimensional Euclidean space with the three perpendicular unit vectors x, y, and z that define a right-hand Cartesian coordinate system. To express the direction of the incident irradiance, the spherical coordinates radius r, nadir angle Θ, and azimuth angle Φ are used. The connections between Cartesian and spherical coordinates

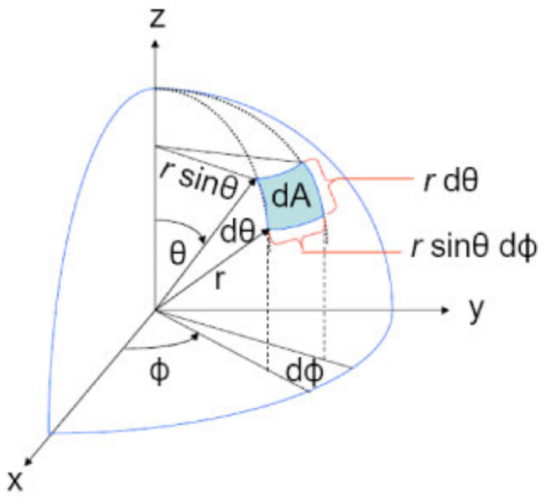

Figure 2.3: *Geometry used to obtain a differential element of area dA in spherical coordinates. Source: Mobley (1994).*

are $x = r \sin\Theta \cos\Phi$, $y = r \sin\Theta \sin\Phi$, and $z = r \cos\Theta$, with Θ and Φ ranging between $(0, \pi)$ and $(0, < 2\pi)$, respectively. It is practical to define the cosine parameter $\mu = \cos\Theta$ which ranges between -1 and 1.

Figure 2.3 defines the differential element of area $dA = (r \sin\Theta\, d\Phi)(r\, d\Theta)$ through which incident irradiance penetrates. Using dA, the differential element of solid angle $dA\, r^{-2}$ is defined, an expression needed to later describe the irradiance. It can be expressed in spherical coordinates as $d\Omega = \sin\Theta\, d\Theta\, d\Phi = d\mu\, d\Phi$.

This section describes how to quantitatively describe the light fields. This includes how radiant energy, its wavelength dependency, and its polarization can be measured as a function of direction at any location.

Figure 2.4 illustrates a schematic of a radiometer used to measure unpolarised spectral radiance (Advance-Radiance-Collector (ARC)). Photons which directions are indicated by $\hat{\xi}$ can enter the collecting tube of the radiometer with an incident angle of ψ or less. Light baffles steer the photons onto a translucent diffuser of area ΔA which makes the light field homogeneous. Only photons with the spectral resolution $\Delta\lambda$ around can pass through the filter. The unpolarised spectral radiance field $I(\vec{x}, t, \hat{\xi}, \lambda)$ describes how much radiation comes from which direction. It is detected as current or voltage output. After calibration the output is converted into the amount of radiant energy ΔQ entering the radiometer during a time interval Δt centered around t. The radiometer is considered to be small compared to the order of spatial (positional) changes in the light field is located for example under the ice at position $\vec{x}$.

The unpolarised spectral radiance provides the spatial, temporal, directional, and wavelength structure of the light field and is expressed as $I(\vec{x}, t, \hat{\xi}, \lambda) = \frac{\Delta Q}{\Delta t\, \Delta A\, \Delta\Omega\, \Delta\lambda}$ with units of $\mathrm{W\,m^{-2}\,sr^{-1}\,nm^{-1}}$. Thus, it is the power in a ray of light in a particular direction in such that

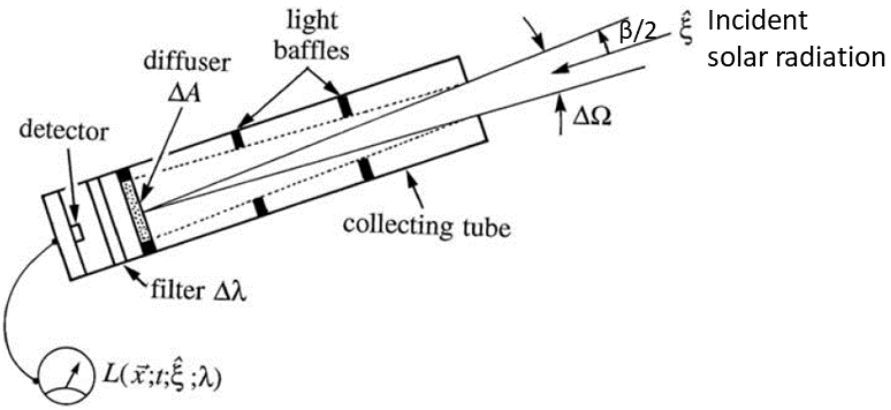

Figure 2.4: *Schematic representation of an Advanced-Radiance-Collector (ARC) radiometer to measure spectral radiance. Source: Mobley (1994).*

it is the radiant flux / nm per unit area per solid angle in a particular direction. In spherical coordinates it is abbreviated as $I(\Theta, \Phi, \lambda)$. In sea-ice optics, the radiance is measured to investigate the spatial variability of the light field and to identify which surface property such as ice thickness and snow depth drives the variability.

The spectral downwelling planar irradiance $E_d(\vec{x}, t, \lambda) = \frac{\Delta Q}{\Delta t\, \Delta A\, \Delta \lambda}$ with units $\mathrm{W\,m^{-2}\,nm^{-1}}$ is measured when the collecting tube of the ARC is removed (**Figure 2.4**). Such an Advanced-Cosine-Collector (ACC) radiometer (**Figure 2.5A**) detects photons from an entire hemisphere instead of from a single direction $\hat{\xi}$. The contribution of each photon arriving at the diffuser of area is weighted by $\cos\Theta$. Hence, the downwelling planar irradiance is the radiance scaled by $\cos\Theta$ and integrated over all downward directions (e.g., from the sun):

$$E_d(\lambda) = \int_{\Phi=0}^{2\pi} \int_{\Theta=0}^{\pi/2} I(\Theta, \Phi, \lambda)\, \cos\Theta\, \sin\Theta\, d\Theta\, d\Phi \tag{2.1}$$

The upwelling planar irradiance E_u is accordingly

$$E_u(\lambda) = \int_{\Phi=0}^{2\pi} \int_{\Theta=\pi/2}^{\pi} I(\Theta, \Phi, \lambda)\, \cos\Theta\, \sin\Theta\, d\Theta\, d\Phi \tag{2.2}$$

which is integrated over all upward directions (e.g., reflected from the surface). In case of isotropic conditions, meaning that the radiation is independent of direction, **Equations 2.1** and **2.2** simplify to $E_{d/u}(\lambda) = \pi\, I(\lambda)$.

The spectral downwelling scalar irradiance $E_{od}(\lambda)$ is measured using a radiometer with a spherical surface $\Delta A = \pi r^2$ where r is the radius of the diffuser (**Figure 2.5B**). The $\cos\Theta$ dependency drops and the downwelling and upwelling scalar irradiances can be expressed using the radiance as

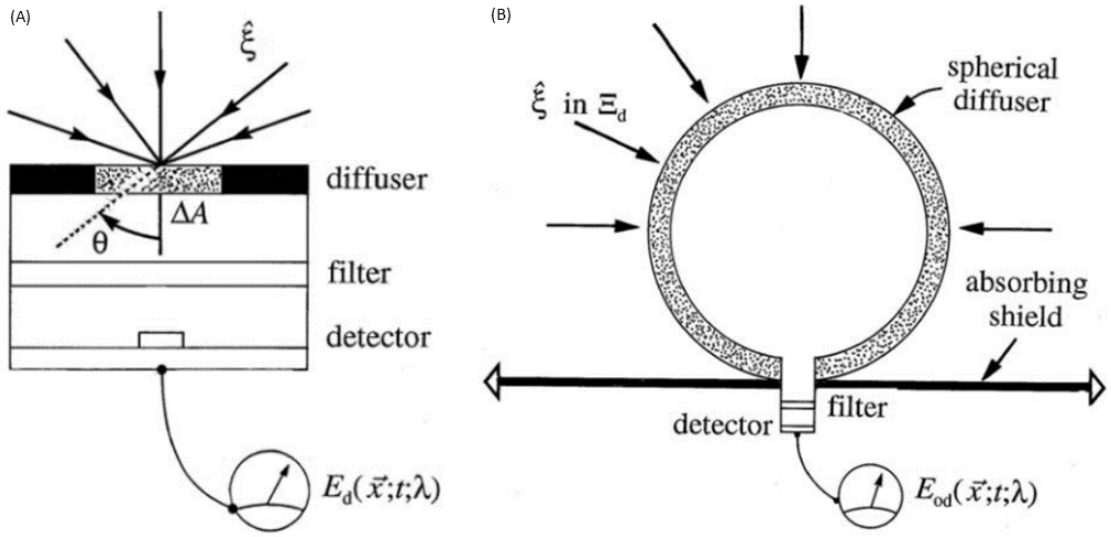

Figure 2.5: *Schematic representation of Advanced-Cosine-Collector (ACC) radiometers to measure spectral (**A**) planar and (**B**) scalar irradiance. Source: Mobley (1994).*

$$E_{od}(\lambda) = \int_{\Phi=0}^{2\pi} \int_{\Theta=0}^{\pi/2} I(\Theta, \Phi, \lambda)\, \sin\Theta\, d\Theta\, d\Phi \tag{2.3}$$

$$E_{ou}(\lambda) = \int_{\Phi=0}^{2\pi} \int_{\Theta=\pi/2}^{\pi} I(\Theta, \Phi, \lambda)\, \sin\Theta\, d\Theta\, d\Phi \tag{2.4}$$

Similarly, for isotropic conditions, **Equations 2.3** and **2.4** simplify to $E_{od/ou}(\lambda) = 2\pi I(\lambda)$.
If the absorbing shield that prevents upward-traveling photons from being detected is removed (**Figure 2.5B**), then the radiometer collects photons traveling in all directions. In this case, the spectral total scalar irradiance $E_o(\lambda)$ is measured with units of $\mathrm{W\,m^{-2}\,nm^{-1}}$ by integrating over all directions $\hat{\xi}$:

$$E_o(\lambda) = \int_{\hat{\xi}} I(\Theta, \Phi, \lambda)\, d\Omega(\xi) = E_{od}(\lambda) + E_{ou}(\lambda) \tag{2.5}$$

and for isotropic conditions, $E_o(\lambda) = 4\pi\, I(\lambda)$.
In sea-ice optics, the irradiance is measured to investigate the energy budget of the sea ice.

2.1.3 Apparent optical properties

Apparent optical properties (AOPs) are ratios and functions of the measured radiance and irradiance. Common AOPs in sea-ice optics are the albedo, transmittance, and bulk extinction coefficients. The AOPs can depend both on the medium and on the directional structure of the

light field. Thus, they are influenced by ice thickness, snow depth, and content of air-bubbles, brine, solids, impurities such as black carbon, and liquid water within the sea ice. As they are derived from field measurements of irradiance and radiance, they highly depend on the atmospheric conditions which can change rapidly (cloud cover, time of the day, incoming light field) and the ice geometry.

2.1.4 Inherent optical properties

In contrast to the AOPs, the inherent optical properties (IOPs) depend only on the structure of the medium. They are independent of the light field within the sea ice. The most common IOPs are the absorption and scattering coefficients as well as the scattering phase function and the refraction index of a medium. Thus, IOPs dominate variations in absorption and scattering (Light et al., 2008). IOPs are a necessary input for radiative transfer models and light parameterizations. The technology is evolving in such that prototype instruments are developed which can measure IOPs directly within sea ice (Perron et al., 2021).

2.1.5 Radiative transfer

The radiative transfer theory connects the IOPs with the AOPs. The equation of radiative transfer within a horizontally homogenous medium with vertical variations is described by Chandrasekhar (1960) as follows:

$$\mu \frac{dI(\tau, \mu, \Phi, \lambda)}{d\tau} = I(\tau, \mu, \Phi, \lambda) - S(\tau, \mu, \Phi, \lambda). \tag{2.6}$$

S is the source function which also includes scattering. τ is the optical depth defined as

$$\tau(\lambda) = [a(\lambda) + \sigma(\lambda)] \cdot z. \tag{2.7}$$

a is the absorption coefficient, σ the scattering coefficient, and z the depth to which the radiance penetrated into the medium. Considering a direct incident beam, the source function can be described as

$$\begin{aligned} S(\tau, \mu, \Phi, \lambda) = \frac{\bar{\omega_0}}{4\pi} \int_{-1}^{1} \int_{0}^{2\pi} p(\mu, \mu', \Phi, \Phi')\, I(\tau, \mu, \Phi, \lambda)\, d\mu'\, d\Phi \\ - \frac{E_0(\lambda)}{4}\, p(\mu, \mu', \Phi, \Phi')\, exp(-\tau(\lambda) \,/\, \mu_0). \end{aligned} \tag{2.8}$$

$\bar{\omega_0}$ is the single scattering albedo which gives the attenuation in radiation due to scattering

(Chandrasekhar, 1960; Mobley, 1994) and is expressed as

$$\bar{\omega_0} = \frac{\sigma(\lambda)}{k(\lambda) + \sigma(\lambda)}. \tag{2.9}$$

$\bar{\omega_0}$ ranges between 0 (fully absorbing) and 1 (fully scattering). $p(\mu, \mu', \Phi, \Phi')$ is the scattering phase function and E_0 is the radiance of the direct beam component of the incident radiation. The double integral in the first term on the right hand side is used for diffuse radiative processes and represents scattering of the radiance $I(\tau, \mu', \Phi', \lambda)$ from different directions into the direction (μ, Θ). The phase function determines the amount of radiation that is scattered from one direction to another. The second term on the right hand side contains the contribution of scattered radiation from $E_0(\lambda)$ and is only applicable in case of both direct and diffuse radiation.

2.1.6 Absorption

Spectral variations in the sea-ice optical properties are due to absorption (Perovich, 1996). When sea ice grows, particulates, sediments, algae, air bubbles, and brine can be trapped into its structure (Perovich, 2017; Petrich and Eicken, 2017). Algae are mostly trapped in the bottom of the sea ice (Arrigo, 2014). They can also be attached to the ice bottom whereas phytoplankton is present in the upper water column. Soot, sediments, and other particulates can be deposited on the sea-ice surface (Light et al., 2008).

Those different components and inclusions exhibit contrasting physical and optical properties. They strongly determine the partitioning of solar radiation and, thus, impact the energy balance of the sea ice.

The magnitude of the radiation that penetrates into the sea ice decays exponentially with the penetration depth z into the ice or inclusions and with the absorption coefficient. It is common practice to solve **Equation 2.8** for the case without additional light sources across boundaries and without scattering ($S = 0$, $\sigma = 0$ in **Equations 2.6** and **2.7**). When considering a direct beam of radiation normally incident on the inclusions ($\Theta = 0$ meaning $\mu = 1$ in **Equation 2.6**), the decay is described by the Bouguer-Lambert and Beer's law:

$$I(z, \lambda) = I(z = 0, \lambda)\, exp(-az). \tag{2.10}$$

where $I(z = 0, \lambda)$ is the radiance incident on the surface of the medium before penetration.

Absorption coefficients are very different for the variety of inclusions in sea ice. Absorption in air bubbles is neglected and thus, coefficients are assumed to be zero. The absorption coefficients for pure ice and brine greatly depend on the wavelength (**Figure 2.6A**, Perovich

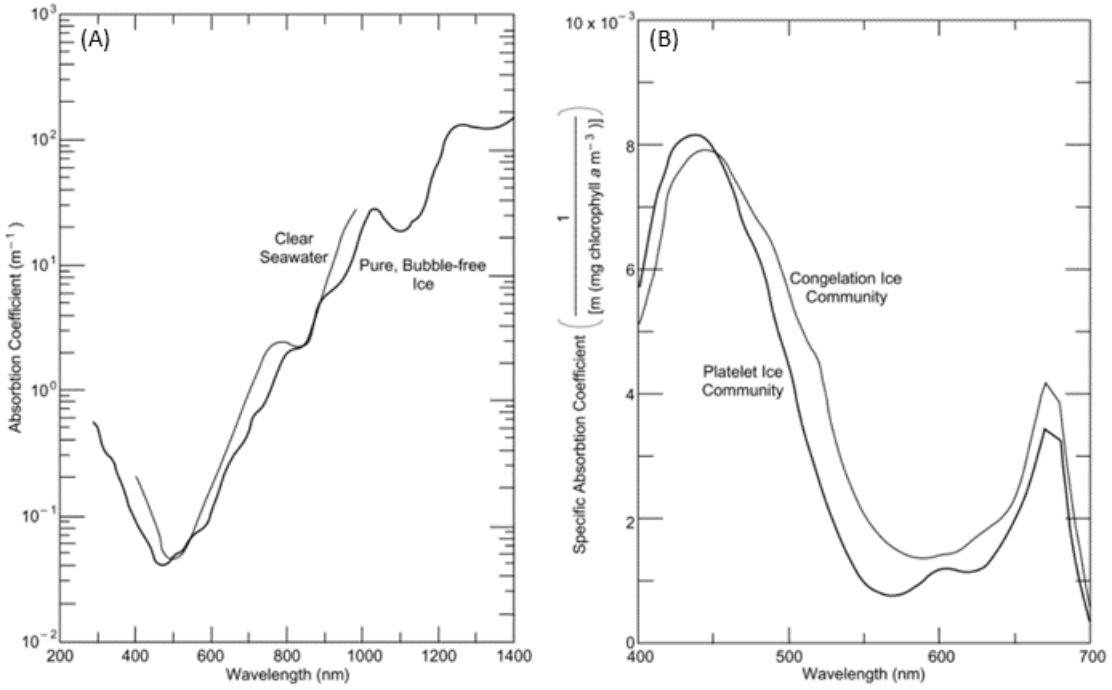

Figure 2.6: *Absorption coefficients of (**A**) clear seawater (Tyler and Smith, 1970; Smith and Baker, 1981), pure bubble-free ice (Grenfell and Perovich, 1981; Perovich and Govoni, 1991) and (**B**) biomass found in congelation ice and frazil ice (Arrigo et al., 1991). Source: Perovich (1996).*

(1996). Values for pure ice are less than $0.05\,\mathrm{m}^{-1}$ at blue wavelengths, increasing to more than $10\,\mathrm{m}^{-1}$ in the near-IR (Light et al., 2004). This means that pure ice is mostly transparent for radiation of blue wavelengths. Absorption coefficients for clear seawater are similar in magnitude and spectral shape to those of pure ice. Absorption coefficients for pure water range from around $0.01\,\mathrm{m}^{-1}$ at 380 nm to $1.68\,\mathrm{m}^{-1}$ at 728 nm with a minimum of $0.004\,\mathrm{m}^{-1}$ at 418 nm (Pope and Fry, 1997). The absorption coefficients of brine are assumed to closely follow those of pure water for visible and near-IR wavelengths (Tyler and Smith, 1970; Grenfell, 1983). The absorption coefficients for sea ice are a combination of those of brine and pure ice taken into account their respective volume fraction (Grenfell, 1983).

Particulate matter such as phytoplankton and algae absorb radiation very efficiently at 440 nm and 670-680 nm (**Figure 2.6B**, e.g., Arrigo et al. (1991); Mundy et al. (2007); Wongpan et al. (2018). Little radiation is absorbed between 575 nm and 650 nm. The absorption coefficients are usually presented in units of $\mathrm{m}^2\,\mathrm{mg\,chl}\,a^{-1}$. They can range from $0.02\,\mathrm{m}^2\,\mathrm{mg\,chl}\,a^{-1}$ at 400 nm, increasing to primary peak values of $0.026\,\mathrm{m}^2\,\mathrm{mg\,chl}\,a^{-1}$ at 440 nm before they decrease towards $0.006\,\mathrm{m}^2\,\mathrm{mg\,chl}\,a^{-1}$ at 600 nm to increase again towards their secondary peak of $0.018\,\mathrm{m}^2\,\mathrm{mg\,chl}\,a^{-1}$ at 670 nm and finally decrease to their minimum of $0\,\mathrm{m}^2\,\mathrm{mg\,chl}\,a^{-1}$ at 700 nm (Mundy et al., 2007).

2.1.7 Scattering

The inclusions within sea ice, such as brine, air bubbles, or solid salts, have different refractive indices n than the surrounding pure ice. Radiation that penetrates the interface between pure ice and an inclusion is scattered and thus, attenuated. The larger the difference in refractive indices, the larger the scattering (Perovich, 1996). The refractive index for pure ice is ~ 1.30, for air ~ 1.0, for solid salts ~ 1.5, and for brine it ranges between 1.34 and 1.40 because of its temperature-dependency (Maykut and Light, 1995). Solid salts scatter very effectively and form when the ice is cold enough (Perovich and Grenfell, 1981).
Scattering is described by the scattering coefficient σ and the phase function. The scattering coefficient gives information about the amount of scattering per unit length. It depends not only on the amount of inclusions, but also on their volume, size, and distribution within the ice (Perovich, 1996). The phase function describes the angular dependency of scattering. In this dissertation and in most sea-ice related radiative transfer problems, the Henyey-Greenstein phase function (Henyey and Greenstein, 1941) is used which is only a one-parameter analytical approximation to a real phase function (Edström, 2005). The asymmetry parameter g of the Henyey-Greenstein phase function describes in which direction radiation is scattered. It ranges from 0 for isotropic scattering (scattering is equal in all directions) over 1 for complete forward scattering to -1 for complete backward scattering. Scattering in sea ice is large, varies greatly depending on the inclusions, is strongly forward peaked, and is assumed to be wavelength-independent (Grenfell, 1983, 1991; Perovich, 1993, 1996).
The scattering coefficients range from $1.2\,\mathrm{m}^{-1}$ for melting blue ice over $160\,\mathrm{m}^{-1}$ for ice at its melting point and with a mixture of inclusions (Perovich, 1990) to $>200\,\mathrm{m}^{-1}$ for ice with many air bubbles or ice with solidified salts (Perovich and Grenfell, 1982). On the surface of melting sea ice, a SSL forms which highly scatters, is observable as a bright white layer, and consists of a crumbly texture (Light et al., 2008). Light et al. (2008) derived scattering coefficients ranging from $500\,\mathrm{m}^{-1}$ to $1100\,\mathrm{m}^{-1}$ for the surface layer of bare, melting ice and $8\,\mathrm{m}^{-1}$ to $30\,\mathrm{m}^{-1}$ for the ice interior and ponded ice. A snow cover overlying the sea ice scatters significantly with coefficients ranging from $160\,\mathrm{m}^{-1}$ for melting wet snow to $800\,\mathrm{m}^{-1}$ for cold dry snow (Perovich, 1990). The Scattering coefficient of ice-algae is assumed zero (Mundy et al., 2007).

2.1.8 Extinction

The combined loss of radiation within sea ice due to absorption and scattering is described by extinction. While absorption determines the wavelength dependence of extinction, scattering dominates its magnitude. The decrease in the magnitude and the change in the spectral shape of radiation are described by the spectral extinction coefficients k (**Figure 2.7**). Extinction coefficients can be determined by measurements of incident, reflected, and transmitted radiation

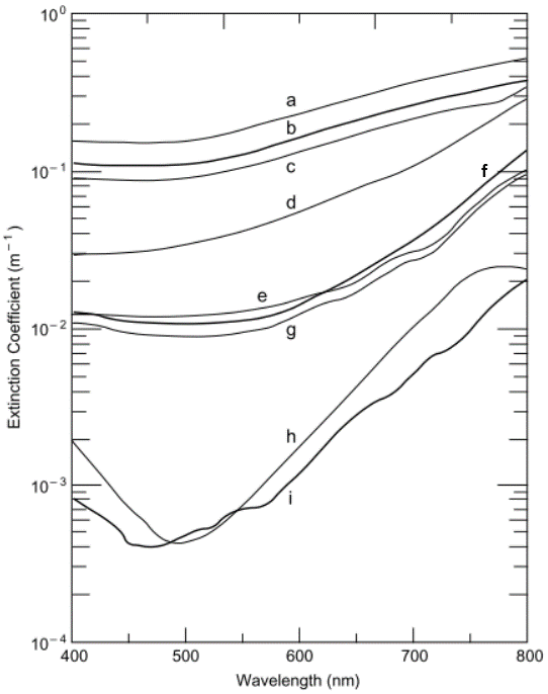

Figure 2.7: *Spectral extinction coefficients for (**a**) cold, dry snow (Grenfell and Maykut, 1977), (**b**) MYI below the eutectic point with solid salts present (Perovich and Grenfell, 1981), (**c**) melting snow (Grenfell and Maykut, 1977), (**d**) SSL of white MYI (Grenfell and Maykut, 1977), (**e**) interior of white MYI (Grenfell and Maykut, 1977), (**f**) cold, blue MYI (Grenfell and Maykut, 1977), (**g**) melting, blue MYI (Grenfell and Maykut, 1977), (**h**) bubble-free, fresh ice (Grenfell and Perovich, 1981), and (**i**) clear Arctic water (Smith and Baker, 1981). Source: Perovich (1996).*

or computed using RT models (Grenfell and Maykut, 1977; Perovich and Grenfell, 1981).

Broadband extinction coefficients for sea ice range from $0.6\,\mathrm{m}^{-1}$ to $5.0\,\mathrm{m}^{-1}$ depending on the surface conditions and ice types (Grenfell and Maykut, 1977; Light et al., 2008; Katlein et al., 2019). Snow attenuates radiation approximately 10 and 100 times more efficient than ice and water, respectively, with values ranging from $4.3\,\mathrm{m}^{-1}$ for dense snow (Weller and Schwerdtfeger, 1967) to $40\,\mathrm{m}^{-1}$ for freshly fallen snow (Thomas, 1963).

Spectral extinction coefficients for different snow and sea-ice types as well as for water are illustrated in **Figure 2.7**. Variations are quite large highlighting their strong impact on the partitioning of the solar radiation, especially on the under-ice radiation. Except for bubble-free, fresh ice (**h**) and clear Arctic water (**i**), extinction coefficients are relatively constant between 400 nm and 500 nm. For longer wavelengths, the coefficients of all types strongly increase, implying that radiation in the near-IR is strongly attenuated.

Spectral snow extinction coefficients are up to 20 times larger than those of melting, blue ice (**a** and **g**). For melting snow, the coefficients decrease by about 50% (**c**). Solid salts scatter very efficiently due to their high refractive index, and thus, extinction coefficients are also high (**b**). Similarly, due to the plenty and effectively scattering air bubbles in the SSL of white MYI,

extinction coefficients are also high (**d**). While the amount of air bubbles is less in the interior of white MYI (**e**) and cold, blue MYI contains rather brine pockets than air bubbles (**f**, **g**), their extinction coefficients are lower.

2.1.9 Albedo

The albedo is the fraction of the incident solar radiation that is reflected by the sea-ice surface. It strongly depends on the snow and surface conditions and is wavelength-dependent.
Broadband albedos range from 0.05-0.07 for open water, over 0.2-0.4 for melt-ponds, 0.5-0.7 for bare ice, 0.60-0.65 for melting white ice, 0.75 for white bare ice, to 0.75-0.85 for snow-covered sea ice (e.g., Langleben, 1968; Grenfell and Maykut, 1977; Warren, 1982; Grenfell and Perovich, 1984; Perovich, 1996; Perovich et al., 2002a).
The dependency of the albedo on the ice thickness is strongest for new, thin growing ice (Weller, 1972). While the albedo increases more gradually with the thickening of the ice, it remains more or less constant for ice thicker than 0.8 m (Maykut, 1982).
Spectral albedos increase with ice thickness at all wavelengths. When the ice grows to a certain thickness, the wavelength dependency can be neglected. This is because only a small amount of radiation reaches the bottom of the ice from which radiation is backscattered towards the surface while being absorbed (Perovich, 1996). In this case, the ice is optically thick.
Due to its dependency on the surface conditions, the albedo strongly varies seasonally (**Figure 2.8**). Seasonal changes in albedo are most pronounced from spring to summer, when the surface evolves from snow-covered over bare ice to melting ice and finally open melt ponds.
Snow albedo is highest because of its high reflective properties owing the large air content and the low density of snow (**a**, Sturm and Massom (2017). For visible wavelengths the albedo is nearly constant resulting in the bright and white appearance of snow. The reason for the weak wavelength-dependency and thus, a weak influence of absorption, is the very high scattering coefficients of snow.
The albedo for cold, bare MYI (**b**) is lower. Due to its age, the MYI consists of a SSL with a high air bubble content. Thus, scattering is still high but less than for snow. Hence, the influence of absorption increases and thus, the wavelength-dependency.
As the ice warms and starts to melt, albedos decrease further (**c**). While melting, water fills the air voids and thus, scattering decreases and absorption and the wavelength-dependency increase.
The albedo continues to decrease with the progression in melting and the subsequent formation of melt ponds (**d** and **e**). Due to the transparency of water for short wavelengths and a low scattering coefficient of water, the melt ponds appear blue. Spectral albedos are highest at 400-500 nm and mainly determined by scattering of the underlying ice at those wavelengths. The

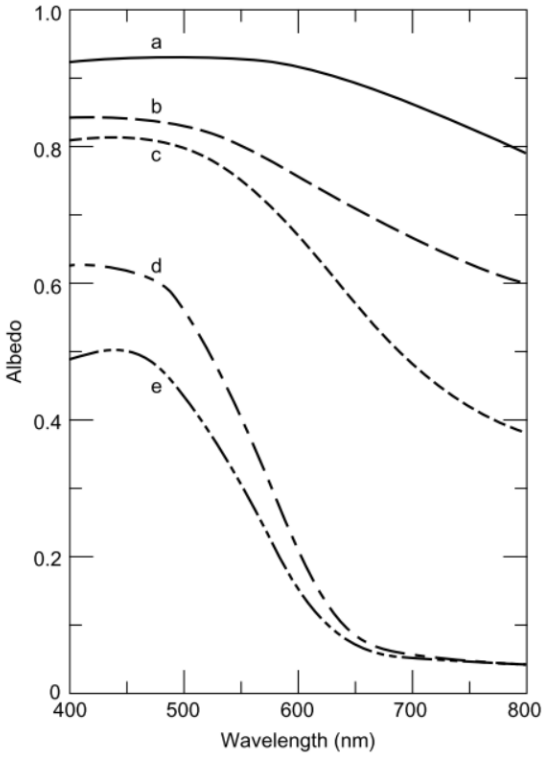

Figure 2.8: *Spectral albedos for (**a**) snow-covered MYI, (**b**) cold bare MYI, (**c**) melting bare MYI, (**d**) MYI covered with early-season melt pond and (**e**) mature melt pond (Grenfell and Maykut, 1977). Source: Perovich (1996).*

rapid decrease in albedo from 500 nm to 800 nm is due to the absorption of water dominating over the scattering of the ice.

2.1.10 Transmittance and transflectance

The transmittance $t_m(\lambda)$ is the fraction of the on the sea-ice surface incident solar irradiance that is transmitted through the sea ice into the underlying ocean. Thus, it is the radiation that is neither reflected or scattered at the surface nor absorbed or scattered within the sea ice. In the same way, the transflectance $t_f(\lambda)$ is the fraction of the incident radiance that is transmitted. The magnitude and spectral shape of the transmittance strongly depend on the ice thickness (e.g., Katlein et al., 2015), the surface conditions such as a snow cover (e.g., Mundy et al., 2007), a SSL (e.g., Light et al., 2008) or melt ponds (e.g., Nicolaus et al., 2012), and on inclusions within the ice (e.g., Perovich, 1996). The magnitude is dominated by scattering and the spectral by absorption within the ice both expressed by the spectral extinction coefficients. For example, the transmittance of a two-layer system consisting of snow and sea ice decays exponentially with snow depth d_s and ice thickness d_i described by the spectral snow and sea ice extinction coefficients $k_s(\lambda)$ and $k_i(\lambda)$ of the form

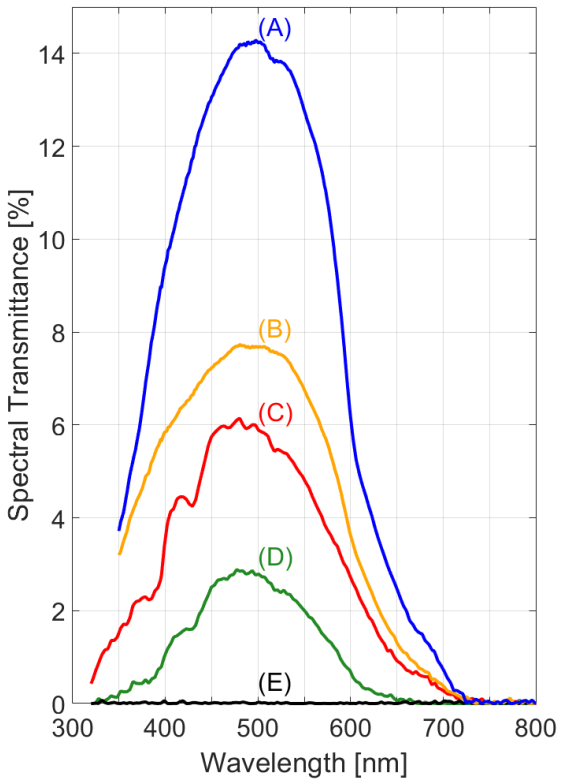

Figure 2.9: *The influence of ice thickness and surface conditions on spectral transmittance. (**A**) Melt pond with 0.3 m depth on 1.60 m thick MYI, (**B**) snow-free 1.86 m thick bare ice, (**C**) 1.56 m thick FYI with a 0.20 m thick snow cover, (**D**) 1.48 m thick FYI with a 0.41 m thick snow cover, and (**E**) 1.66 m thick FYI with a 0.59 m thick snow cover. The transmittance was obtained during the three expeditions presented in this dissertation: (**A**) and (**B**) in the central Arctic in summer 2018 and (**C**), (**D**), and (**E**) in the Lincoln Sea in late spring 2018.*

$$t_m(\lambda, d_i, d_s) = i_0 \exp\left(-k_i(\lambda)\, d_i - k_s(\lambda)\, d_s\right). \tag{2.11}$$

i_0 is the fraction of the broadband incident irradiance transmitted through the top 0.1 m of the ice (Perovich, 1996). i_0 ranges between 0.18 and 0.63 depending on ice type and atmospheric conditions (Grenfell and Maykut, 1977).

The transmittance in the visible of a melt pond on summer sea-ice is high because melt ponds are translucent and lack a persistent SSL (e.g., Grenfell and Maykut, 1977; Light et al., 2008; Nicolaus et al., 2012, **Figure 2.9A**). During summer, the transmittance of snow-free ice is also high because of a lacking snow cover but significantly lower than that of melt ponds (**B**). A thin (0.20 m) layer of cold snow can reduce the transmittance further (**C**) and a thick (0.41 m) layer of snow to less than 3% (**D**). Sea ice covered by a snow layer as thick as 0.59 m transmits almost no light (**E**).

During summer, sea-ice thickness determines most of the spatial variability in the transmittance

on large scales, while on smaller scales ($< 1000\,m^2$), melt ponds control the variability (Katlein et al., 2015). During winter and spring, it is the snow cover that limits the transmittance and dictates its variability (e.g., Mundy et al., 2005).

2.2 Mass balance

This section describes the sea-ice extent and thickness distribution in the Arctic, thermodynamic and dynamic growth of sea ice, surface and bottom melting, and snow on sea ice. It closely follows the work from Warren et al. (1999), Haas (2017), Petrich and Eicken (2017), Sturm and Massom (2017), Webster et al. (2018), and Meredith et al. (2019).

2.2.1 Sea-ice extent and concentration

The Arctic sea-ice extent is defined as the area of ocean with an ice concentration of at least 15% (Walsh, 2005). It is an estimate of the actual sea-ice area. The sea-ice extent experiences huge seasonal and interannual variability. Since the era of satellite observation started in 1978 (e.g., Meier et al., 2014), both the sea-ice extent and concentration are extensively and reliably monitored (e.g., Spreen et al., 2008). The annual maximum in sea-ice extent is with approximately 15 million km^2 in March while the minimum of 4-5 million km^2 is in September (Walsh, 2005). The mean sea-ice extent in March 2021 and September 2021 are shown in **Figure 2.10**.

In general, the area of the Arctic sea ice is divided into the permanent and the seasonal ice zone. The permanent ice zone is outlined by the minimum ice extent in September (**Figure 2.10**, right) while the seasonal ice zone is the area between the permanent zone and the sea-ice extent maximum in March (**Figure 2.10**, left). The seasonal variability in sea-ice extent arises from sea-ice melt during summer and refreezing and growth in winter. The interannual variability is described by the variations of the ice edge which can vary as much as five degrees in latitude depending on region and time (Walsh, 2005). In general, the permanent ice zone consists mainly of MYI and the seasonal ice zone of FYI that did not survive the melt season.

2.2.2 Sea-ice thickness

The sea-ice thickness ranges between few centimetres for newly formed ice and up to several metres for highly deformed ice and pressure ridges (**Figure 2.11**, Haas, 2017). Historical records of Arctic-wide ice thickness data are available from upward-looking sonars mounted on submarines (Kwok and Rothrock, 2009). Nowadays, the ice thickness is also measured using satellites (e.g., Hendricks et al., 2018), moored sonars (Krishfield et al., 2014; Belter et al., 2021) and electromagnetic induction sounding devices dragged along the sea-ice surface (e.g.,

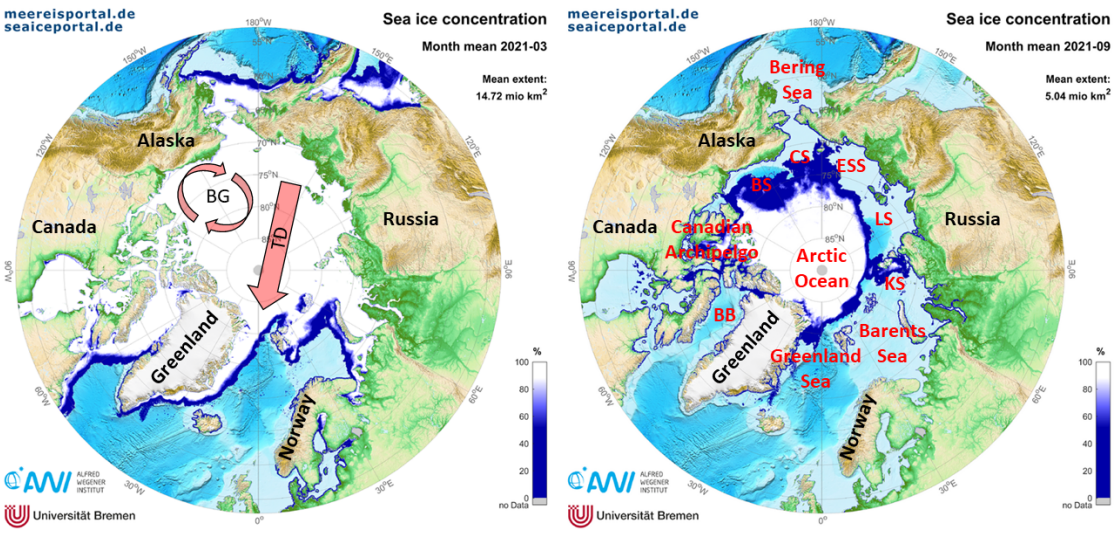

Figure 2.10: *Sea-ice concentration in % as shown by the colour bar in the Arctic in March 2021 (left) and September 2021 (right). The figures were obtained from the AWI Meereisportal (Spreen et al., 2008; Grosfeld et al., 2016) and modified with annotations. The red arrows (left) indicate the Beaufort Gyre (BG) and the Transpolar Drift (TD). In the right figure are marked in red the seas surrounding the Arctic Ocean with the abbreviated ones being the Beaufort Sea (BS), Chukchi Sea (CS), East Siberian Sea (ESS), Laptev Sea (LS), Kara Sea (KS), Baffin Bay (BB).*

Hunkeler, 2016; Haas et al., 2017) or towed in the air by aircraft (e.g., Haas et al., 2010; Haas et al., 2021 (AIRPLANE); Haas et al., 2006; Haas et al., 2008 (HELI)).

A large spatial gradient in sea-ice thickness exists with thin ice and thicker FYI along the Russian and Alaskan coasts and with very thick MYI and ridges along the Canadian and Greenlandic coasts (**Figure 2.10**, e.g., Kwok et al., 2009; Jahn et al., 2012). The frequency histogram of ice thickness data shown in **Figure 2.11** illustrates the variety of ice types with different ice thicknesses. The following scenario describes the dominate thickness evolution process observed in the Arctic guided using **Figures 2.11** and **2.12**: Thin and new ice forms quickly through thermodynamic processes favoured by very low air temperatures in areas of open water such as polynyas, especially in the shelf seas along the Russian coast, small leads, and cracks.

New and thin ice is usually <0.5 m thick. Subsequent thickening of thin ice results in lead ice (defined only for the purpose of this dissertation) with a thickness of <1.0 m. The thickness distribution continues over thicker FYI with thickness of <2.0 m previously formed in and exported from open water areas. The ice is pushed away from the lee sides of the coasts (divergence, **Figure 2.12**) towards the North Pole in response to the mean pattern of sea-ice drift mainly due to wind and ocean current forcing (Transpolar Drift, **Figure 2.10**). Open water areas are replenished where new ice can form. The sea ice continues to grow to SYI with thicknesses between 2.0 m and 3.5 m whereas melt-pond covered SYI and MYI is thinner (**Figure 2.11**). Due to the drift, sea ice is converged against the Canadian Arctic Archipelago, resulting in the

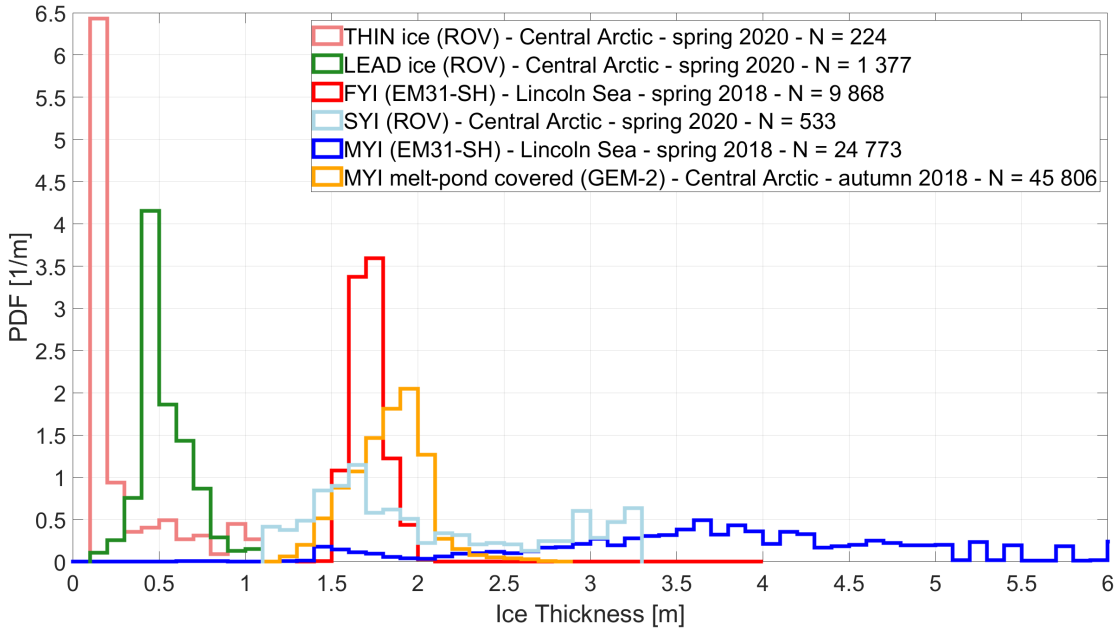

Figure 2.11: *Ice thickness distribution (probability density function (PDF), 0.1 m bin width) from different locations and seasons in the Arctic obtained by a sonar altimeter attached to an ROV (**Section 2.3** and **Figure 2.13A**) and electromagnetic induction sounding devices (**Section 2.3**, EM31-SH and GEM-2 (**Figure 2.13E**)). Note: The altimeter is used to measure the sea-ice draft. The draft was multiplied by a factor of 1.1 to convert the draft to ice thickness. N is the number of measurements.*

evolution of thick and old MYI (> 2 m to 4 m) as well as very thick pressure ridges (> 6 m) as the drifting ice cover collides with the shore-anchored landfast ice (**Figure 2.12**).

2.2.3 Thermodynamic growth

New ice grows in areas of open water in response to atmospheric forcing, such as sub-zero air temperature (**Figure 2.12**). The seawater cools down to its freezing point of approximately -1.9 °C (T_f). Subsequently, when more latent heat is released to the atmosphere, sea ice starts to form.

The thermal balance of a sea-ice cover with its surroundings is described as

$$(1-\alpha)\cdot F_R + I_0 + F_L\downarrow + F_L\uparrow + F_{OHF} + F_{Latent} - F_C + F_M = 0. \tag{2.12}$$

α is the albedo, F_R is the incident solar shortwave flux, I_0 the penetrated shortwave radiation, $F_L\downarrow$ the incident longwave flux, $F_L\uparrow$ the outgoing longwave flux, F_{OHF} the turbulent sensitive/ocean heat flux, F_{Latent} the turbulent latent heat flux which includes evaporation, F_M the heat flux due to freezing or melting, and F_C the conductive heat flux through the ice. Fluxes

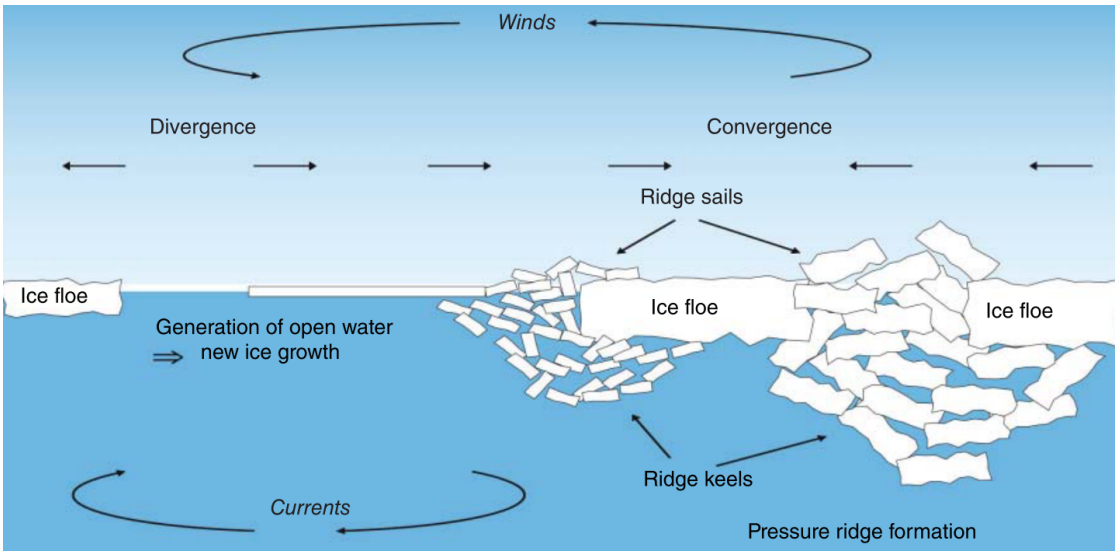

Figure 2.12: *Illustration of thermodynamic and dynamic processes contributing to the development of the sea-ice thickness distribution. Source: Haas and Druckenmiller (2009).*

directed into the ice are considered positive.

F_C describes how much energy is transferred into a unit area per unit time of the surface ice layer. The rate depends on the thermal conductivity of ice which in turn is a function of temperature T and salinity S of the form $\kappa_i = \kappa_i(S,T)$ (e.g., $2.0\,\mathrm{W\,m^{-1}\,K^{-1}}$) and the vertical temperature gradient $\partial T/\partial z$:

$$F_C = \kappa_i \left(\frac{\partial T}{\partial z}\right)_z = -\kappa_i \frac{T_f - T_0}{d_i}, \tag{2.13}$$

with ∂T being the difference between the salinity-dependent freezing temperature T_f at the bottom and the surface temperature T_0, and d_i the ice thickness.

The heat flux F_M due to freezing or melting can be written as

$$F_M = \rho_i L_i \left(\frac{dd_i}{dt}\right)_0, \tag{2.14}$$

Where ρ_i is the density of ice (e.g., $917\,\mathrm{kg\,m^{-3}}$), L the latent heat of fusion of ice (here $333.5\,\mathrm{kJ\,kg^{-1}}$), and $\frac{dd_i}{dt}$ the temporal change in ice thickness.

The turbulent sensitive/ocean heat flux F_{OHF} (measured by the temperature difference between surface and atmosphere) causes either melting or is conducted through the ice. By virtue of simplification, it is supposed that there is no thermal inertia in the ice and no internal heat sources. As a result, **Equation 2.12** reduces to

$$\rho_i L_i \left(\frac{dd_i}{dt}\right)_0 = \kappa_i \frac{T_f - T_0}{d_i} - F_{OHF}, \tag{2.15}$$

which is the ice growth rate. When there is no convection in the water column beneath the sea ice, $F_{OHF} = 0$.

Assuming a known surface temperature, $T_0 = T_{i,surface} = T_{air}$, integrating **Equation 2.4** in time, and introducing the number of freezing-degree days (FDD) $\Gamma = \int_0^t (T_f - T_{air})\, dt$ with time steps $dt = 1$ day gives the analytical solution for the ice thickness d_i,

$$d_i^2 = d_{i0}^2 + b^2\, \Gamma, \tag{2.16}$$

with d_{i0} being the initial ice thickness and $b = \sqrt{\frac{2\kappa_i}{\rho_i L_i}}$.

Snow overlying an ice cover causes an insulating effect because it is less compressed and contains a greater air volume than ice which results in a lower heat conductivity $\kappa_s \ll \kappa_i$. The ice growth rate is therefore reduced when a snow cover is present (Leppäranta, 1993). To include this effect, the heat conduction through a snow layer with depth d_s is added in **Equation 2.15**:

$$\rho_i L_i \left(\frac{dd_i}{dt}\right)_0 = \kappa_s \kappa_i \frac{T_f - T_{air}}{\kappa_s d_i + \kappa_i d_s} - F_{OHF}, \tag{2.17}$$

where κ_s ranges between $0.15\,\mathrm{W\,m^{-1}K^{-1}}$ and $0.40\,\mathrm{W\,m^{-1}K^{-1}}$. If more heat is conducted away towards the atmosphere then is mixed up from the ocean, sea ice forms. When air temperature remains low or become lower, sea ice further grows downwards.

2.2.4 Dynamic growth

Due to wind and ocean flow patterns, sea ice diverges and converges and different ice floes crash into each other thereby forming pressure ridges (**Figure 2.12**). Rafting and ridging account for the thickest ice and rapid thickening. However, those dynamic processes also create areas of open water in which frazil ice and subsequently pancake ice form. Wind and ocean swell shape the pancake ice and by time this ice type can contribute a large fraction of the sea-ice cover (Petrich and Eicken, 2017).

2.2.5 Melting

The seasonal variability in sea-ice thickness is driven by surface and bottom melt in summer (e.g., Perovich et al., 2011b) and by the formation of new ice in polynyas and leads and by bottom growth in winter and spring. Surface melting is driven by solar radiation incident on the

sea-ice surface. Bottom melting is initiated when the ocean heat flux exceeds the convective heat flux towards the atmosphere or due to warming of seawater adjacent to sea ice and advection of warm water.

In most years, surface melt exceeds bottom melt. However, for example, Perovich et al. (2008) observed an increase in open water area which led to a 500% anomaly in solar heat input in the Beaufort Sea. This resulted in increased bottom melting which might have been responsible for the extreme retreat of the sea-ice cover in 2007 (Perovich et al., 2008; Lindsay et al., 2009). As the sea-ice extent decreases, the fraction of open water area increases. This leads in particular at lower latitudes to enhanced solar heat input into the ocean and increases bottom melting in sea-ice covered regions (Perovich et al., 2008). Such events drive the interannual variability in surface and bottom melt.

Events of remarkable bottom melting might increase due to climate change as was observed in the Beaufort Sea and at the North pole during several summers (Perovich et al., 2008). By the same token, the increase in the length of the melt season and the decrease in the length of the freezing season increases surface melt (Markus et al., 2009; Vaughan et al., 2013).

2.2.6 Snow

Snow on sea ice plays a key role for the thermodynamic ice growth and in the partitioning of solar radiation (e.g. Mundy et al., 2007; Sturm and Massom, 2017), and thus, for the ice- and ocean-associated ecosystem (Mundy et al., 2005) due to its high reflectivity (Grenfell and Maykut, 1977) and insulation (e.g., Sturm et al., 1997). The snow distribution and properties are highly affected by dynamic atmospheric and sea-ice conditions. Therefore, snow is very heterogeneous and its properties vary both seasonally and annually as well as spatially across the sea-ice covered Arctic Ocean.

Due to the high air content of snow, its density is low ranging from $133\,\mathrm{kg\,m^{-3}}$ to $488\,\mathrm{kg\,m^{-3}}$ depending on the snow type (Sturm et al., 1998). For the same reason the snow's thermal conductivity is also low ranging from $0.07\,\mathrm{W\,m^{-1}K^{-1}}$ to $0.45\,\mathrm{W\,m^{-1}K^{-1}}$ (Sturm et al., 1998). The albedo of snow ranges from 0.77 for melting snow over 0.81 for wind-packed snow to 0.89 for new snow (Perovich, 1996).

Snow depth is measured using a variety of instruments and methods including passive microwave satellites, visual observations from ships, *in-situ* measurements, and autonomous measuring systems. However, to this date little is known about the spatial and temporal distribution of snow depth on sea ice on the regional to global scales.

Most snow fall occurs in autumn and depending on the recent weather. Minor snow fall occurs in spring and winter. During the summer, the sea ice is usually snow-free due to surface melting. The snow cover reaches a maximum snow depth in May, where snow-ice interactions

are most dynamic and exert the greatest degree of control on the ice (Sturm and Massom, 2017). The snow melt starting in spring sets the timing for ice melt and pre-conditions the ice (Sturm and Massom, 2017). This makes information about the snow depth both in space and time tremendously important.

Snow re-distribution, transport, and erosion are dominated by wind conditions and surface roughness as well as the fraction of open water, such as leads where might be lost into due to wind. Thus, reliable estimates of mean snow depth are not possible. Nevertheless, mean snow depth estimates for Arctic sea-ice exist. They range from 0.21 m in the Beaufort Sea (Sturm et al., 2006) over 0.23 m in the Canadian Archipelago (Iacozza and Barber, 2001) to 0.34 m in the Central Arctic (Warren et al., 1999). A pattern in regional snow depth distribution is observed that indicates that the deepest snow is found north of Greenland and in the eastern Canadian Archipelago whereas snow depth decreases towards Siberia (Serreze and Maslanik, 1997; Warren et al., 1999).

2.3 Instruments

Several different scientific platforms and instruments were used in this dissertation to perform the measurements **Figure 2.13**. They are here briefly summarized and more details are provided at appropriate places throughout this thesis.

Remotely operated vehicle (ROV, M500, Ocean Modules, Åtvidaberg, Sweden, Katlein et al., 2017 **Figure 2.13A**): The ROV used here is equipped with a sensor platform for interdisciplinary sea-ice research at the ice-ocean interface. The system is made to function reliably in harsh polar conditions and can be operated by at least two scientists that need to simultaneously operate a wide variety of sensors and monitor their real-time data streams. The vehicle attitude (pitch, roll, heading) is measured with an inertial measurement unit. The sensors that were used for this dissertation are RAMSES-ACC and -ARC hyper-spectral radiometers (320-950 nm, TriOS Mess- und Datentechnik GmbH, Rastede, Germany) to measure transmitted irradiance and radiance, respectively. The spectral resolution of the radiometers is 3.3 nm which is usually interpolated to 1 nm (Nicolaus et al., 2010a). Further used are a sonar altimeter (PA-500 High Precision Altimeter, Tritech, UK) with a measurement range between 0.1 m and 10 m and a frequency of 500 kHz to measure the distance from the ROV to the ice bottom, a CTD (conductivity, temperature, depth, pumped SBE GPCTD, Seabird Scientific, USA) to measure the depth additionally to a pressure sensor (Keller A-21Y, Keller AG, Jestetten, Germany), and a high definition zoom camera (Surveyor WAHD, Bowtech). An acoustic-based long-baseline (LBL, Pinpoint Linkquest, San Diego, CA, USA) positioning system was used to retrieve the geographic or local-floe position of the ROV under the ice. The full list of the scientific sensor suite, technical details, and information about the operation scheme of the ROV system can

Figure 2.13: *Instruments and measuring systems used in this dissertation: (**A**) Remotely operated vehicle (ROV) Beast (Katlein et al., 2017), (**B**) Terrestrial laser scanner (photo: Steve Duerksen, Fisheries and Ocean Canada), (**C**) Magnaprobe (photo: Pierre Coupel, Fisheries and Ocean Canada), (**D**) Radiation station 2018R4 (background) and Snow Buoy 2018S69 (foreground) (photo: Mario Hoppmann, AWI), (**E**) ground-based electromagnetic induction sounding device (GEM-2) (photo: Christian Katlein, AWI).*

be found in Katlein et al. (2017). Radiation stations and Snow Buoys are often deployed in the vicinity where ROV surveys are performed.

Terrestrial laser scanner (**Figure 2.13B**): A terrestrial laser scanner (VZ-400i, RIEGL, Horn, Austria, 1550 nm) was used to scan the sea-ice surface and to achieve topography and snow depth. A laser scanner is usually mounted on a tripod $\sim$2 m above the surface. Different scan positions are distributed around or along the study area. The transmitter of the laser scanner emits laser pulses at the speed of light which are reflected at the target surface and directed back to the receiver. By measuring the time between emitting and detecting the laser pulse, the time of flight, the surface topography relative to the scanner position based on the velocity of the pulses in the air is recorded (RIEGL, 2013). The individual scans are registered each to a master scan position using fixed cylindrical retro-reflectors (10 mm diameter) as registration points to create a full point cloud of the area using for example the RiSCAN PRO software. At least three reflectors are necessary to register scans. It is not advisable to perform measurements on windy days as the stabilization of the scanner (roll and pitch) and with that good data

retrieval cannot be assured. Unstable scanner positions affect the standard deviation of the tie points as calculated during registration. Laser reflections from snow fall need to be removed manually and, thus, measurements during severe snow fall should not be performed.
The scan pattern panorama 20 with an angular resolution of 20 mdeg (0.35 mrad) and a scan time of 180 s was used for measurements presented in this dissertation. At 20 m this corresponds to a 7 mm and at 50 m to a 17 mm resolution. For most applications a laser pulse repetition rate of 1200 kHz with a theoretical maximum measurement range of 250 m is used. However, due to the snow conditions and the laser wavelength, the real maximum range can be significantly lower.
Snow depth measurements using a tape or a Magnaprobe should be performed on the same day the laser is operating, ideally during the same time. Those measurements can be used for reference to derive the snow depth from the surface topography measured by the laser scanner. Thereby should be ensured that the Magnaprobe does not penetrate into the surface scattering layer of the ice.
Magnaprobe (**Figure 2.13C**): Snow depth point measurements can be performed using a Magnaprobe (Snow-Hydro, Fairbanks, AK, USA, Sturm and Holmgren, 2018) with an accuracy of near zero for hard ground and ± 0.05 m for soft ground. On sea ice, the basket that rides on the metal pole of the Magnaprobe might penetrate into the snow layer. The positions of the measurements are recorded with a enabled GPS and is accurate to ± 2.5 m (Sturm and Holmgren, 2018).
Radiation stations (Richter-Menge et al., 2006; Nicolaus et al., 2010b, **Figure 2.13D**): Those radiation stations consist of three RAMSES-ACC hyper-spectral radiometers. They measure the incoming irradiance on the surface, the reflected irradiance by the surface, and the transmitted irradiance. In addition, the radiation stations can contain an ultrasonic snow pinger (Max Botix, Brainerd, MN, USA) which records changes in snow accumulation and drift with an accuracy of 1 cm. A tiltmeter monitors the stability of the station and is useful to correct radiation measurements. Battery and electronics are either stored in each a peli case or combined within one case. Often, a camera is installed in the electronics case which takes a picture every 4 hours. With that the station and the close vicinity are documented to get an impression of the weather around and identify possible causes of failure, e.g., polar bear or fox. The temporal resolution for the radiometers can vary between 10 min and one hour. The data are sent on-shore via Iridium.
Snow Buoys (Nicolaus et al., 2021, **Figure 2.13D**): Continuous time series of snow depth were measured by Snow Buoys (Nicolaus et al., 2021). A Snow Buoy consists of four ultrasonic snow pingers. The snow depth is calculated from the distance to the surface measured by the pingers and the initial *in-situ* snow depth measured during deployment. Temperature and pressure sensors are attached providing information on the weather and onset dates of melt

and freeze-up. The temporal resolution for the data is one hour. The data are sent on-shore via Iridium.

Ground-based electromagnetic induction sounding devices (EM31-SH, Geonics Limited, Mississauga, ON, Canada, Haas et al., 2008; 2017, not shown, and GEM-2, Geophex Ltd, Raleigh, NC, USA, Hunkeler, 2016, **Figure 2.13E**): Ground-based electromagnetic induction sounding devices (Haas et al., 2008; Hunkeler, 2016; Hunkeler et al., 2016; Haas et al., 2017) are used to detect the distance between the device on the sea-ice surface and the interface between sea ice and ocean, and, thus, estimate the total ice thickness (snow depth + ice thickness). The two ground-based electromagnetic induction sounding devices used in this dissertation are based on the same principle of electromagnetic fields in small coil systems. The devices consist of a transmitter and receiver coil. A primary magnetic field is generated in the transmitter and a secondary field is induced in the conductive sea-ice surface. Both fields superimpose and are measured by the receiver. Commonly, the ratio between secondary and primary field is evaluated. The secondary field is described by a real and imaginary component. Its unit is ppm (parts per million). The penetration depth depends on the oeprating frequency, the electrical conductivity, the magnetic permeability, and the electric permittivity of the sea ice and underlying ocean. Due to the differences in electrical conductivity between sea ice and sea water the total ice thickness can be retrieved after calibration of the instruments. While the GEM-2 uses multiple operating frequencies between 0.45 kHz and 63.03 kHz, the EM31-SH uses one frequency of 9.80 kHz.

3. Snow depth retrieval on Arctic sea ice using under-ice hyperspectral radiation measurements

This chapter has been published as

Anhaus, P., Katlein, C., Nicolaus, M., Arndt, S., Jutila, A., and Haas, C. (2021): Snow Depth Retrieval on Arctic Sea Ice Using Under-Ice Hyperspectral Radiation Measurements, *Frontiers in Earth Science, 9*, doi:10.3389/feart.2021.711306.

3.1 Abstract

Radiation transmitted through sea ice and snow has an important impact on the energy partitioning at the atmosphere-ice-ocean interface. Snow depth and ice thickness are crucial in determining its temporal and spatial variations. Under-ice surveys using autonomous robotic vehicles to measure transmitted radiation often lack coincident snow depth and ice thickness measurements so that direct relationships cannot be investigated. Snow and ice imprint distinct features on the spectral shape of transmitted radiation. Here, we use those features to retrieve snow depth. Transmitted radiance was measured underneath landfast level FYI using a remotely operated vehicle in the Lincoln Sea in spring 2018. Colocated measurements of snow depth and ice thickness were acquired. Constant ice thickness, clear water conditions, and low in-ice biomass allowed us to separate the spectral features of snow. We successfully retrieved snow depth using two inverse methods based on under-ice optical spectra with 1) normalized difference indices and 2) an idealized two-layer radiative transfer model including spectral snow and sea ice extinction coefficients. The retrieved extinction coefficients were in agreement with previous studies. We then applied the methods to continuous time series of transmittance

and snow depth from the landfast FYI and from drifting, melt-pond covered MYI in the Central Arctic in autumn 2018. Both methods allow snow depth retrieval accuracies of approximately 5 cm. Our results show that atmospheric variations and absolute light levels have an influence on the snow depth retrieval.

3.2 Introduction

The Arctic sea ice is undergoing rapid and tremendous changes during the last decades (Meredith et al., 2019). The extent of sea ice is shrinking (Serreze et al., 2007; Stroeve et al., 2012). Old thick MYI is replaced by younger (e.g., Maslanik et al., 2007; Stroeve and Notz, 2018) and thinner FYI (Haas et al., 2008; Kwok and Rothrock, 2009). Those changes are mainly driven by atmospheric (e.g., Graversen et al., 2008) and ocean warming (e.g., Steele et al., 2010). As the sea-ice cover shrinks, less area is available where snow can deposit. Due to its high reflectivity, snow plays a key role in the energy balance of the sea ice (Webster et al., 2018). It determines the amount of radiation transmitted through sea ice (e.g., Perovich, 2007; Nicolaus et al., 2013), and has a strong effect on the surface albedo (e.g., Perovich and Polashenski, 2012). Delays in sea-ice formation due to a prolonged melt season (e.g., Markus et al., 2009) reduce early snow accumulation. To further investigate and understand the solar partitioning and with that assess and monitor the changes in the Arctic sea ice, relationships between the under-ice solar radiation and snow depth must be established.

Under-ice radiation can be measured using remotely operated vehicles (ROVs, e.g., Nicolaus et al., 2012, Katlein et al., 2015, Arndt et al., 2017, Meiners et al., 2017, Katlein et al., 2019, Lange et al., 2019), towed platforms (Castellani et al., 2020), and autonomous underwater vehicles (AUVs, e.g., Wulff et al., 2016). Using such platforms minimizes the destruction of the sea-ice surface while measuring. Hardly or not at all accessible, undersampled, and heterogeneous ice-covered areas such as very thin, newly formed ice, and open and refreezing leads can be accessed and studied on large scales and in a reasonably short operation time. Time series of under-ice radiation at local fixed points and coincident snow depth and ice thickness can be collected by autonomous measuring system drifting with the sea ice (Richter-Menge et al., 2006; Nicolaus et al., 2010b, 2021). However, for many ROVs and AUVs surveys coincident snow depth measurements are not available, especially when the vehicles are far away from their deployment site.

Solar radiation penetrating through sea ice is scattered or absorbed (Perovich, 1996). This attenuation depends strongly on snow, sea ice, water, and in-ice and water biomass and their physical properties (e.g., Mundy et al., 2005; Katlein et al., 2015; Smith and Baker, 1981; Arrigo et al., 1991; Mundy et al., 2007). Those properties determine the magnitude and the spectral

shape of the under-ice radiation and leave distinct features in the spectra at specific wavelengths (e.g., Mundy et al., 2007; McDonald et al., 2015). These distinct features can be used to retrieve snow and ice properties from under-ice radiation.

Normalized difference indices (NDIs) describe the spectral shape of under-ice radiation and can be correlated with the properties of snow, ice, water, and biomass. They have been successfully used to retrieve chlorophyll a concentration in the Arctic (Mundy et al., 2007; Campbell et al., 2014; Lange et al., 2016; Castellani et al., 2020) and Antarctic (Melbourne-Thomas et al., 2015; Meiners et al., 2017; Wongpan et al., 2018; Castellani et al., 2020; Cimoli et al., 2020). Relationships between the NDIs and snow depth have been established to investigate the potential to retrieve snow depth (Mundy et al., 2007; Melbourne-Thomas et al., 2015; Arndt et al., 2017; Wongpan et al., 2018). However, no attempts have been made yet to apply those findings and to retrieve snow depth as such. Inverse radiative transfer (RT) modelling can also be used to retrieve snow and ice properties through the dependency of under-ice radiation on the spectral extinction coefficients (e.g., McDonald et al., 2015; Arndt et al., 2017).

Recent remote sensing snow depth retrieval methods provide snow depth over large regions in the Arctic using space-borne passive microwave radiometry (e.g., Rostosky et al., 2018), dual-band satellite altimetry (e.g., Guerreiro et al., 2016; Lawrence et al., 2018), and airborne ultrawideband microwave radar (e.g., Jutila et al., 2021). However, the temporal and spatial scales of those space-borne retrievals are not applicable for colocation with small scale, localized under-ice radiation measurements. While it is easy to measure snow depth directly for small areas, e.g., using a Magnaprobe (Sturm and Holmgren, 2018), simultaneous and repeated under-ice radiation measurements are not possible due to the destruction of the area through measuring snow depth.

Here, we utilize two non-destructive optical methods to inversely retrieve snow depth from under-ice radiation measurements. The methods are applied to landfast level FYI and to drifting, melt-pond covered MYI. We present colocated snow depth and ice thickness measurements along with under-ice hyperspectral radiation data from an ROV. Based on these data, we find the best wavelength pairs to retrieve snow depth from NDIs. We also retrieve snow depth by inverting an idealized two-layer RT model and snow and sea ice spectral extinction coefficients in the wavelength range between 400 nm and 700 nm. The discrepancies between directly measured and retrieved snow depth are the criteria to evaluate the performance of the two methods. We discuss how those methods could be applied to current sea ice research with a focus on technological advances.

3.3 Material and methods

3.3.1 Study sites

The data presented in this study were collected during two field campaigns (**Figure 3.1**). The Multidisciplinary Arctic Program – Last Ice Area (MAPLI18) campaign was conducted on landfast level FYI in the Lincoln Sea off the coast of Ellesmere Island near the Canadian Forces Station Alert, Canada, in spring 2018. The Arctic Ocean 2018 (AO18) MOCCHA – ACAS – ICE campaign was conducted with the Swedish Icebreaker *Oden* on drifting, melt-pond covered MYI close to the geographic North Pole in autumn 2018.
For the following description of data and results we refer only to MAPLI18 if not otherwise stated. Snow depth, total sea ice thickness (ice thickness plus snow depth), and transmitted radiance were measured on and under an approximately 120 m x 80 m landfast level FYI patch (**Figure 3.1B**). The measurements were performed along a 100 m transect and across the entire patch. At the marker locations M0 to M10, plastic poles were put through drilled holes in the ice to ease under-ice navigation and ensure correct colocation of the data. Adjacent to the FYI patch was deformed MYI (Lange et al., 2019).

3.3.2 Snow depth and ice thickness

The surface topography of the FYI patch was measured with a terrestrial laser scanner (VZ-400i, RIEGL, Horn, Austria). The laser scanner was mounted on a tripod $\sim$2 m above the surface. Scan positions were distributed at the marker locations and along the transition to the deformed ice spaced 10-40 m apart (**Figure 3.1B**). The individual scans were each registered to a master scan position using three space-fixed cylindrical retro-reflectors (RF1-3) in the RiSCAN Pro software. Subsequently, a full point cloud was created with a mean horizontal resolution of 5 cm and a mean vertical accuracy of 2 cm caused by uncertainties in scanner orientation. The point clouds for three different days were each manually rotated for horizontal alignment with the marker locations. Snow depth was calculated from the surface topography by subtracting the height of the reflector center of RF2 above the ice surface (**Table 3.1**). The snow depth could be differentiated from the ice by assuring that neither the rod of the reflector nor the tripod penetrated deep into the surface scattering layer between ice and snow. Using the length of the reflector rod allowed the extraction of the snow depth for reference at this particular location within the RiSCAN Pro software. Snow depths exceeding 0.6 m close to the deformed ice area were removed as for higher snow loads the assumption of level sea ice was questionable. More details on the surface topography measurements and how snow depth was derived can be found in the data repository doi:10.1594/PANGAEA.932594.

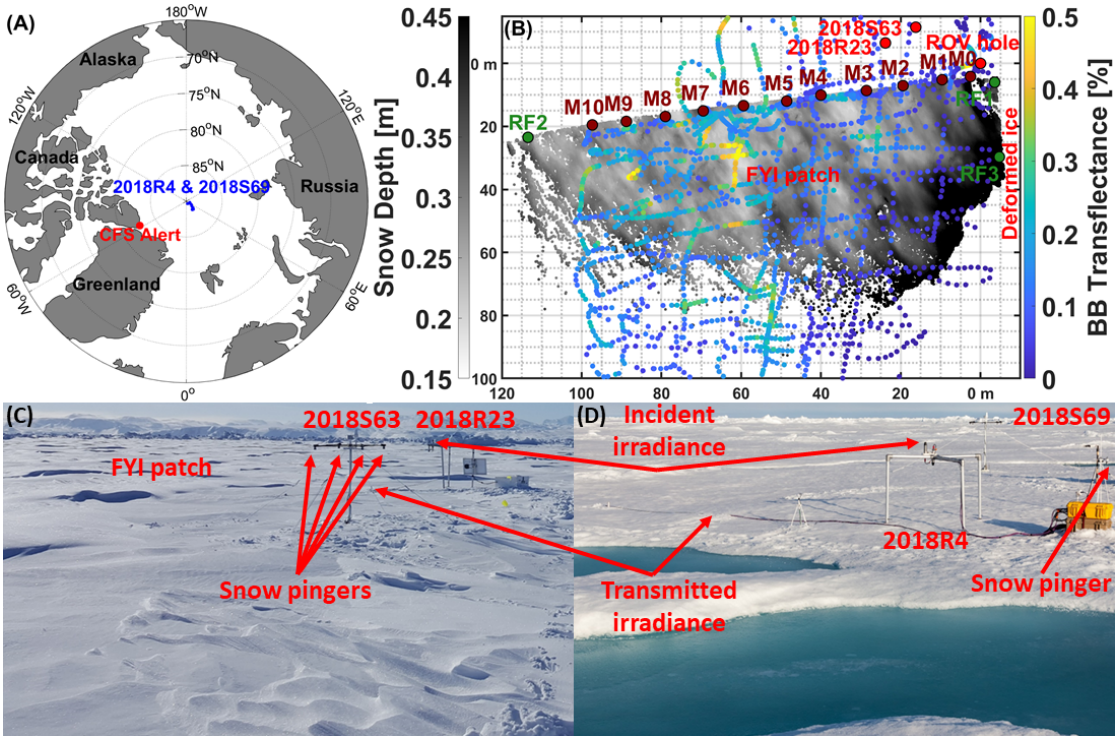

Figure 3.1: *(**A**) Location of the MAPLI18 campaign close to the Canadian Forces Station (CFS) Alert in the Lincoln Sea and the drift of the radiation station 2018R4 and the snow buoy 2018S69 close to the geographic North Pole during the AO18 campaign. (**B**) Map of the FYI patch during MAPLI18 displaying snow depth in m derived from the terrestrial laser scanner as measured on 23 May (grey scale). Overlaid is the broadband (BB) transflectance in % (colour scale) measured by the ROV on 22 May. Circles indicate the marker locations M0 to M10 (dark red), the access hole of the ROV in the ice (red), and the locations of the radiation station 2018R23 and the Snow Buoy 2018S63 (red). RF1-3 (green circles) are the reflectors used to process the laser scanner data. (**C**) Radiation station 2018R23 and Snow Buoy 2018S63 as of 5 May 2018. (**D**) Radiation station 2018R4 and Snow Buoy 2018S69 as of 20 August 2018 (photo: Mario Hoppmann, AWI).*

Table 3.1: *Snow depth obtained in drill holes at the marker locations and with a laser scanner. Std is the first standard deviation of the mean snow depth and N the number of measurements. The modes were read from histograms with 1 cm bin width.*

Data sub set	Method	N	Min [m]	Max [m]	Mean [m]	Std [m]	Median [m]	Mode [m]
Marker 05 May	Drill hole	11	0.07	0.46	0.20	0.13	0.16	0.12
Transect 09 May	Laser scanner	163	0.10	0.27	0.17	0.05	0.15	0.15
Patch 09 May	Laser scanner	491	0.09	0.31	0.18	0.05	0.18	0.16
Marker 12 May	Laser scanner	43	0.11	0.54	0.20	0.10	0.18	0.13
Transect 12 May	Laser scanner	162	0.11	0.51	0.20	0.06	0.18	0.19
Patch 12 May	Laser scanner	443	0.11	0.51	0.20	0.05	0.20	0.21
Marker 23 May	Laser scanner	35	0.21	0.60	0.28	0.07	0.27	0.25
Transect 23 May	Laser scanner	110	0.20	0.60	0.28	0.06	0.27	0.24
Patch 23 May	Laser scanner	955	0.20	0.59	0.30	0.06	0.29	0.29

Snow depth point measurements with a horizontal resolution between 1 m and 3 m were obtained using a Magnaprobe (Snow-Hydro, Fairbanks, AK, USA, Sturm and Holmgren, 2018) with an accuracy of 1 cm. The position of the measurements was recorded with an integrated GPS with an accuracy of ± 2.5 m (Sturm and Holmgren, 2018). The Magnaprobe measurements were used to validate the snow depths derived from the laser scanner. Laser scanner snow depths were averaged around Magnaprobe measurements. Differences in modal snow depths between Magnaprobe and laser scanner were with 0-2 cm within the laser scanner accuracy.
Total ice thickness was measured with a ground-based electromagnetic induction sounding device (EM31-SH, Geonics Limited, Mississauga, ON, Canada, Haas et al., 1997; 2017). The EM31-SH measurements were compared against measurements from other drill hole locations (not shown) for proper calibration on both FYI and MYI following the description from Haas et al. (1997, 2017). The EM31-SH was placed on a sledge and dragged across the ice and has a vertical accuracy of 0.10 m. The ice thickness was then calculated by subtracting the laser scanner snow depth from the total ice thickness. The ice thickness was assumed to be level indicated by underwater images (**Figure 3.2A**), small standard deviations in ice thickness (**Table 3.2**), mean and modal thickness agreeing to within ± 0.15 m which is close to ± 0.10 m found by Rabenstein et al. (2010), multiple drillings and ice investigations in the area, and by the area extent of at least 100 m in length (**Figure 3.1B**). We further assumed the thickness to be constant during the study period because it did not vary by more than 0.10 m across the whole patch (**Table 3.2**).
In-situ snow depth, ice thickness, draft, and freeboard were measured at drill holes at the

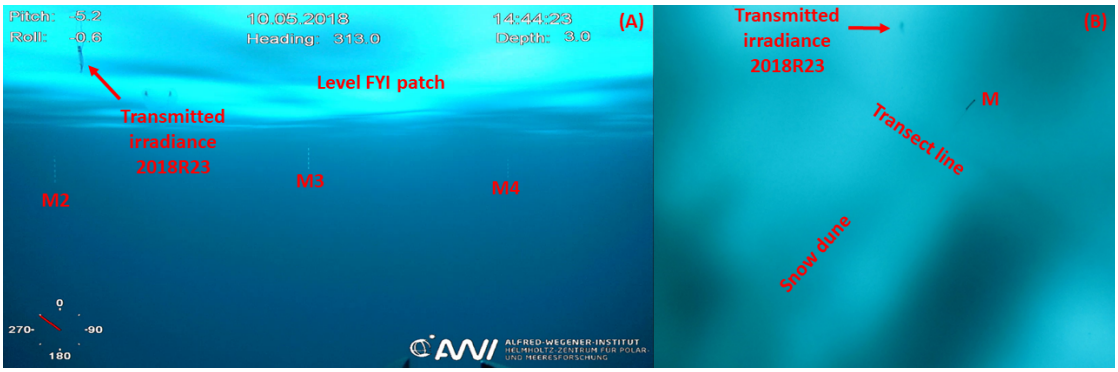

Figure 3.2: *(**A**) Underwater image of the level FYI patch on 10 May as extracted from a video taken by the ROV HD camera. (**B**) Underwater upward looking still image at 55.6 m depth as taken by a 14.1-megapixel Tiger Shark camera (Imenco, Norway) attached to the ROV on 12 May.*

Table 3.2: *Drill hole ice thickness and draft (in brackets) at the marker locations and EM31-SH ice thickness. Std is the first standard deviation of the respective mean and N the number of measurements. The modes were read from histograms with 0.10 m bin width.*

Data sub set	Method	N	Min [m]	Max [m]	Mean [m]	Std [m]	Median [m]	Mode [m]
Marker 05 May	Drill hole	11 (11)	1.49 (1.37)	1.68 (1.58)	1.57 (1.48)	0.07 (0.07)	1.57 (1.48)	1.57 (1.40)
Transect 10 May	EM31-SH	110	1.43	1.60	1.54	0.05	1.55	1.60
Transect 24 May	EM31-SH	56	1.39	1.54	1.45	0.04	1.46	1.50
Patch 24 May	EM31-SH	246	1.08	1.58	1.35	0.10	1.37	1.50

marker locations using a tape measure.

3.3.3 Under-ice radiation

Horizontal profiles of under-ice spectral radiance were measured by a RAMSES-ARC hyperspectral radiometer (320-950 nm, TriOS Mess- und Datentechnik GmbH, Rastede, Germany). The radiometer was mounted to an M500 ROV (Ocean Modules, Åtvidaberg, Sweden, Katlein et al., 2017). The ROV was lowered into the water through a 1.5 m x 1.5 m hole in the ice and operated horizontally along the ice bottom. The hole and the control system for the ROV were covered by a heated tent. To take into account atmospheric variability, the transmitted radiance was normalized by the incident downwelling planar irradiance recorded at the surface by a RAMSES-ACC radiometer. The ratio of transmitted radiance $I_T(\lambda)$ and incident irradiance $E_S(\lambda)$ was defined as transflectance: $t_f(\lambda) = I_T(\lambda)/E_S(\lambda)$ (Nicolaus and Katlein, 2013). The spectral resolution of the radiometers was 3.3 nm, which was interpolated to a common wavelength grid with 1 nm spacing (Nicolaus et al., 2010a). The analysis of the transflectance

was limited to wavelengths between 400 nm and 700 nm, ROV pitch and roll within $\pm 10°$, and depths shallower than 2 m below the sea level. We manually removed some noisy spectra.
For under-ice navigation of the ROV an acoustic long baseline positioning system (Pinpoint Linkquest, San Diego, CA, USA) was used. Manual post-processing of the position was required to remove distortion in positioning probably caused by local sound speed differences. To correct this distortion, the position of the ROV at the marker locations as recorded by the positioning system and as viewed by the ROV high definition zoom video camera (Surveyor WAHD, Bowtech, **Figure 3.2A**) was manually aligned with the marker locations measured by a handheld GPS at the surface to obtain scaling factors for correcting the position (**Figure 3.1B**). The opening angle of the radiance radiometer β was about 7°. Based on this value, we determined 1.5 m as the approximate footprint radius R of the area from which the radiometer detected radiance through the surface based on $R = D \cdot \tan(\beta/2)$ (Katlein, 2012), with D as the distance from the radiometer to the surface. It was determined by the mean snow depth, ice thickness, and draft at the marker locations (**Tables 3.1** and **3.2**). We assumed a 1:1 radius-ice thickness relationship, conservative scattering, and a diffuse light source. Following results from (Petrich et al., 2012a), 50-60% of the photons reaching the radiometer would originate from a 1.5-2.0 m radius. The footprint was then used to colocate transflectance, snow depth, and ice thickness measurements.

3.3.4 Continuous radiation and snow depth measurements

Continuous time series measurements of transmitted and incident irradiance were measured with RAMSES-ACC radiometers mounted on the radiation stations 2018R23 from 5 to 21 May during MAPLI18 and on 2018R4 from 27 August to 18 September during AO18 (**Figure 3.1**). The radiometer that measured the transmitted irradiance was hanging in the water at a distance to the ice bottom of 0.5 m. During the same periods time series of snow depth were measured by two Snow Buoys (Nicolaus et al., 2021), 2018S63 during MAPLI18 and 2018S69 during AO18 (**Figure 3.1**). Each snow buoy consisted of four ultrasonic snow pingers (Max Botix, Brainerd, MN, USA) with an accuracy of 1 cm. In addition, a single pinger was attached to the radiation station 2018R4 which was deployed 10-15 m away from the Snow Buoy 2018S69. The snow depth was calculated from the distance to the surface measured by the pingers and the initial *in-situ* snow depth. Data gaps from the 2018R4 pinger were replaced by data from previous time stamps. The temporal resolution for both radiation stations and Snow Buoys were one hour.

3.3.5 Normalized difference indices

The distinct features caused by the snow depth in the spectral shape of the transflectance was used as a non-invasive method to retrieve snow depth (**Figure 3.3**). We assumed that the effect of snow on the transflectance can be separated from the effect of the ice because the ice was level and the thickness did not vary by more than 0.10 m across the whole patch. Thus, in our dataset ice thickness does not influence retrieved snow depths, however our dataset only covers a small thickness variation to verify this. The absorption by water and phytoplankton was neglected because the visibility in the water was above 50 m (i.e. very clear water, **Figure 3.2B**) and Lange et al. (2019) reported low in-ice chlorophyll *a* biomass of 0.23 mg m^{-2} to 2.56 mg m^{-2} in the bottom and 1.42 $\pm$ 0.62 mg m^{-2} overall. Absorption by water close to the ice bottom was measured by a hyperspectral extinction sensor (VIPER-G2, TriOS, Rastede, Germany, Katlein et al., 2017) attached to the ROV. On average absorption was 0.06 m^{-1} at 436 nm and 0.03 m^{-1} at 620 nm on 12 May while on 22 May it was 0.07 m^{-1} at 436 nm and 0.03 m^{-1} at 620 nm. The maximum distance between radiometer and ice bottom based on the operational depth of the ROV and the mean sea-ice draft was 0.62 m (**Section 3.3.3** and **Table 3.2**). Neglecting absorption by water resulted in relative errors ranging between 1.9% and 4.4% in transflectance measurements. Katlein et al. (2016) used a 3D model to investigate the effects of a spatially inhomogeneous sea-ice cover and of water absorption on under-ice radiation. They recommend to use radiance instead of irradiance for spatial variability studies and to rather discard measurements taken at greater distance to the ice bottom (e.g., > 1.5 m, Lange et al., 2016) then correcting measurements for water absorption as this introduces unknown errors due to unknown geometry that cannot be quantified and thus, no gain in precision. We computed NDIs as described by Mundy et al. (2007) using ROV-based transflectance t_f for all wavelength pairs λ_1 and λ_2 between 400 nm and 700 nm:

$$NDI(\lambda_1, \lambda_2) = \frac{t_f(\lambda_1) - t_f(\lambda_2)}{t_f(\lambda_1) + t_f(\lambda_2)} \tag{3.1}$$

t_f was measured along the transect on May 12. The Pearson correlation coefficients between NDIs and measured snow depth were plotted for all wavelength pairs to construct a spectral correlation surface (**Figure 3.4**). The snow depth was also measured along the transect on May 12. The NDIs with the wavelength pairs λ_1 and λ_2 that showed the highest correlation with measured snow depth were used to establish a linear regression between NDIs and measured snow depth. The regression functions for different wavelength pairs were then used to retrieve snow depth from the other dates than 12 May using NDIs calculated from transflectance measurements.

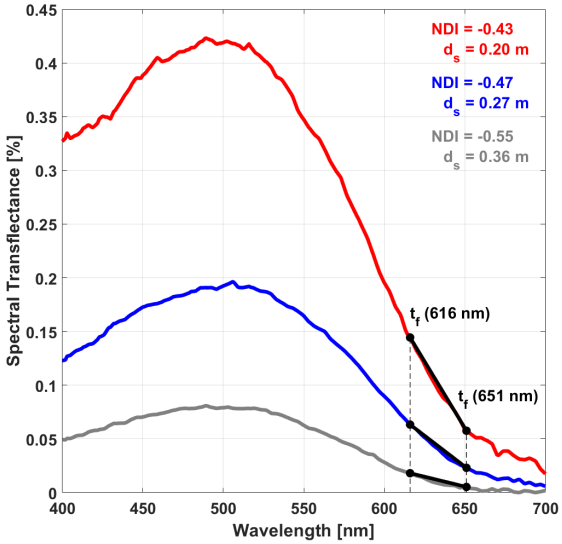

Figure 3.3: *Spectral transflectance in % for three different snow depths d_s of 0.20 m (red), 0.27 m (blue), and 0.36 m (grey). NDIs (**Equation 3.1**) are given in numbers to indicate the different slopes of the transflectance tf between 651 nm and 616 nm.*

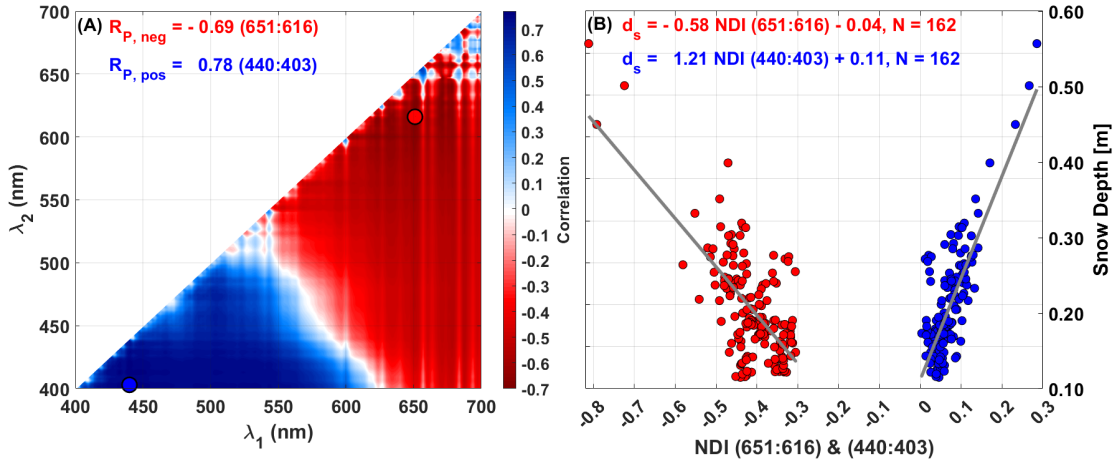

Figure 3.4: *(**A**) Spectral correlation surface constructed from the Pearson correlation coefficients R_p between the NDIs and measured snow depth for all possible wavelength pairs λ_1 and λ_2. Transflectance and laser scanner snow depth were measured along the transect on May 12. (**B**) Corresponding linear regression between the NDIs for the wavelength pairs yielding the highest correlations (circles in **A**) and the snow depth. The regression functions used to retrieve the snow depth d_s are also provided. N is the number of measurements used.*

3.3.6 Radiative transfer model

In addition to the NDI method, we applied a multiple exponential regression model from the MATLAB^{TM} curve fitting toolbox with a non-linear least square Trust-Region algorithm (Sorensen, 1982) to approximate radiative transfer (RT) in sea ice. In this approach, the spectral transflectance transmitted through a two-layer system consisting of snow and sea ice decays exponentially with snow depth d_s and ice thickness d_i described by the spectral snow and sea ice extinction coefficients $k_s(\lambda)$ and $k_i(\lambda)$:

$$t_f(\lambda, d_i, d_s) = i_0 \exp\left(-k_i(\lambda)\, d_i - k_s(\lambda)\, d_s\right) \tag{3.2}$$

The value $i_0 = 0.35$ was used which is the fraction of the incident net short-wave radiation that is not reflected back at the surface or absorbed within the snow under cloudy skies for white bare ice by (Grenfell and Maykut, 1977). This approximation (**Equation 3.2**) has been frequently used for large scale modeling, but disregards effects of strong multiple scattering in snow and ice. Extinction by in-ice biomass and absorption by water were neglected as well as the effects of any impurities within the ice. In a first step, measured t_f was fitted to measured d_s and d_i resulting in retrieval of $k_s(\lambda)$ and $k_i(\lambda)$. ROV-based t_f, laser scanner d_s, and EM31-SH d_i used for the retrieval were measured at the marker locations (**Figure 3.1B**) on 22, 23, and 24 May, respectively. In a second step, the retrieved $k_s(\lambda)$ and $k_i(\lambda)$ were fitted to measurements of t_f collected on other dates than 22 May to inversely retrieve snow depth for other dates than 23 May.

3.4 Results

3.4.1 Snow depth and sea-ice thickness

We studied the snow stratigraphy close to the Snow Buoy 2018S63 and the radiation station 2018R23 on 12 May and at the end of the transect (close to M10) on 22 May (**Figures 3.1B**, **C**). We observed typical characteristics of snow on Arctic sea ice. Closest to the snow-ice interface was a poorly bonded layer of depth hoar underlying a wind slab layer of varying hardness. Between them, we found a thin layer of melt forms or even an ice lens. The topmost layer consisted of very soft, new snow. However, for further analysis we assumed the snow being one bulk layer.

Snow dunes were present across the FYI patch which caused spatial variability (**Figure 3.1B**). A wind-induced snow redistribution event took place between 9 and 10 May, also reported by Lange et al. (2019). This caused an increase in mean and modal snow depth along the transect and across the patch between 9 and 12 May (**Table 3.1**). Significant snow fall occurred on 16, 23, and 24 May. This caused further increases of mean and modal snow depth as evident on 23

Table 3.3: *Spectral snow $k_s(\lambda)$ and sea ice $k_i\lambda)$ extinction coefficients as inversely retrieved using a two-layer RT model. The transflectance, snow depth, and ice thickness used for the retrieval were measured at the marker locations on 22, 23, and 24 May, respectively. N is the number of measurements used and BB are the broadband values.*

Extinction coefficient	N	Min	Max	Mean	Median	Std	Mode	BB
		m^{-1}	m^{-1}	m^{-1}	m^{-1}	m^{-1}	m^{-1}	m^{-1}
$k_s(\lambda)$	27	9.9	14.4	11.2	10.9	1.1	10.4	10.9
$k_i(\lambda)$	27	1.5	3.5	1.9	1.7	0.5	1.6	1.7

May.

The mean standard deviation of the laser scanner snow depths within a radius of 1.5 m around every transflectance measurement was 5 cm. Hence, we used it as a tolerance value to evaluate the method performance that can be achieved using optical measurements in this study.

The difference between mean EM31-SH ice thicknesses along the transect measured on 10 and 24 May was within the measurement error of 0.10 m (**Table 3.2**). Modal ice thicknesses measured at the drill holes at the marker locations on 5 May and with the EM31-SH along the transect on 10 and 24 May and across the patch on 24 May were also within the error. Thus, we assume that the ice thickness did not change significantly during the observation period.

3.4.2 Normalized difference indices, radiative transfer model, and extinction coefficients

Strong Pearson correlation coefficients (R_P) between NDIs and snow depth displayed in the spectral correlation surface indicated that the snow depth explained the majority of the variability in the transflectance for the two wavelength pairs 651:616 nm and 440:403 nm (**Figure 3.4A**). The highest negative correlation was found for the wavelength pair 651:616 nm and the highest positive correlation for 440:403 nm. The snow depth explained 69% and 78% of the variability in the transflectance at those wavelengths along the transect, respectively (**Figure 3.4A**). We used both wavelength pairs to find the best snow depth retrieval using the NDI method. (**Figure 3.4B**).

The spectral snow extinction coefficients retrieved from inverse RT modeling decreased from 400 nm to their minimum at around 550 nm and then increased to a maximum at 661 nm (**Figure 3.8A**). The sea-ice extinction coefficients remained nearly constant between 400 nm and 520 nm at around 1.5 m^{-1}, and increased above 550 nm to their maximum value of 3.5 m^{-1} at 700 nm (**Figure 3.8B**, **Table 3.3**).

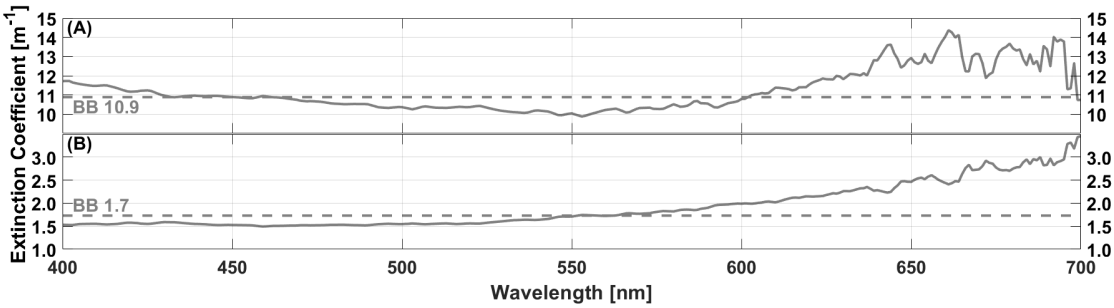

Figure 3.5: *Spectral snow $k_s(\lambda)$ (**A**) and sea ice $k_i(\lambda)$ (**B**) extinction coefficients as retrieved by inversion of a two-layer RT model. Transflectance, laser scanner snow depth, and EM31-SH ice thickness used for the retrieval were measured at the marker locations on 22, 23, and 24 May, respectively. The broadband values (BB) are indicated by the numbers and the dashed lines.*

Snow influences and attenuates radiation most efficiently at longer wavelengths between 600 nm and 700 nm as expressed in high spectral snow extinction coefficients (**Figure 3.8B**). The extinction coefficients are also high between 400 nm and 450 nm indicating that snow also influences radiation at those wavelengths. As the transflectance increases with wavelength from 403 nm to 440 nm (**Figure 3.3**), correlation coefficients at those wavelengths are positive while between 616 nm and 651 nm the transflectance decreases with wavelength resulting in negative correlation coefficients.

3.4.3 Spatial variability of measured and retrieved snow depths

The spatial variability in snow depth during MAPLI18 was well reproduced using the NDI method (**Figure 3.6**). The magnitude of the retrieved snow depths agreed with the direct snow depth measurements (**Table 3.4**). On 9 May, the NDI method achieved root mean square errors (RMSEs) between measured and retrieved snow depths below or slightly exceeding the tolerance of 5 cm (**Table 3.4**). The percentage of the direct snow depth measurements that were $\pm$ 5 cm (tolerance) of the retrieved snow depths is referred to as agreement and was between 65% and 77% on 9 May. The snow depth was overestimated but with deviations between the modal snow depths, Δmode, within the tolerance. On 23 May, the achieved RMSEs were significantly above the tolerance. The agreements were between 17% and 58% and the snow depth was underestimated with Δmodes of 3 cm and 8 cm.

To summarize, the NDI method with the wavelength pairs 651:616 nm and 440:403 nm performed well in reproducing the spatial variability and the magnitude of the measured snow depth with a combined mean RMSE of 6.6 cm.
The spectral snow and sea-ice extinction coefficients (**Figure 3.8**, **Table 3.3**) were implemented in the RT model (**Equation 3.2**) together with measured transflectance to retrieve snow depth

Table 3.4: *Comparison of snow depth retrieval using the NDI method. In bold are the retrieved snow depths that are within the tolerance of ± 5 cm. The modes were read from histograms with 1 cm bin width. N is the number of measurements used.*

Direct measurements	N	Wavelength pair [nm]	Agreement [%]		RMSE [cm]	Min [cm]	Max [cm]	Mean [cm]	Median [cm]	Std [cm]	Mode [cm]
			± 5 cm	± 50%							
Transect 09 May	143					0.10	0.27	0.17	0.15	0.05	0.15
		651:616	**77**	**92**	**4.3**	**0.14**	0.34	**0.20**	**0.19**	**0.04**	**0.18**
		440:403	**71**	**88**	**4.9**	**0.13**	0.34	**0.21**	**0.19**	**0.05**	**0.18**
Patch 09 May	491					0.09	0.31	0.18	0.18	0.05	0.16
		651:616	**71**	**91**	**4.7**	**0.13**	0.42	**0.20**	**0.19**	**0.04**	**0.21**
		440:403	**65**	**88**	5.4	**0.13**	0.42	**0.21**	**0.20**	**0.05**	**0.21**
Transect 23 May	110					0.20	0.60	0.28	0.27	0.06	0.24
		651:616	45	**97**	7.7	0.14	0.52	0.22	0.21	**0.05**	**0.21**
		440:403	**58**	**99**	6.5	**0.16**	0.38	**0.23**	**0.23**	**0.04**	**0.21**
Patch 23 May	955					0.20	0.59	0.30	0.29	0.06	0.29
		651:616	17	**98**	11.0	0.08	0.53	0.21	0.20	**0.04**	0.21
		440:403	32	**99**	8.2	0.13	0.85	0.24	0.22	**0.07**	0.21
2018S63											
05 – 21 May											
hourly resolution	379					0.22	0.32	0.28	0.28	0.02	0.29
daily mean	17					0.22	0.30	0.27	0.28	0.02	0.30
hourly resolution		651:616	**59**	**100**	**4.6**	**0.20**	**0.29**	**0.23**	**0.24**	**0.01**	**0.24**
daily mean			**53**	**100**	**4.4**	**0.21**	**0.25**	**0.23**	**0.24**	**0.01**	**0.25**
hourly resolution		440:403	**96**	**100**	**2.3**	**0.18**	**0.30**	**0.26**	**0.27**	**0.02**	**0.29**
daily mean			**100**	**100**	**2.2**	**0.18**	**0.28**	**0.26**	**0.27**	**0.03**	**0.29**
2018S69											
27 Aug – 18 Sep											
hourly resolution	515					0.02	0.11	0.06	0.05	0.02	0.05
daily mean	23					0.03	0.10	0.06	0.06	0.02	0.05
hourly resolution		440:403	37	10	10.9	**0.02**	0.65	0.13	**0.10**	0.09	0.11
daily mean			35	0	8.8	**0.08**	0.33	0.13	**0.10**	**0.07**	0.11
2018R4											
snow pinger											
27 Aug – 18 Sep											
hourly resolution	515					0.04	0.29	0.09	0.07	0.07	0.08
daily mean	23					0.05	0.26	0.10	0.07	0.07	0.06
hourly resolution		440:403	**77**	**50**	7.5	**0.02**	0.65	**0.13**	**0.10**	**0.09**	**0.11**
daily mean			**83**	48	**4.0**	**0.08**	0.33	**0.13**	**0.10**	**0.07**	**0.11**

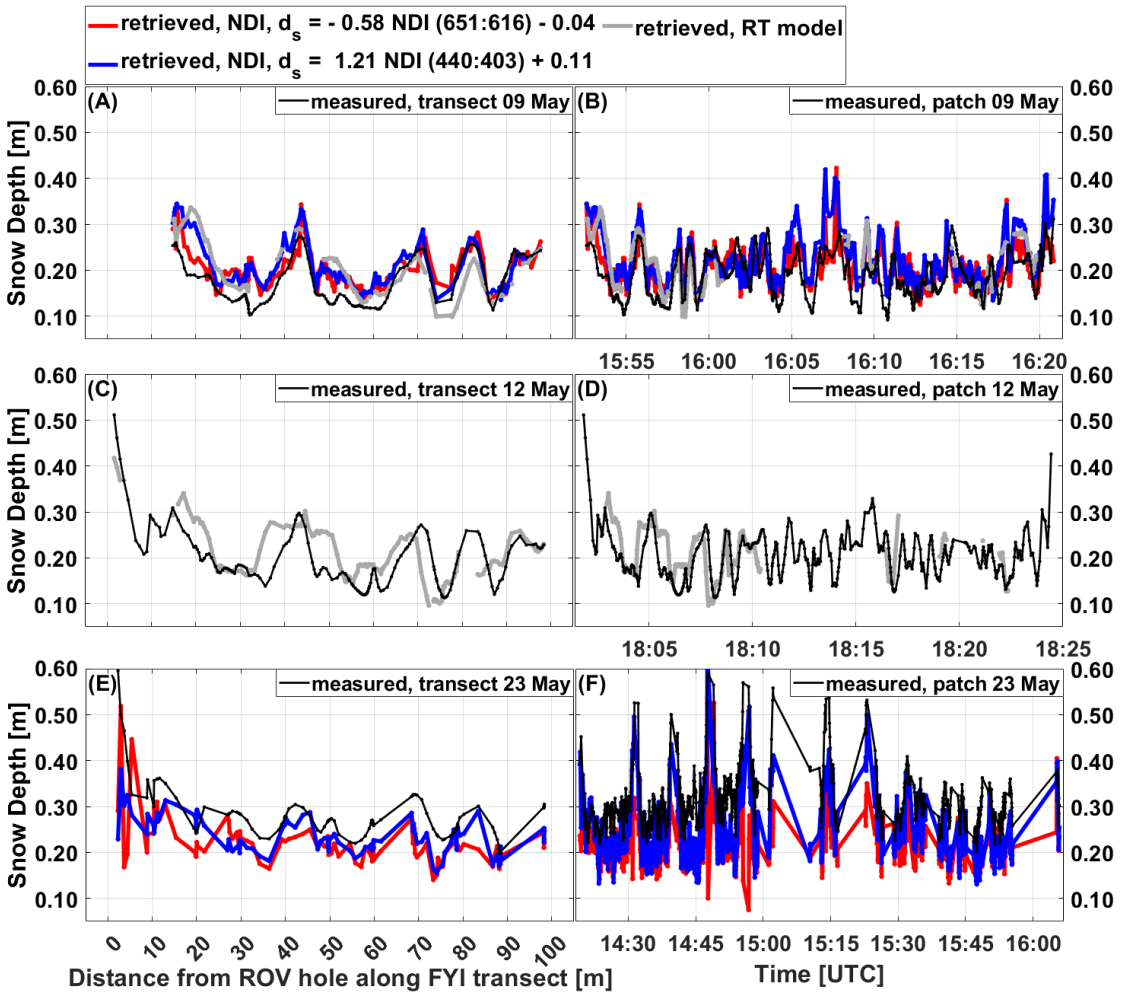

Figure 3.6: *Measured snow depth (black) and retrieved snow depth using the NDI method (red, blue) and the RT model (grey) along the transect (**A**, **C**, **E**) and across the patch (**B**, **D**, **F**). Note that for the patches the x-axis is time.*

and ice thickness. The resulting magnitudes and the spatial variability of the retrieved snow depth agreed well with the direct measurements (**Figure 3.6**, **Table 3.5**). The mean RMSE was 5 cm (**Table 3.5**). Agreements were between 64% and 72%. Δmodes ranged from 0 cm to 2 cm and were within the tolerance. Thus, the RT model performed better than the NDI method in reproducing the spatial variability of the measured snow depth.

3.4.4 Temporal variability of measured and retrieved snow depths

Here, we applied the NDI method and the RT model to continuous time series measurements of snow depth and transmittance as obtained by Snow Buoys and radiation stations during MAPLI18 (**Figure 3.7**) and AO18 (**Figure 3.8**).

Table 3.5: *Comparison of snow depth retrieval using the RT model and the snow and sea ice extinction coefficients from* ***Table 3.3****. In bold are the retrieved values within the tolerance of ± 5 cm. The modes were read from histograms with 1 cm bin width. N is the number of measurements used.*

Direct measurements	N	Agreement [%]		RMSE	Min	Max	Mean	Median	Std	Mode
				[cm]	[cm]	[cm]	[cm]	[cm]	[cm]	[cm]
		± 5 cm	± 50%							
Transect 09 May	110				0.11	0.27	0.17	0.15	0.05	0.13
		72	**88**	**5.0**	**0.10**	0.34	**0.19**	**0.17**	**0.06**	**0.15**
Transect 12 May	149				0.11	0.51	0.19	0.18	0.06	0.19
		64	**87**	5.2	**0.10**	0.42	**0.21**	**0.19**	**0.06**	**0.19**
Patch 09 May	209				0.11	0.30	0.18	0.18	0.04	0.20
		67	**90**	**4.9**	**0.10**	**0.34**	**0.20**	**0.20**	**0.05**	**0.21**
Patch 12 May	197				0.11	0.31	0.19	0.18	0.05	0.19
		68	**89**	**4.9**	**0.10**	**0.34**	**0.20**	**0.19**	**0.05**	**0.19**
2018S63										
05 – 21 May										
hourly resolution	379				0.23	0.32	0.28	0.28	0.02	0.29
daily mean	17				0.22	0.30	0.27	0.28	0.02	0.30
hourly resolution		16	**99**	6.8	0.11	0.25	0.21	0.22	**0.03**	**0.25**
daily mean		12	**100**	6.8	0.12	0.24	0.21	0.22	**0.04**	0.24
2018S69										
27 Aug – 18 Sep										
hourly resolution	515				0.02	0.11	0.06	0.05	0.02	0.05
daily mean	23				0.03	0.10	0.06	0.06	0.02	0.05
hourly resolution		**82**	**51**	**3.6**	**0.02**	0.18	**0.09**	**0.09**	**0.04**	**0.06**
daily mean		**78**	43	**4.5**	**0.04**	0.19	**0.09**	**0.10**	**0.05**	0.11
2018R4										
snow pinger										
27 Aug – 18 Sep										
hourly resolution	515				0.04	0.29	0.09	0.07	0.07	0.08
daily mean	23				0.05	0.26	0.10	0.07	0.07	0.07
hourly resolution		**70**	**68**	5.8	**0.02**	0.18	**0.09**	**0.09**	**0.04**	**0.06**
daily mean		**78**	**70**	**4.2**	**0.04**	0.19	**0.09**	**0.10**	**0.05**	**0.11**

Applying the NDI method with the wavelength pairs 651:616 nm and 440:403 nm to the MAPLI18 data set resulted in RMSEs of 4.6 cm and 2.3 cm, agreements of 59% and 96%, and Δmodes of 5 cm and 0 cm, respectively (**Figure 3.7A**, **B**, **Table 3.4**). The NDI method with 440:403 nm was clearly better in reproducing the magnitude but also the results with 651:616 nm were within the tolerance.

Using the RT model resulted in a RMSE of 6.8 cm, an agreement of 16%, and a Δmode of 4 cm. Although the RMSE was above the tolerance and the agreement low, the temporal variability was well reproduced (**Figure 3.7C**).

Between 9 and 10 May a wind-induced snow-redistribution event took place. This caused an increase in measured snow depth early on 9 May, which was captured by the NDI method and the RT model (**Figures 3.7B**, **C**). The subsequent decrease was however not reproduced using the NDI method with 651:616 nm. The decrease was measured at the same time as an increase in air temperature from about -10°C to -4°C (**Figure 3.7F**).

The time series of snow depth retrieved using the NDI method with 440:403 nm and the RT model shows a diurnal cycle on 7 May and between 9 and 12 May (**Figure 3.7B**, **C**). This is attributed to the daily variations in the transmitted irradiance and transmittance at the wavelengths 440 nm to 500 nm which are part of the blue spectrum (**Figure 3.7D**, **E**). Those variations occur because radiation at blue wavelengths is scattered about 16 times more efficiently by air molecules in the atmosphere than radiation at red wavelengths. During sunset and sunrise, the solar zenith angle is highest and radiation travels a greater distance through the atmosphere while the radiation at blue wavelengths is scattered away. Thus, a diurnal cycle in solar radiation at blue wavelengths exists, here clearly affecting the snow depth retrieval using those wavelengths. The diurnal cycle in transmitted irradiance was present in the entire time series whereas diurnal variations in transmittance and retrieved snow depth occurred only on the specific days.

The diurnal cycle was removed by calculating daily means (**Figure 3.7A**-**C**). In general, comparing daily means resulted in lower RMSEs using the NDI method, whereas using the RT model it remained the same (**Tables 3.4** and **3.5**). For the wavelengths in the red part of the spectrum as with 651:616 nm, the diurnal cycle was also present but less pronounced. Therefore, it was not present in the retrieved snow depth (**Figure 3.7A**).

During AO18, the snow depth measured by the Snow Buoy 2018S69 and the single pinger attached to the radiation station 2018R4 agreed until 14 September (**Figure 3.8**, e.g, panel **A**). Then, the single pinger recorded a sharp increase, which was not measured by the buoy.

For most of the time series, the snow depth retrieved using the NDI method with 651:616 nm was significantly higher than the snow depth measured by the buoy (mean) and by the single pinger (**Figure 3.8A**). The NDI method was also unable to capture the increase recorded by the pinger. Due to transmitted irradiance below 1 mW m^{-2} for the wavelengths in the red part

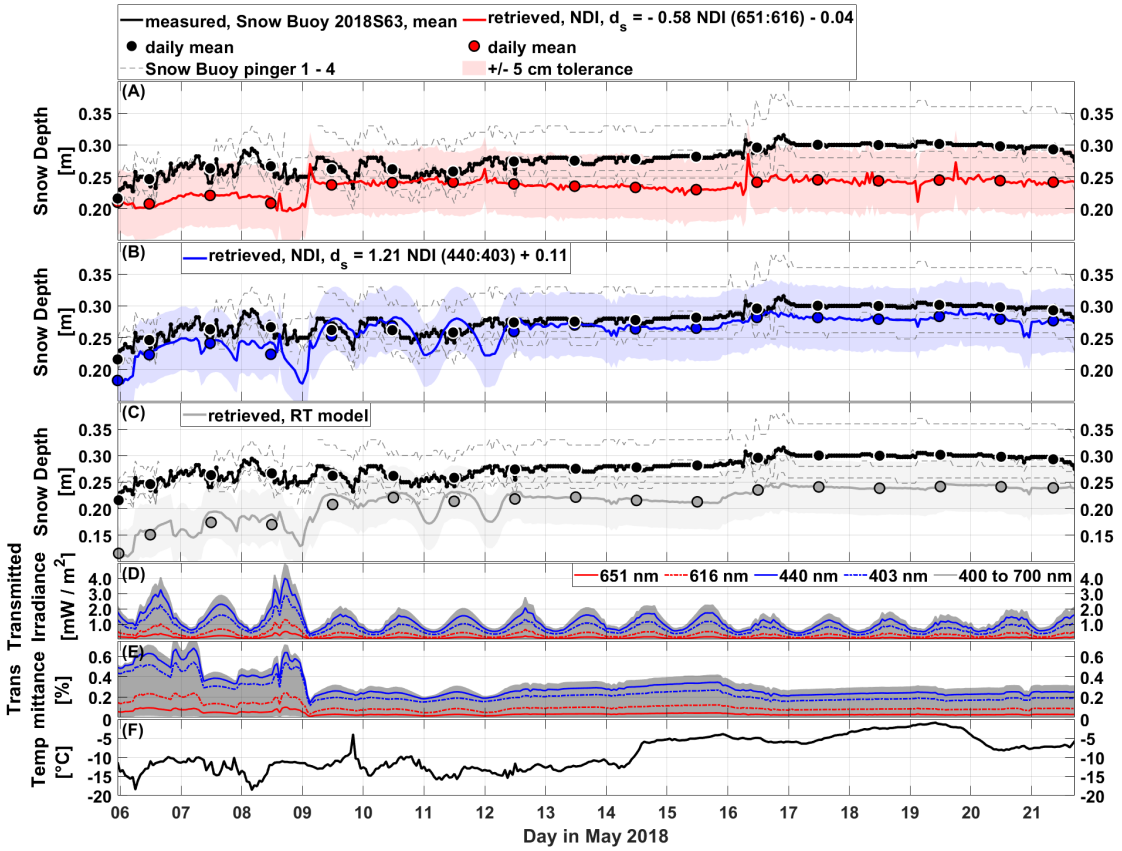

Figure 3.7: *(**A**)-(**C**) Hourly mean snow depths measured by the Snow Buoy 2018S63 as obtained on FYI during MAPLI18 (solid black). Variations in the snow depth of the four individual ultrasonic snow pingers are indicated by the respective grey dashed lines. The snow depths retrieved using the NDI method with the wavelength pairs 651:616 nm (**A**, red) and 440:403 nm (**B**, blue) are overlaid. The NDIs were calculated from the 2018R23 transmittance. (**C**) Retrieved snow depths using the RT model with the extinction coefficients from **Figure 3.8** (grey). Corresponding daily means (circles) are overlaid. The tolerance of ± 5 cm is indicated by the respective coloured shadings. (**D**) Transmitted irradiance in mW m^{-2} and (**E**) transmittance in % for the wavelengths of the NDI method and integrated from 400 nm to 700 nm as used in the RT model. (**F**) Air temperature in °C as measured by the Snow Buoy.*

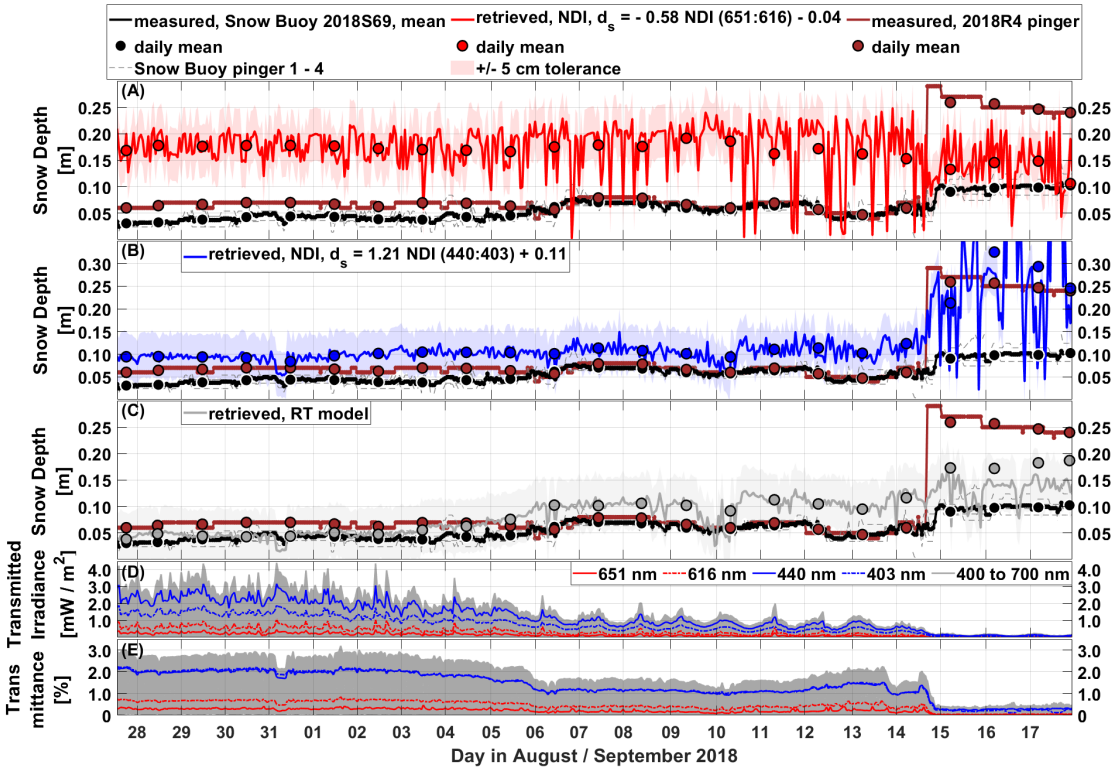

Figure 3.8: *(**A**)-(**C**) Hourly mean snow depths measured by the Snow Buoy 2018S69 (solid black) as obtained on MYI during AO18. Variations in the snow depth due to the four individual ultrasonic snow pingers are indicated by the respective grey dashed lines. The snow depth measured by the snow pinger attached to the radiation station 2018R4 is indicated by the solid brown line. The snow depths retrieved using the NDI method with the wavelength pair 651:616 nm (**A**, red) and 440:403 nm (**B**, blue) are overlaid. The NDIs were calculated from the 2018R4 transmittance. (**C**) Retrieved snow depths using the RT model with the extinction coefficients from **Figure** (grey). Corresponding daily means (circles) are overlaid. The tolerance of ± 5 cm is indicated by the colored shadings. (**D**) Transmitted irradiance in mW m^{-2} and (**E**) transmittance in % for the wavelengths of the NDI method and integrated from 400 nm to 700 nm as used in the RT model.*

of the spectrum the retrieved snow depth was noisy (**Figure 3.8A**). The irradiance decreased further from 14 September onwards with the increase in snow depth. Similar results were achieved by using the NDI method with other wavelength pairs in the yellow/orange/red part of the spectrum (not shown). Because of this, the results using 651:616 nm were excluded from further analyses related to the temporal variability during AO18.

In contrast, the using 440:403 nm reproduced the increase and the retrieved snow depth agreed better to the measurements (**Figure 3.8B**). However, the retrieved snow depth was also noisy at the same time as the transmitted irradiance for the algorithms blue wavelengths became low (**Figure 3.8D**). RMSEs between retrieved and both buoy and pinger snow depths were above the tolerance (**Table 3.4**). The comparison to the pinger snow depth was better than to the buoy. While comparing daily means for the buoy led to similar results, the RMSE of 4 cm was within the tolerance when comparing to the pinger daily means.

On average, the snow depths retrieved inversely with the RT model agreed better than the snow depths from the NDI method (**Figure 3.8C**, **Table 3.5**). The overall temporal variability was reproduced and the RMSEs were 3.6 m (buoy) and 5.8 cm (pinger). However, the sudden increase measured by the pinger was only partly captured and with a lower magnitude. Comparing daily means from the buoy led to worse results, while daily means from the pinger improved the RMSE.

To summarize, the magnitude of the mean snow depth measured by the Snow Buoy 2018S63 during MAPLI18 was well reproduced using the NDI method with both wavelength pairs and the RT model. However, the temporal variability using 440:403 nm in the NDI method and the RT model was influenced by the diurnal cycle in transmittance due the wavelengths in the blue part of the spectrum that were used to retrieve the snow depths. In contrast, the temporal variability during AO18 was well reproduced because no diurnal cycle was observed. The performance of the NDI method with the wavelengths in the red part of the spectrum, 651:616 nm, to this time series was limited due to the low transmitted irradiance. The overall performance of the NDI method and the RT model combined was with mean RMSEs of 5.6 cm and 5.3 cm, respectively, comparable.

3.5 Discussion

3.5.1 Accuracy of snow depth retrieval

The total mean accuracy (RMSE) along spatial measurements and for time series from both methods and the two locations is 5.6 cm and with that slightly above the tolerance. The accuracies achieved using the RT model are better than using the NDI method for spatial scales but comparable for temporal scales (**Tables 3.4** and **3.5**). The lateral resolution using

the NDI method is on average less than 1 m owing the high-resolution ROV and laser scanner measurements while using the RT model it is 10 m attributed to the spacing between the marker locations (**Figure 3.1B**).

In this study, the range in snow depth retrieval is dictated by the range in measured snow depth which is between 0.02 m and 0.60 m and, thus, covers a wide range (**Tables 3.4** and **3.5**). Extreme snow depths and variability can occur in troughs between ridges, at ridge flanks, in form of sastrugi, and on newly formed, thin ice (cracked features). The transflectance under ridges is most likely quite low and noisy due to the thick ice which is expected to make snow depth retrieval difficult. However, this remains speculative as this not investigated. On the same token, the difficulty in retrieving snow depth in form of sastrugi is explained by the extreme snow depth variability across 10^{th} of centimetres in horizontal scales. As described in **Section 3.3.3**, the footprint radius of the radiance radiometer on the surface is 1.5-2.0 m which hints to the impossibility to retrieve snow depth of sastrugi correctly. We have not attempt to retrieve snow depth on thin ice but expect that the methods presented in this study are applicable and promising. However, little is known about radiative transfer in thin ice which might complicate the retrieval.

Compared to no snow depth information or vague visual observations from a ship´s bridge as for example during biological sampling with large nets towed behind a ship (e.g., Castellani et al., 2020, the accuracy achieved here appears satisfying.

Our total mean accuracy of 5.6 cm compares with retrieved snow depths using satellite and airborne products. Rostosky et al. (2018) present a RMSE of 3.7 cm using passive microwave on FYI in spring. Guerreiro et al. (2016) and Lawrence et al. (2018) use dual-band altimetry and retrieve mean RMSEs of 6.4 cm and 3.0 cm to 5.0 cm, respectively. However, these satellite products do not provide the same spatial resolution as our approach. Jutila et al. (2021) obtained a RMSE of 6.9 cm using an airborne microwave radar on level landfast FYI.

Once technology advances, autonomous platforms such as AUVs and submarines equipped with radiometers might travel many kilometers under the ice and measure transmitted radiation. Our methods might provide an option to remotely retrieve snow depth for regional or basin-wide scales covered during such surveys. For many research questions, it would then be sufficient to estimate whether an ice floe has a thin, intermediate, or thick snow cover within the accuracy achieved in this work. During those surveys, a wider range in sea ice types, snow covers, and seasonal differences and progressions in snow depth as well as in under-ice radiation could be investigated. Such measurements could serve to further develop and validate our methods and then provide a base for more targeted Arctic surveys over different spatial and temporal scales.

During MAPLI18, the fast snow depth variations measured by the buoy are probably unrealistic. The snow pack does not change so quickly except during strong wind events (Lange et al.,

2019), which were not frequently observed. This might explain some discrepancies between then measured and the retrieved snow depths.

During AO18, we found a large discrepancy of 10.9 cm (daily mean 8.8 cm) between buoy measurements and the results from the NDI method with 440:403 nm. This can be explained by spatial variability in snow depth and the noise from 14 September onwards (**Figure 3.8B**, **D**). The buoy was deployed 10-15 m away from the under-ice irradiance radiometer which was closer to the pinger. In contrast, the RT model results agree better with the buoy than with the pinger snow depth because the RT model captures only partly the sharp increase measured by the pinger. Nonetheless, some discrepancies might also occur because we compare optical to geometrical snow depth.

3.5.2 NDI-specific comparison to existing studies

Our two wavelength pairs for the NDI method are similar to previous studies, reflecting their potential to retrieve snow depth. In the Antarctic, Melbourne-Thomas et al. (2015), Arndt et al. (2017), and Wongpan et al. (2018) found wavelength pairs in the orange/red and blue part of the spectrum. In the Arctic, Mundy et al. (2007) separated the influence of snow depth on the spectral magnitude and distribution. They found strongest correlation between their NDIs and snow depth at wavelengths less than 570 nm for the magnitude. However, they attribute snow depth little influence on the distribution between 400 nm and 550 nm. Nevertheless, our findings and the results from Wongpan et al. (2018) confirm that the snow depth influences the under-ice radiation also at wavelengths below 500 nm and supports the application of the NDI method with 440:403 nm. We find that wavelength pairs with spectral ranges larger than 30 nm perform better than those with lower ranges. For example, we tested another wavelength pair with a spectral range lower than 20 nm that significantly overestimated the snow depth (not shown). Further, Melbourne-Thomas et al. (2015) provide wavelength pairs with spectral ranges of 3 nm and 4 nm. Those are likely too narrow to resolve the spectral influence of snow depth, given that the spectral resolution of the radiometer is only 3.3 nm.

3.5.3 Model-specific comparison to existing studies

The two-layer RT model (**Equation 3.2**) is idealized and theoretically only valid in the absence of scattering and far away from boundaries (Mobley, 1994). Those simplified conditions are rarely met in sea ice (Light et al., 2004). However, this approximation is often used for modelling approaches within sea ice. It gives already useful information, as presented in this work, and is the easiest form of a RT model (Grenfell and Maykut, 1977). Further, Arndt et al. (2017) use this RT model in the Antarctic and find reliable estimates of spectral snow and sea-ice extinction coefficients. This strengthens our confidence that this simple model is a justified tool for our

application.

The values of our spectral snow extinction coefficients obtained during MAPLI18 agree with the lower ranges published by Warren (1982) and Perovich (2007). They are very close to values presented by McDonald et al. (2015) for landfast FYI near Resolute Passage, Canada, in spring. Their shape is in agreement with Grenfell and Maykut (1977) and McDonald et al. (2015). Our broadband coefficient matches with the values from Mundy et al. (2005) and McDonald et al. (2015) obtained also close to Resolute Passage during spring. The sea ice extinction coefficients seem too high compared to values stated by Grenfell and Maykut (1977), Perovich (1996), and Light et al. (2008). However, they compare well to results from Katlein et al. (2015) and Katlein et al. (2019). The overall agreement with literature values suggests that our snow and sea ice extinction coefficients are reliable estimates and justify their use to retrieve snow depth with the RT model.

During AO18, the spectral extinction coefficients and thus, the transmittance were likely influenced by a small melt pond in the vicinity ($\sim 2\,\mathrm{m}$) of where the radiometer was hanging underneath the bare ice (**Figure 3.1D**). This is supported by a footprint radius on the surface of the radiometer of about 3 m. Melt-pond covered MYI has clearly different optical properties than FYI. Assuming a scattering coefficient of the melt water of zero is likely justified as the ponds appear blue also after refreezing and thus, scattering can be neglected (Lu et al., 2018a). A typical broadband absorption coefficient of $0.1\,\mathrm{m}^{-1}$ and the average melt pond depth of 0.3 m as measured during AO18 lead to a relative error of 3.1% in transmittance that arises when neglecting the absorption within the melt ponds. This small error and the well retrieved snow depth using the RT model (**Figure 3.8C**, **Table 3.5**) led conclude that besides the different optical properties of melt-pond covered MYI compared to FYI, the MAPLI18 extinction coefficients are suitable to apply also to the AO18 data set.

3.5.4 General comparison to existing studies

The choice between radiance/transflectance and irradiance/transmittance likely affects the method calibration of snow depth retrieval. The opening angle of the radiometers influences the ability to resolve small spatial scales of snow depth and to capture outlier values. Transflectance is based on the much smaller opening angle of 7° of the radiance radiometer compared to the half sphere of the irradiance radiometer. Mundy et al. (2007), McDonald et al. (2015), Melbourne-Thomas et al. (2015), Arndt et al. (2017) and use transmitted irradiance. Wongpan et al. (2018) use transmitted radiance but do not account for atmospheric variations, which is more accounted for when using transflectance. For the spatial variability we use transflectance whereas for the temporal variability we use transmittance measurements from the buoys. This might be sufficient for the buoy measurements because we do not aim to resolve spatial scales

but reproduce the temporal variability.

The methods calibrated with measurements collected at the marker locations are expected to yield better results compared to using non-marker measurements. The reasons for that assumption are a shallower water column between radiometer and ice bottom and with that less absorption by water and a stable well-known ROV position. However, the NDI method is based on all measurements along the transect, so also the non-marker measurements. Thus, we conclude that our assumption of neglecting absorption by water and water biomass during MAPLI18 is justified.

The performance seems to also depend on the variability of the measured snow depth used to calibrate the methods. On 9 May, the range in measured snow depths was in the mean 21 cm lower than on 12 and 23 May (**Table 3.1**). The methods calibrated with snow depths measured on 9 May did not perform as good as the methods presented here (not shown). This suggests that if the range in snow depth is limited in the calibration stage of the methods, their ability to retrieve a larger variety of snow depths will be modest.

3.5.5 Application to sea-ice research including technological aspects

In general, it is easier to measure the snow depth directly, e.g., using a Magnaprobe, than measuring under-ice radiation. However, when measuring under-ice radiation using an under-water platform coincident measurements of snow depth are often not practical because they can also destruct the surface which will impact subsequent under-ice radiation measurements, especially when time series under the same ice area need to be collected. Thus, the advantage of developing the two methods presented in this study is to enable snow depth retrieval remotely from under-ice radiation yielding co-localized, non-destructive data of under-ice radiation and snow depth.

Little is known about the spatiotemporal distribution of snow depth on sea ice on regional scales (Sturm and Massom, 2017). Hence, a future aim is to retrieve high spatial coverage snow depth for large regions of Arctic sea ice which is in particular necessary to improve the description of snow processes in climate models (Webster et al., 2018) and the validation of satellite products. A product derived from this study could be probability density functions of snow depth that could serve as input for, e.g., Icepack, the column physics package of the Los Alamos sea ice model CICE (e.g., Zampieri et al., 2021). However, for that to be feasible the gaps between local scale studies as presented here and larger scales studied in models need to be minimized. One step could be to apply the methods to all available under-ice surveys where radiation was measured and retrieve snow depths for the different ice types, and spatial and temporal scales covered therein. For example, Katlein et al. (2019) provide radiation data for many ROV surveys in the Arctic between 2011 and 2017. This would also help to further

monitor and assess changes of under-ice radiation, snow depth, and their combined effects on the energy and mass balance of the sea ice in the focus of climate change. However, measuring snow depth *in-situ* for larger areas is neither practical nor appealing. This gap could be closed once extensive AUV surveys with a focus on measuring under-ice radiation from which snow depth can be retrieved can be conducted regularly. During an AUV survey presented by Wulff et al. (2016) measurements were collected along a short section of a few kilometers in a couple of hours at the marginal ice zone in Fram Strait. Possibilities for larger surveys will exist in the future, as technology in AUV operations advances.

In this study, we retrieve snow depth on two ice types, at two geographic locations, and during two seasons. FYI and melt-pond covered ice are predicted to prevail in the future Arctic (e.g., Maslanik et al., 2007; Perovich et al., 2009; Schröder et al., 2014). Therefore, information on the snow depth for those ice types is important to study the energy balance, especially prior to the melt season (MAPLI18) and before and during freezing (AO18).

Biological studies would benefit from using our methods by retrieving snow depth from the same data set used to estimate biogeochemical properties. With that, interpretation of data could be put in a broader context.

Chlorophyll *a* concentrations were successfully retrieved from ice core scanning using hyperspectral cameras (Cimoli et al., 2020). In this process, small sections of biomass containing ice cores are cut and illuminated with different light sources. Hyperspectral images of the through the ice section transmitted light result in light spectra from which, e.g., biomass absorption peaks can be investigated.

Such an optical set-up is in principal possible to perform on sections of snow-covered ice. However, it might be logistically challenging to retrieve an ice core with an undisturbed snow cover from the field. Instead, laboratory studies could be envisioned using in the freezer grown sea ice and artificial snow. Hyperspectral images could then be used to examine the spectral effect of snow on the transmitted light.

Another method used to retrieve chlorophyll a concentrations from under-ice radiation spectra is the principal component analysis (e.g., Lange et al., 2016; Cimoli et al., 2020). In this method, spectra are normalized to reduce the variability due to the magnitude and to focus on the spectral shape (Craig et al., 2012; Taylor et al., 2013). Several steps of statistical computations described by Lange et al. (2016) result in empirical orthogonal functions which modes characterize the variability in the spectra. Within linear functions, those modes act as predictor variables to retrieve chlorophyll *a*. In principle, this method could be used to retrieve snow depth. The NDI method could benefit from a multilinear regression (e.g., Lange et al., 2016) or machine learning approach to use instead of one wavelength pair, several. This is expected to yield better results but the simplicity of the NDI method as presented here has its advantages. Radiometers with two wavelengths compared to hyperspectral radiometers (e.g., TriOS) are

cheaper. For example, the Ocean Color Radiometer 504 or 507 manufactured by WET Labs, Inc. Thus, the application of the NDI method could also reduce costs and material for future deployments of autonomous stations.

3.5.6 Limitations

Atmospheric influence

Optical measurements should be collected under overcast conditions and at around noon. Clear sky conditions and changing cloud cover and solar elevation lead to variations in the blue part of the spectrum. This also affects the direction from which photons originate and the distance they travel within the snow and sea ice.

The diurnal cycle during MAPLI18 is caused by variations of incident irradiance in the blue part of the spectrum which is reflected in the transmitted irradiance (**Figure 3.7D**). As evident in the transmittance, the influence of atmospheric absorption is not completely compensated for by normalizing the transmitted irradiance with the incident irradiance (**Figure 3.7E**). For some atmospheric conditions some variability persists under the ice which seems to have been the case during 7 and 9 to 12 May. In contrast, during AO18 a diurnal cycle is not present in the transmittance and thus not in the retrieved snow depths (**Figure 3.8**). Most likely, this is due to smaller daily solar variations owing the higher latitude and the season. The diurnal cycle is also not present in the retrieved snow depths when using wavelengths in the red part of the spectrum as the snow attenuates the incident irradiance very efficiently at those wavelengths (**Figure 3.7**, Perovich, 2007). Here, the retrieval depends more on the magnitude of the transmitted irradiance.

During AO18, substantial noise in the snow depth retrieved using red wavelengths is attributed to irradiances below $1.0\,\mathrm{mW\,m^{-2}}$ and transmittance below 1% (**Figure 3.8**, Katlein et al., 2021a). From 14 September onwards noise is also evident in the snow depth retrieved using blue wavelengths (**Figure 3.8B**). This corresponds to transmitted irradiance and transmittance close to zero caused by the sharp increase in snow depth recorded by the pinger.

It seems that rapid and extensive variations in air temperature affect the measured snow depth from the ultrasonic pingers of Snow Buoy 2018S63 even though the measurements are temperature compensated (**Figure 3.7**, Nicolaus et al., 2021).

The limitations addressed here can be partly compensated for by using daily means of radiation to retrieve snow depth. For example, the period where the NDI method with the wavelength pairs 440:403 nm yields reasonable results can be prolonged but it is unclear for how long, e.g., towards winter (**Figure 3.8B**).

Influence of other constituents on the extinction of solar radiation

Besides snow depth and ice thickness, the magnitude and spectral shape of the radiation are also determined by snow grain size, wetness, and density, snow and ice temperature, snow metamorphism (e.g., Warren, 1982; Perovich, 1996; Perovich et al., 1998), particulates in snow (Warren, 1982) and ice (Light et al., 2008), water (e.g., Baker and Smith, 1982) and in-ice biomass (e.g., Mundy et al., 2007). Especially the biomass has large effects during spring bloom (Perovich et al., 1998). The optical properties of snow can also be locally altered through flooding which changes the physical and optical snow properties, leads subsequently to refrozen snow ice and additional biomass introduced on the snow/ice interface (Perovich, 1990; Arndt et al., 2017). During MAPLI18, we observed typical snow characteristics with metamorphic forms. Air temperatures were negative, thus, most likely no further melt processes were initiated (**Figure 3.7F**). Including information of the internal snow layers and their optical properties as well as scattering may improve the snow depth retrieval. However, we neglect the influences of the above mentioned effects and achieve satisfying accuracies for the snow depth retrieval by doing so. The calibration and results of the methods also benefit from clear water, low in-ice chlorophyll *a* (Lange et al., 2019), and level ice with constant thickness.

3.6 Conclusions

We apply two optical methods that successfully retrieve spatial and temporal variations in snow depth on different ice types, locations, and seasons with a combined mean RMSE of 5.6 cm. The spectral effect of snow on the transflectance can be separated from other components because the water was clear, in-ice biomass was low, and the ice was level and had a constant thickness. This makes it possible to establish relationships between transflectance and snow depth.
The spatial variability and magnitude in snow depth on landfast level FYI in the Lincoln Sea in spring 2018 (MAPLI18) can be reproduced 1) by NDIs with the wavelength pairs 651:616 nm and 440:403 nm and 2) by an idealized two-layer RT model with a nonlinear least square algorithm including inversely retrieved spectral snow and sea ice extinction coefficients.
Both methods are less reliable in retrieving the temporal variability of snow depth during MAPLI18 due to the influence of the diurnal cycle in solar radiation at wavelengths in the blue part of the spectrum. However, the magnitudes of the retrieved snow depths agree with the measured time series, especially when comparing daily means. In contrast, the temporal variability on drifting, melt-pond covered MYI in the Central Arctic during autumn 2018 (AO18) can be reproduced by the methods using blue wavelengths. This is because atmospheric variations in the blue part of the spectrum are less pronounced here, likely owing the higher latitude and the different season. The NDI method with wavelengths close to the near-infrared

produce noise in the retrieved snow depth because the extinction of radiation by snow at those wavelengths is strong. This can partly be compensated for when constraining to daily means. In no regard is this work meant to replace *in situ*, airborne, or satellite snow depth measurements and retrievals. The methods can rather provide a step forward to retrieve snow depth from under-ice hyperspectral measurements and serve as a close-range sensing tool that can increase spatial and temporal coverage of local measurements that can be applied across different regions. This can be particularly useful in providing auxiliary data for remotely operated and autonomous under-ice missions, where surface data are unavailable.

Data availability statement

All data presented in this study are publicly available under the following DOIs:
ROV: doi:10.1594/PANGAEA.930289.
Terrestrial laser scanner, Magnaprobe, EM31-SH: doi:10.1594/PANGAEA.932594.
2018S63: doi:10.1594/PANGAEA.905717.
2018R23: doi:10.1594/PANGAEA.936597 (dataset in review).
2018S69: doi:10.1594/PANGAEA.905723.
2018R4: doi:10.1594/PANGAEA.936930 (dataset in review).

Acknowledgments

We thank Polar Continental Shelf Program (PCSP), Natural Resources Canada; Department of National Defense (DND) at CFS Alert, and Defense Research and Development Canada (DRDC), Environment and Climate Change Canada (ECCC), and the communities and Hunters and Trappers Associations of Resolute Bay and Grise Fjord. Special thanks to A. Platt (ECCC), C. Brown, J. Milne, J. Higgins and M. Simms at DRDC for all their efforts in logistics, and Major C. Stiles (CO), R. Hansen (SWO) and R. Lutz (Alta SWO) at CFS Alert. We also thank the MAP—Last Ice Program led by Christine Michel, funded by Fisheries and Oceans Canada (DFO) Science. Deployment of 2018R4 and participation in the AO18 expedition of the Swedish icebreaker Oden was facilitated by the Swedish Polar Research Secretariat (SPRS). We want to thank in particular Mario Hoppmann and Matthieu Labaste for field assistance, as well as Anja Nicolaus for administrative support around the buoy deployment.

4. From bright windows to dark spots: Snow cover controls melt pond optical properties during refreezing

This chapter has been published as

Anhaus, P., Katlein, C., Nicolaus, M., Hoppmann, M., and Haas, C. (2021): From bright windows to dark spots: Snow cover controls melt pond optical properties during refreezing, *Geophysical Research Letters, 48*(23), doi:10.1029/2021GL095369.

Key points

- Refrozen melt ponds may collect a thicker snow cover compared to bare sea ice due to their recessed topography
- Such snow-covered melt ponds transmit less light compared to bare ice of similar type
- This scenario has not been documented before and should be accounted for in studies involving light in a refreezing Arctic Ocean

4.1 Abstract

Melt ponds have a strong impact on the Arctic surface energy balance and the ice-associated ecosystem because they transmit more solar radiation compared to bare ice. In the existing literature, melt ponds are considered as bright windows to the ocean, even during freeze-up in autumn. In the central Arctic during the summer-autumn transition in 2018, we encountered

a situation where more snow accumulated on refrozen melt ponds compared to the adjacent bare ice, leading to a reduction in light transmittance of the ponds even below that of bare ice. Supporting results from a RT model suggest that melt ponds with a snow cover > 0.04 m lead to lower light transmittance than adjacent bare ice. This scenario has not been described in the literature before, but has potentially strong implications for example on autumn ecosystem activity, oceanic heat budget and thermodynamic ice growth.

Plain language summary

Arctic sea ice is covered with snow during autumn, winter and spring. During summer, melt ponds evolve in response to surface melting. After snow fall starts again in autumn, these ponds can be filled with a lot of snow compared to bare ice because of their recessed surface. Indeed, during an expedition close to the North Pole in summer and autumn 2018, we measured a thick snow cover on ponds. This thick snow cover reduced the light availability underneath the ponds to levels below that underneath adjacent bare ice. This is a surprising finding, because it is different from the established theory of high light availability underneath melt ponds during both summer and autumn and how this is described in most computer models. It has consequences for our understanding of the ice-associated ecosystem (organisms that live in and under sea ice). It might also impact the mass and energy balance of central Arctic sea ice during summer-autumn transition when new sea ice starts forming.

4.2 Introduction

During autumn, winter, and spring, snow controls the optical properties and, thus, regulates the energy as well as the mass balance of sea ice because of its high reflectivity (Grenfell and Maykut, 1977) and insulation (e.g., Sturm et al., 1997). The snow cover of Arctic sea ice is highly variable in time and space (Webster et al., 2014, 2018). The rougher the sea ice topography the more snow accumulates (Massom et al., 1997; Sturm et al., 2002), for example, at the lee sides of pressure ridges (Webster et al., 2018), at windward sides of snow dunes (Dadic et al., 2013), and within the depression of melt ponds (Perovich et al., 2003). In turn, the distribution of snow, especially snow dunes, influences melt pond formation (Petrich et al., 2012b; Polashenski et al., 2012). Melt ponds also play a key role for the surface energy budget (Nicolaus et al., 2012) and the mass balance of sea ice (Flocco et al., 2015), as well as for the ice- and ocean-associated ecosystem (Arrigo, 2014). In general, in August-September, the melt pond coverage peaks (Perovich et al., 2002b) and open and mature ponds evolve toward refrozen and snow-covered ponds (Perovich et al., 2009). The areal fraction of melt ponds on Arctic FYI is up to 53% and 20%–38% on MYI (e.g., Fetterer and Untersteiner, 1998; Nicolaus et al., 2012; Perovich et al.,

2003; Webster et al., 2015). This fraction has been shown to increase from 15% to 35% for MYI based on observations from 1994 to 2005 (Perovich et al., 2009) and from 11% to 34% for the entire Arctic based on model simulations from 1996 to 2012 (Schröder et al., 2014). The amount of radiation that is reflected back to the atmosphere is significantly reduced for melt ponds compared to bare ice (e.g., Nicolaus et al., 2012). Instead, a considerable amount of radiation is absorbed by and transmitted through melt ponds (e.g., Ehn et al., 2011; Katlein et al., 2015; Light et al., 2008, 2015; Nicolaus et al., 2012). Consequently, the ice underlying the melt ponds warms and can thin faster than bare ice during summer when no snow is present (Flocco et al., 2015; Hanson, 1965; Untersteiner, 1961).

The translucent melt ponds are often considered as bright windows in Arctic sea ice, even during autumn when their surface refreezes. The formation and occurrence of under-ice phytoplankton blooms are highly dependent on the under-ice light field and, thus, on snow and sea ice conditions (Ardyna et al., 2020). An Arctic-wide increase in the occurrence of the blooms was partly explained by the increasing fraction of melt ponds (Horvat et al., 2017). Lee et al. (2011) showed that ice algal masses accumulate in and under refrozen and snow-free melt ponds that favor higher light availability. They argue that algal accumulations in autumn can provide an important food source for higher trophic animals before and during winter.

This study documents a situation where a thicker snow cover accumulates on melt ponds compared to bare ice after snow fall starts in autumn. The thicker snow cover reduces the light availability under melt ponds to levels lower than under adjacent bare ice. Using data collected in the central Arctic close to the geographic North Pole during the transition from summer to autumn in 2018, we investigate the effect of snow accumulated on the refrozen melt ponds on the under-ice light availability. We compare two datasets that represent the summer and autumn conditions, which mainly consist of snow depth and ice thickness measurements, along with aerial images and under-ice transmittance data from an ROV. We apply a radiative transfer model to calculate an estimate for the snow accumulation threshold necessary for the light level to be lower under melt ponds compared to bare ice.

4.3 Material and methods

4.3.1 Study site

The data presented in this study were collected during the Arctic Ocean 2018 MOCCHA–ACAS–ICE campaign (short: AO18) onboard the Swedish icebreaker *Oden*. During this campaign, a temporary ice camp was set up on drifting, ponded MYI close to the geographic North Pole between 14 August and 14 September 2018. Snow depth, total sea ice thickness (ice thickness plus snow depth), and transmitted irradiance were measured in an area of approximately 100 m

× 100 m (**Figure 4.1**). Marker poles (M0 to M23) were deployed under the ice to facilitate ROV navigation and to obtain a better co-location of the data. The mean ice thickness of bare ice was 1.9 m and of the ice underlying the melt ponds 1.7 m (**Table 4.1**). Melt ponds were on average 0.3 m deep. Here we focus on two main datasets: measurements performed between 17 and 24 August represented summer conditions which were characterized by open or only slightly refrozen melt ponds and no snow cover, whereas measurements performed between 13 and 14 September represented autumn conditions which were characterized by refrozen and snow-covered melt ponds.

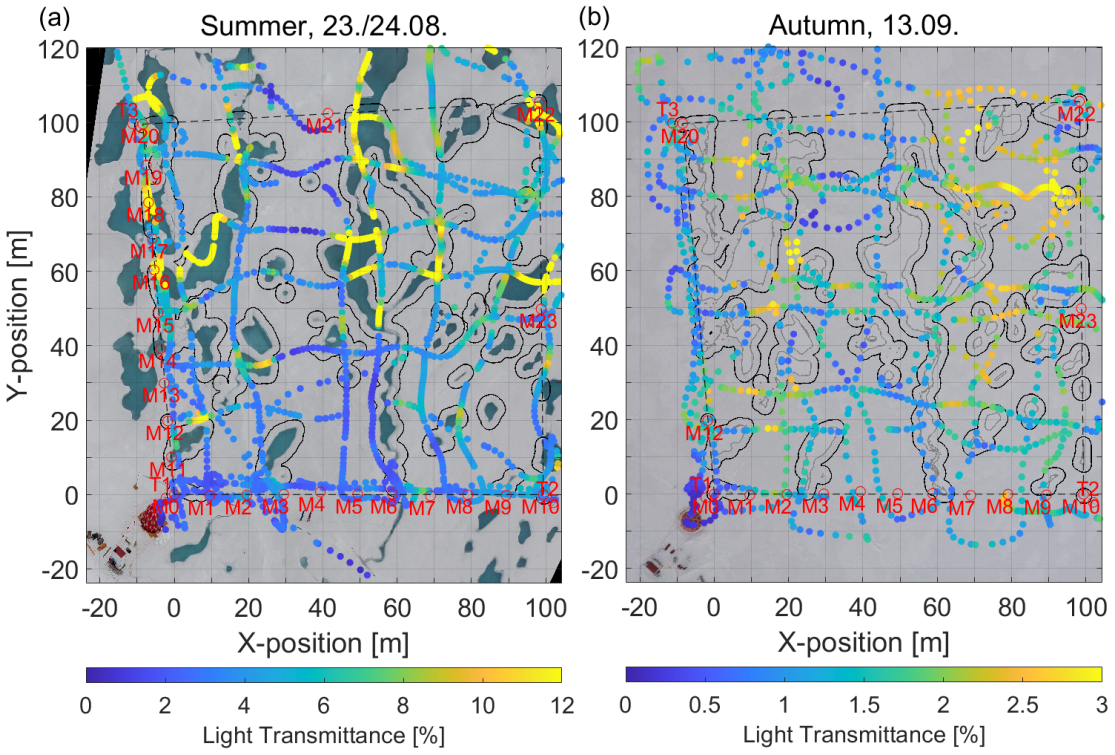

Figure 4.1: *Distribution of melt ponds and bare ice on drifting MYI in the central Arctic during the transition from (**a**) summer to (**b**) autumn. The surfaces of the melt ponds were partly open and partly refrozen in (**a**) and completely refrozen and snow-covered in (**b**). Overlaid is light transmittance as measured using an ROV. The background images are orthorectified aerial images acquired during (**a**) a low altitude helicopter flight and (**b**) a drone flight. Pixels within the study area that were classified as melt ponds and used for further analysis are outlined by the melt ponds themselves in (**a**) and by the gray line in (**b**). The edges around the melt ponds in (**a**) and (**b**) were dilated by a buffer of about 2 m indicated by the black lines. Red labels indicate the marker (M) and transponder locations (T). The ROV tent and control hut are visible on the lower left corners of the images. Note the different ranges in transmittance in (**a**) and (**b**).*

Table 4.1: *Statistics of measured snow depth (m), ice thickness (m), and light transmittance (%), of melt ponds and bare ice. N is the number of measurements. The modes were read from histograms (**Figure 4.3**) with bin widths of 0.01 m, 0.10 m, and 0.5%, respectively.*

Variable	Date	Type	N	Min	Max	Mean	Std	Median	Mode
Snow depth [m]	Autumn	Bare	1 308	0.04	0.25	0.11	0.03	0.10	0.09
	14.09.	Pond	887	0.05	0.32	0.14	0.05	0.13	0.10
Ice thickness [m]	Autumn	Bare	26 831	1.25	2.83	1.90	0.21	1.92	2.00
	14.09.	Pond	18 794	1.14	2.32	1.73	0.19	1.75	1.80
Transmittance [%]	Summer	Bare	830	0.7	15.5	4.1	1.9	3.9	4.5
	24.08.	Pond	859	1.6	23.2	8.9	5.5	7.1	5.5
	Autumn	Bare	466	0.2	3.4	1.8	0.7	1.9	2.0
	13.09.	Pond	328	0.4	3.1	1.3	0.6	1.2	1.0

4.3.2 Snow depth and sea-ice thickness

Snow depth point measurements with a horizontal spacing of 1–3 m and an accuracy of 0.01 m were obtained on the (pristine) study area using a Magnaprobe (Snow-Hydro, Fairbanks, AK, USA, Sturm and Holmgren, 2018). On snow-covered bare ice, the Magnaprobe likely penetrated into the underlying surface scattering layer (SSL) leading to an overestimate in snow depth. The GPS position of each measurement was recorded by an integrated GPS with an accuracy of 2.5 m (Sturm and Holmgren, 2018).

Total (sea ice plus snow) thickness was determined using a ground-based electromagnetic induction sounding device (GEM-2, Geophex Ltd, Raleigh, NC, USA, Hunkeler, 2016, Hunkeler et al., 2016) using the in-phase signal at a frequency of 18.33 kHz. The GEM-2 was placed on a sled and dragged across the study area in a grid pattern at the very end of the campaign. The accuracy of the total thickness measurements is ± 0.1 m (Hunkeler, 2016; Hunkeler et al., 2016). Finally, ice thickness was calculated from total thickness by subtracting the (interpolated) snow depths. GPS positions of snow depth and ice thickness measurements were subsequently corrected for ice drift using GPS recorders placed at the acoustic transponder locations to enable co-location with the transmittance measurements.

In addition, *in-situ* snow depth, ice thickness, draft, freeboard, and melt pond depth were measured in drill holes at the marker locations using a tape measure on 17 August.

4.3.3 Under-ice transmittance

Horizontal transects of under-ice spectral irradiance were measured by a RAMSES-ACC hyperspectral radiometer (TriOS GmbH, Rastede, Germany). The radiometer was mounted on a M500 ROV (Ocean Modules, Åtvidaberg, Sweden, Katlein et al., 2017). The ROV was lowered into the

water through a 2 m × 2 m hole in the ice covered by a tent next to the study area (**Figure 4.1**). The light transmittance was calculated by wavelength-integrating the transmitted irradiance from 350 nm to 920 nm and normalizing by the incident downwelling planar irradiance recorded by an upward-looking reference sensor at the surface. The data were filtered for ROV pitch, roll, and depth, and the noise was filtered from the spectra. Using the photosynthetically active radiation (400–700 nm) did not lead to qualitatively different results and conclusions in this work, and is thus not further considered here.
For under-ice navigation, the ROV was equipped with an acoustic long baseline positioning system (Pinpoint 1500 Linkquest, San Diego, CA, USA). We manually post-processed the ROV position to remove distortions caused by calibration uncertainties.

4.3.4 Aerial images

Oblique aerial images were obtained during a helicopter flight on 23 August (summer) and by a drone on 13 September (autumn). Those were used to retrieve the geographic coordinates of the melt ponds. The images were corrected for camera perspective and georeferenced using the marker locations measured by a terrestrial laser scanner (VZ-400i, RIEGL, Horn, Austria). Melt ponds in the image were detected using a simple threshold criterion. All pixels within the study area where $mean(R, G, B) < 70 + 0.5 \cdot B$ (Katlein et al., 2015) were classified as melt ponds, with R, G, B representing the integer values of the respective channels of the RGB color space ($R = 700\,nm$, $G = 525\,nm$, $B = 450\,nm$). We added a 2 m buffer by image dilation to account for horizontal light spreading (Ehn et al., 2011) and uncertainties of the ROV position.

4.3.5 Radiative transfer model

We modeled broadband reflection and under-ice transmittance using the radiative transfer model DORT2002 version 3.0 (Edström, 2005; Katlein et al., 2021a). The model uses a discrete ordinate model geometry and is implemented in the MATLAB^{TM} software. The ice geometry was approximated by three layers each for bare ice and melt ponds (**Table 4.2**): The bare ice consisted of the interior sea ice underlying an SSL with a freshly fallen snow layer of varying thickness on top. The melt ponds consisted of interior sea ice underlying the melt pond overlain by a snow layer of varying thickness. For simplicity, the situation without any snow will be referred to as "summer" conditions whereas the snow-covered scenario is referred to as "autumn" conditions. We used typical inherent optical properties for MYI (Katlein et al., 2021a; Perron et al., 2021).

Table 4.2: *Parameters used in the radiative transfer model. SSL is the surface scattering layer. The melt pond depth is based on the in situ average melt pond depth measured at six marker locations. The scattering coefficient for cold dry snow was provided by Perovich (1990). The other parameters were chosen with respect to Ehn et al. (2008); Light et al. (2008); Petrich et al. (2012a); Katlein et al. (2021a) and adjusted so that they resulted in transmittance values similar to our observations. A Henyey–Greenstein phase function with an asymmetry parameter $g = 0.9$ was used for all layers.*

Type	Layer thickness [m]		Scattering Coefficient [m^{-1}]	Absorption Coefficient [m^{-1}]	Refractive index
	Bare	Pond			
Snow	0-0.2	0-0.2	800	0.15	1.33
SSL	0.1	-	250	0.15	1.33
Interior ice	2.0	1.8	25	0.15	1.33
Pond	-	0.3	0	0.10	1.30

4.4 Results and discussion

4.4.1 Evolution of the snow cover in the transition from summer to autumn

Figure 4.1 illustrates the distribution of melt ponds and bare ice and their surface properties during the transition from summer to autumn in the study area.
On 23 August, the melt ponds were generally still open but in parts slightly refrozen at the surface (**Figures 4.1a** and **4.2**). No significant snow fall occurred prior to 29 August (Vüllers et al., 2021), however, an SSL of deteriorated ice with a mean thickness of 0.07 m was present. The passage of low-pressure systems between 29 August and 15 September brought precipitation accompanied by strong winds with speeds up to 13 $m\,s^{-1}$ (Vüllers et al., 2021). This wind speed exceeded the threshold of 8–10 $m\,s^{-1}$ under which divergence of large amounts of drifting snow is favorable (Van den Broeke and Bintanja, 1995). As a result, snow was deposited and re-distributed toward and caught by the recessed and refrozen melt ponds and their edges (Figure **4.2**, Fetterer and Untersteiner, 1998, Perovich et al., 2003). This led to a higher mean snow accumulation on the ponds (0.14 m) compared to on bare ice (0.11 m) as measured on 13 September (**Figure 4.3a**, **Table 4.1**). On the melt ponds, higher snow depths were also much more frequently measured than on bare ice (modes of 0.17 m and 0.22 m, **Figure 4.3a**).

The snow mostly covered the visible surface signature of the ponds (**Figure 4.1**). However, the ponds were still discernible because of their brighter appearance due to the higher snow depth compared to the adjacent bare ice (**Figure 4.1b**).
The higher snow depth on the melt ponds can have important implications on the sea ice mass balance related to the insulating effect of the snow cover (Sturm et al., 1997). Reduced heat loss (Maykut, 1978) and thermodynamic ice growth (Maykut, 1978; Merkouriadi et al., 2017) as well

Figure 4.2: *Photograph as of 23 August illustrating that refrozen melt ponds have a recessed topographic position within the adjacent bare ice (photo: Mario Hoppmann, AWI).*

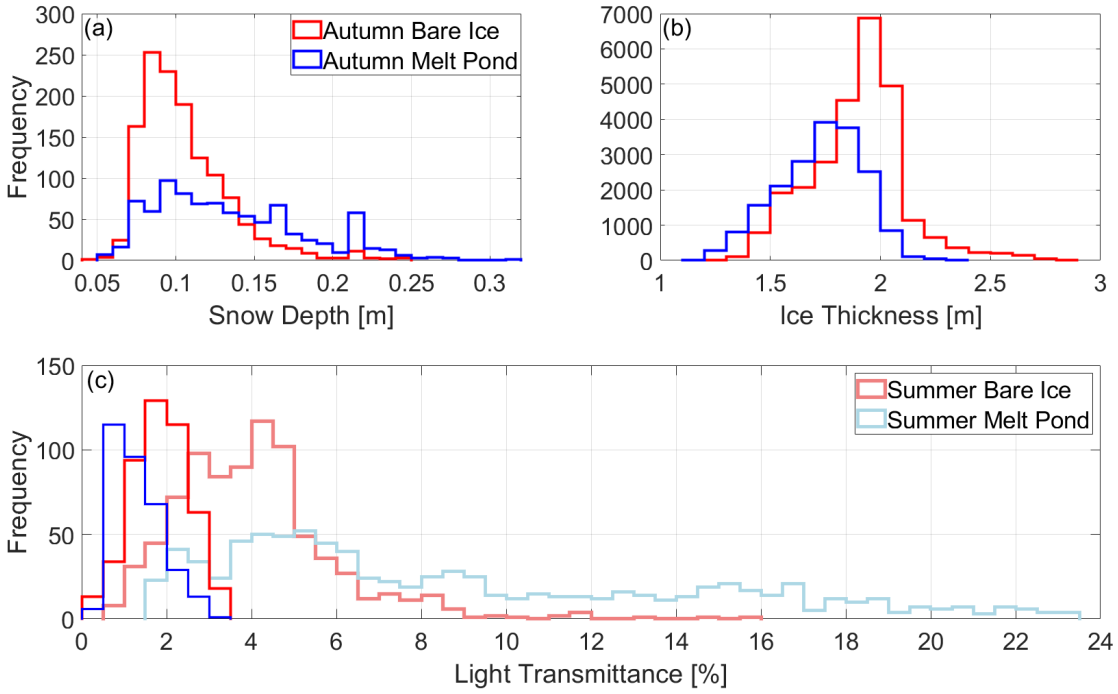

Figure 4.3: *Histograms of measured (**a**) snow depth, (**b**) ice thickness, and (**c**) light transmittance of melt ponds and bare ice.*

as delayed freeze-up of the liquid melt pond (Flocco et al., 2015) and induced bottom roughness are expected.

The refrozen surface of the melt ponds alone reduces the heat release from the ocean through the ice toward the atmosphere (Flocco et al., 2015). This hampers ice growth at both water-ice

interfaces of the refreezing pond, as well as between the sea ice bottom and the ocean in the transition from autumn to winter. This can result in a delay of the complete freeze-up of the pond by up to 60 days (Flocco et al., 2015). A thinner ice cover is more vulnerable to dynamic and warming events. The presence of a snow cover on top of the refrozen pond surface and the still liquid melt pond underneath are expected to amplify those effects (Perovich et al., 2003). As a result of the reduced thermodynamic growth of the sea ice underlying melt ponds compared to bare ice, a generally rougher bottom topography might result, affecting the mass, momentum, heat, and salt fluxes at the sea ice-ocean interface.

The exact evolution of the thicker snow cover on melt ponds during refreezing depends on the sequence of weather events. Whether or not more snow accumulates on the refrozen melt ponds than on adjacent bare ice is governed by the wind speed and snow drift regime during and after the snow fall, by the snow properties, and by the roughness of the refrozen surface. Falling and deposited snow needs to be re-distributed before it can accumulate on the topographically recessed and rougher pond surface. Wet and heavy snow is more resistant to erosion by wind than low-density dry snow (e.g., Colbeck, 1979; Massom et al., 1997). For instance, new snow deposited on blue ice either by drifting or precipitation can hardly settle on the smooth and warm surface (Bintanja, 1999; Van den Broeke and Bintanja, 1995). In case downwind slopes are smooth, any snow that can temporarily accumulate is prevented from actually attaching to the surface (Bintanja, 1999; Dadic et al., 2013). On such surfaces, drifting snow is also prevented from becoming attached causing the wind to be stronger over the glazed surface than over the snow (Frezzotti et al., 2002a). Furthermore, less snow will accumulate on smooth nilas with a low surface roughness (e.g., Massom et al., 1997; Sturm et al., 2002) than on surfaces with a higher surface roughness (e.g., Bintanja, 1999; Frezzotti et al., 2002b).

4.4.2 Optical properties

The surface topography of the ponded ice cover was key in modulating spatial variability in snow depth. The presence of open melt ponds in summer and the variability in snow depth driven by the refrozen melt ponds in autumn led to spatial and temporal variability in the under-ice light field. On 24 August, ROV-based mean and maximum transmittances of ponds (8.9% and 23.2%, respectively) were significantly higher than those of bare ice (4.1% and 15.5%, see also **Figures 4.1a** and **4.3c** and **Table 4.1**). Histograms showed a bi-modal transmittance distribution of ponds and bare ice combined (**Figure 4.4**). The distribution also showed a characteristic long tail for ponds, indicating high spatial variability and different properties of the ponds. This distribution is typical for Arctic summer sea ice and results from the formation and development of the melt ponds (Katlein et al., 2015, 2019; Nicolaus et al., 2012; Schanke et al., 2021). The magnitudes of transmittance are similar to observations from (Nicolaus et al.,

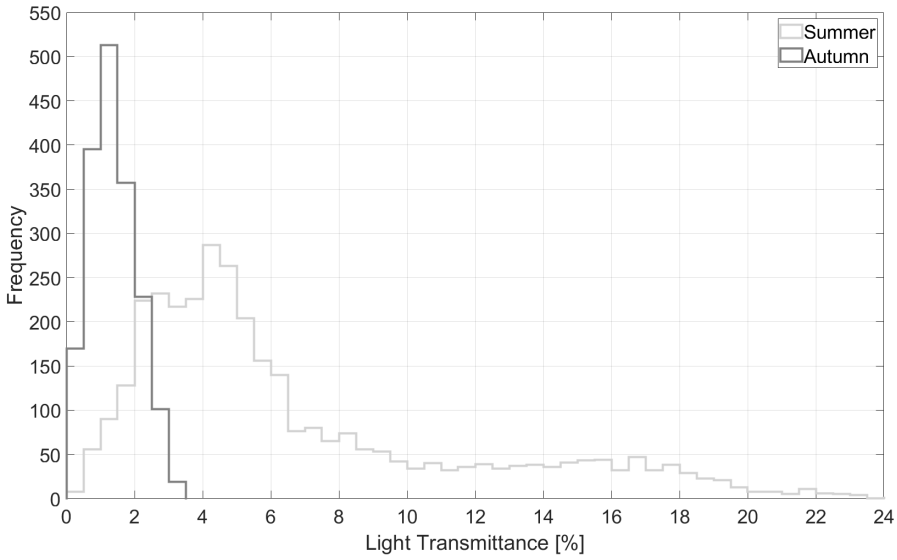

Figure 4.4: *Histograms of light transmittance as measured on 24 August (summer) and 13 September (autumn) of melt ponds and bare ice combined.*

2012) in the same region in August 2011. The maximum transmittance of the melt ponds also agrees to values found by (Katlein et al., 2019).

Due to the new snow cover on top of both the refrozen melt ponds and the bare ice (**Figure 4.1b**), the transmittance of both melt ponds and bare ice decreased (**Figures 4.1** and **4.4**, **Table 4.1**). The spatial variability in the transmittance of both melt ponds and bare ice was significantly reduced in autumn while the long tail of the high transmittances diminished, with very few observations higher than 3% (**Figures 4.3c** and **4.4**, **Table 4.1**). In summer, approximately 80% (25%) of the transmittance measurements were higher than 3% (9%). Due to stronger and more frequent snow fall events that started to occur from 28 August (Vüllers et al., 2021), only 1% (0%) of the transmittance measurements in autumn were higher than 3% (9%).

Lee et al. (2011) describe observations indicating that melt ponds remain bright windows even in autumn after refreezing, although they did not consider a snow cover. This implies that the transmittance of melt ponds remains higher than that of bare ice. (Katlein et al., 2019) showed that the bi-modal structure of transmittance during summer is conserved even during the first weeks of freeze-up in mid of September. They further suggest that the transmittances of both melt ponds and bare ice decrease gradually and equally in the transition from summer to autumn. Snow and particularly re-distribution were observed during their transmittance measurements, however, the influences of the re-distribution on the transmittance were not investigated.

We observed a different scenario than Lee et al. (2011) and Katlein et al. (2019). A thicker snow cover accumulated on melt ponds compared to adjacent bare ice because of the recessed topography of the ponds. This led to a lower mean transmittance of melt ponds (1.3%) than of bare

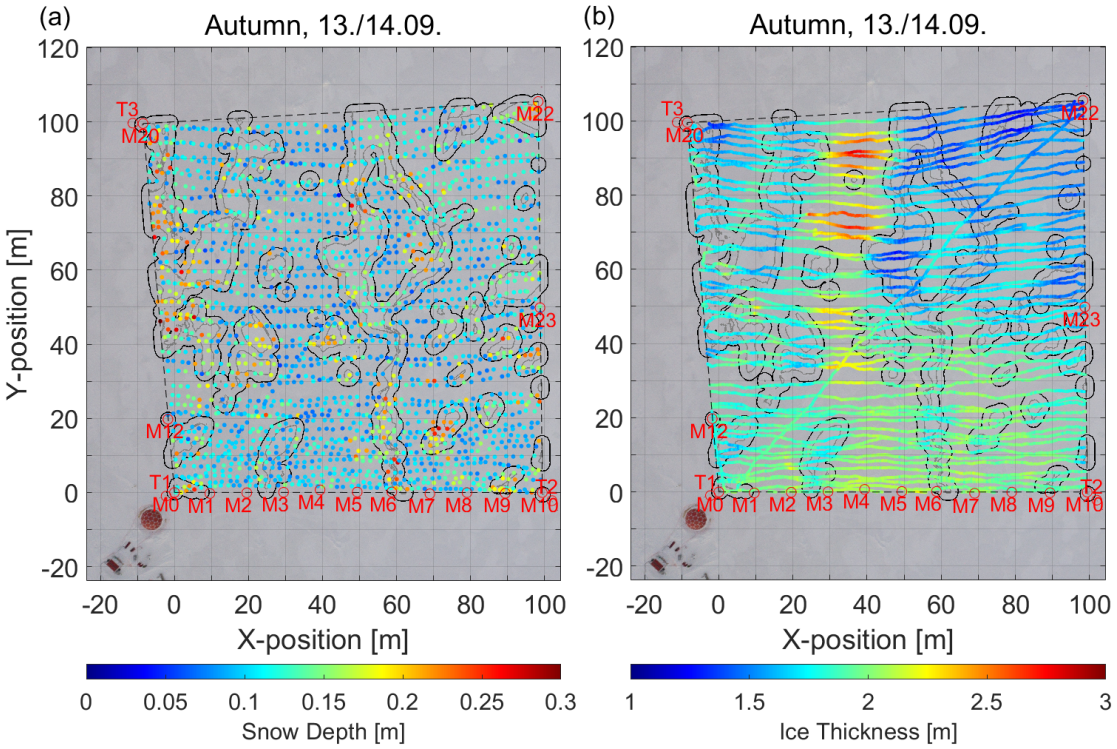

Figure 4.5: *(**a**) Snow depth and (**b**) ice thickness on ponded sea ice as measured on 14 September (autumn). The background images are orthorectified aerial images acquired during a drone flight on 13 September. Pixels within the area of focus that were classified as melt pond during the summer are outlined by the grey lines to illustrate the refrozen and snow-covered ponds during autumn. The edges around the melt ponds were dilated by a buffer of about 2 m indicated by the black lines. Red labels indicate the marker (M) and transponder locations (T). The ROV tent and control hut are visible on the lower left corners of the images.*

ice (1.8%) in autumn (**Figures 4.1** and **4.3c**, **Table 4.1**). The transmittance distribution showed two distinct modes of 1.0% and 2.0% associated with melt ponds and bare ice, respectively (**Figures 4.3c** and **Table 4.1**).

Despite the reversal of the magnitude in the transmittance of melt ponds and bare ice, the spatial variability remained during autumn (**Figure 4.1**). This suggests that the spatial variability was still coupled to the ponds after snow accumulation and re-distribution and most likely also persisted into winter.

The transmittance of ridged ice with thicknesses up to 2.8 m was naturally still lower than that of the melt ponds (**Figures 4.1b** and **4.5b**). Those measurements are included in the bare ice data and are represented in the tail of larger ice thicknesses in the histogram (**Figure 4.3b**).

This study provides quantitative observations of a thicker snow cover on melt ponds than on adjacent bare ice in autumn. Besides lower light transmittance of melt ponds than of bare ice due to higher snow depths on the ponds, major implications on the ice-associated ecosystem and the energy balance of the sea ice might arise from those observations in case such a situation

is viable for the entire Arctic which is very likely.

Lee et al. (2011) proposed that the soft refrozen surface of open melt ponds that are in connection with the ocean provides a fertile habitat for biomass in autumn. They pointed out that the biomass accumulated under the refrozen melt ponds serves as an important food source for higher trophic animals during the transition from autumn to winter and further into winter. However, as presented here, a snow cover significantly reduces the light availability in and under melt ponds in autumn, suggesting limited suitability as a habitat in terms of available light. These observations lend support to a study by Lange et al. (2017), who found higher biomass values underneath hummocks on MYI compared to adjacent level ice. Lange et al. (2017) attributed the differences in biomass accumulation to increased light availability under the hummocks resulting from a very thin or absent snow cover (Perovich et al., 2003). Our results and those of Lange et al. (2017) suggest that light conditions under sea ice in spring can already be initialized by melt pond coverage and snow distribution during autumn and may persist throughout winter.

Further, due to the common assumption that there is more light available under melt ponds than under bare ice also during autumn, processes and magnitudes of carbon uptake and biomass accumulation in models, might need to be adjusted with respect to our new observations.

Arndt and Nicolaus (2014) developed a parameterization to quantify the annual solar heat input through Arctic sea ice. For their calculations in autumn, they use for transmittances of melt ponds the fivefold (500%) of that of bare ice. However, our results showed that the modal transmittance of melt ponds is only half (50%) of that of bare ice once covered by the first snow (**Table 4.1**). Arndt and Nicolaus (2014) applied a constant summer mean melt pond fraction for MYI of 29% (Rösel et al., 2012) and transmittance of melt ponds for MYI of 0.4%. They estimated the solar heat input into the ocean in September to $0.69 \cdot 10^{19}$ J. We adopted their parameters but used the ratio of transmittances between melt ponds and bare ice as presented in the present study. As a result, the solar heat input into the ocean decreased by 61%. This shows, that despite the generally low solar energy fluxes in autumn compared to in summer (e.g., Arndt and Nicolaus, 2014; Perovich et al., 2011a), our described effect could have an important impact on the energy budget if valid in the entire Arctic. In this regard, our results might also impact the heat stored in the upper ocean, the interior sea ice structure, as well as internal and basal melting.

4.4.3 Radiative transfer model

For the effect described above, it is of interest to quantify the threshold snow depth that is necessary to decrease the transmittance of melt ponds below that of bare ice for the specific environmental conditions we have observed (**Table 4.2**). To determine this threshold depth,

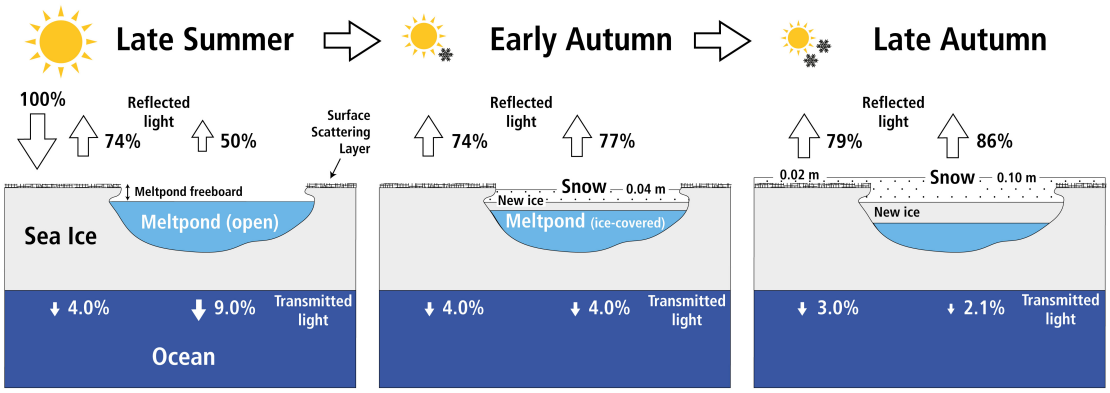

Figure 4.6: *A bright window turns into a dark spot: graphical representation of the situation observed in this study. During the transition from summer to autumn, snow predominantly accumulated on the recessed surface of frozen melt ponds, resulting in a reversal of the light transmittance between melt ponds and bare ice. Numbers result from the RT model DORT2002. Properties used in the model are displayed in* ***Table 4.2****.*

we used the RT model DORT2002. **Figure 4.6** summarizes the observations of this study is a schematic which is supported by simulated albedo and transmittance. For the situation without snow (summer), both the simulated transmittances of melt ponds and bare ice (9% and 4%, respectively) were very similar to our observations (8.9% and 4.1%, respectively, **Figures 4.6** and **4.7**, **Table 4.1**).

Incorporating an increasing snow cover from 0 to 0.20 m (autumn), our results yielded an exponential decrease in the transmittances of both melt ponds and bare ice (**Figure 4.7**). For a snow depth of approximately 0.04 m, the transmittance of the melt ponds becomes equal to that of snow-free bare ice for this specific situation (**Figures 4.6** and **4.7**). This is in agreement with the observations which showed that the transmittance of melt ponds was lower than that of bare ice for a 0.03 m higher mean snow depth on the ponds (**Table 4.1**). **Figure 4.6** illustrates that the transmittance of melt ponds with a 0.10 m thick snow cover is significantly lower than that of bare ice with a 0.02 m thick snow cover. In our simulations, the influence of the thin ice lid on the melt ponds on the transmittance was neglected, as they were only partially existing, as for typical Arctic summer sea ice these are very translucent and scattering is small (Lu et al., 2018b), indicated by their blue-green color (**Figure 4.1a**).

4.5 Summary

Snow depth measurements on a ponded sea-ice floe in the transition from summer to autumn reveal that snow accumulation was on average 0.03 m higher on refrozen melt ponds than on adjacent bare ice favored by the recessed topography of the ponds. Using under-ice radiation measurements from an ROV we show that due to the thicker snow cover on the melt ponds

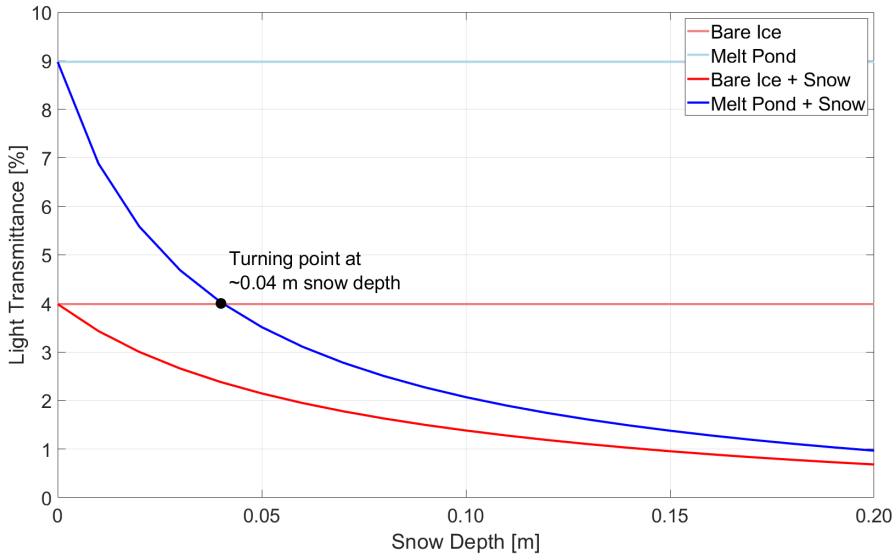

Figure 4.7: *Simulated light transmittance depending on the snow depth as modelled by DORT2002 for four cases: bare ice (light red), melt ponds (light blue), snow-covered bare ice (red), and snow-covered melt ponds (blue).*

the transmittance of the melt ponds can become lower than that of bare ice. Those results imply that melt ponds cannot be universally considered as bright windows of Arctic autumn sea ice. This finding is supported by computations from a RT model. Our findings can have consequences for the autumn ecosystem activity, oceanic heat budget, and thermodynamic ice growth if they can be observed in the entire Arctic.

Data availability statement

All data presented in this study are publicly available under the following DOIs:
ROV: doi:10.1594/PANGAEA.925698
Magnaprobe and GEM2: doi:10.1594/PANGAEA.934431
Aerial images: doi:10.5281/zenodo.5119094.

Acknowledgments

We thank the editor Harihar Rajaram and two anonymous reviewers for improving this work. This work was financed through the research programs PACES II and POF4 of the Alfred-Wegener-Institut Helmholtz-Zentrum für Polar-und Meeresforschung (AWI) and the Swedish Polar Research Secretariat (SPRS, grant no. AO18). Additional funding was received through the Diatom-ARCTIC project (NE/R012849/1; 03F0810A) as part of the Changing Arctic Ocean program (CAO), jointly funded by the UKRI Natural Environment Research Council (NERC) and the German Federal Ministry of Education and Research (BMBF). The ROV work was

supported by the Helmholtz Infrastructure Initiative “Frontiers in Arctic marine Monitoring” (FRAM). We are thankful to the captain, crew and scientists onboard the IB Oden, as well as to the SPRS and AWI logistics for facilitating our participation in the AO18 expedition. Our special thanks go to Matthieu Labaste, Helen Czerski, and Lars Lehnert for their field support, Ruzica Dadic for her advice on snow, and the polar bear guarding crew for keeping us safe. We also acknowledge financial support by the Open Access Publication Funds of AWI.

5. Evolution of the light field under a refreezing lead in spring

5.1 Abstract

The thinner and more dynamic sea ice of the future Arctic will cause an increase in the formation and coverage of leads which will subsequently lead to more thin ice. The resulting higher light transmittance through thin ice compared to adjacent thicker ice has implications for energy fluxes between atmosphere, sea ice, and ocean in the vicinity as well as for algal growth and accumulation rates beneath the ice. Observations under thin and new ice to quantify those implications are sparse, especially in the central Arctic in spring. Here, we present a time series of sea-draft and light transmittance data obtained under a refreezing lead using an ROV during the MOSAiC expedition in the Central Arctic throughout spring 2020. Our measurements indicate that the mean light transmittance of the refrozen lead was 15.5% only 1.5 weeks after formation, and dropped to 1.6% after another six weeks. This decrease in light transmittance is explained by continuous thermodynamical ice growth and snow accumulation. By the beginning of May, the mean transmittance of the lead ice was only 1.5% higher than that of adjacent, much thicker SYI. Snow dunes that formed at the flanks of a nearby ridge and at the lead edges contributed to the spatial variability of light transmittance.

5.2 Introduction

The Arctic sea ice is undergoing rapid and tremendous changes during the last decades (Meredith et al., 2019). The extent of sea ice is shrinking (Serreze et al., 2007; Stroeve et al., 2012). Old, thick MYI is replaced by younger (e.g., Maslanik et al., 2007; Stroeve and Notz, 2018) and thinner FYI (Haas et al., 2008; Kwok, 2018). Even though no significant changes in the strength of winds has been observed, the sea-ice drift speed increased (Rampal et al., 2009; Spreen et al., 2011). The thinning ice and increasing drift speed result in more frequent and more severe

dynamic events which foster lead formation (Rampal et al., 2009; Itkin et al., 2017). Leads are long, linear strips of open water that occur when the sea-ice cover breaks and diverges. Their occurrence exhibits a substantial spatial and temporal variability with hotspots in the Russian shelf seas, the marginal ice zones in Fram Strait and Barents Sea, the Beaufort Sea, and north of Greenland and Svalbard (Röhrs et al., 2012; Willmes and Heinemann, 2016).

Upward heat fluxes from the warm ocean towards the cold atmosphere are very high in a lead (Maykut, 1982; Perovich et al., 2011a). Thin ice forms quickly in a lead (Maykut, 1982) resulting in a dramatic increase in the albedo from 0.08 for open water to still low values of 0.40 for thin ice (Weller, 1972; Perovich and Grenfell, 1982; Perovich, 1996). Due to the low albedo of leads and thin ice, light transmittance is very high compared to thick and snow-covered ice (Taskjelle et al., 2016; Assmy et al., 2017; Kauko et al., 2017). The low thickness, low albedo, and high transmittance of thin ice significantly impact the solar heat input into the ocean, the mass and energy balance of Arctic sea ice as well as the ice- and ocean associated ecosystem.

Perovich (2005) showed that during spring none of the solar radiation incident on snow-covered sea ice was transmitted to the ocean compared to over 90% of that incident on leads. Kauko et al. (2017) measured PAR transmittances through a snow-covered lead between 5% and 41% in May 2015 north of Svalbard. Thicker ice covered by thick snow transmitted less than 0.3%. The transmittance of snow-free lead ice was significantly higher and ranged from 28% to 49%. Taskjelle et al. (2016) reported measurements of mean PAR transmittance between 77% and 86% of thin ice (thinner than 0.15 m) in a fjord in Svalbard in April 2010. Using a sophisticated RT model, they simulated a mean transmittance of 51%.

As biomass depends on sunlight, leads and refreezing thin ice play an important role for the ice- and ocean associated ecosystem in the Arctic (e.g., Kauko et al., 2017) and it is expected that the Arctic ecosystem is altered by more frequent leads. An increase in the occurrence and an earlier initiation of phytoplankton blooms were observed with possible impacts for the annual primary production estimates, marine food web, and carbon uptake (Assmy et al., 2017; Olsen et al., 2017). In turn, Taskjelle et al. (2017) observed that phytoplankton blooms increase water absorption and attenuation, and thus, alter solar heating of the upper water column. They found an increase in energy absorption of 36% under thin lead ice (0.25 m thick, 0.02 m snow) associated with the presence of a phytoplankton bloom in spring with consequences for ice melt.

While the physical, biological, and optical properties of leads have been observed in fjords in Svalbard (Taskjelle et al., 2016), in the pack-ice north of Svalbard (Assmy et al., 2017; Itkin et al., 2017; Kauko et al., 2017; Taskjelle et al., 2017), and in the Canadian Archipelago, no such observations exist for the Central Arctic in winter/spring where the occurrence of leads is low (Röhrs et al., 2012; Willmes and Heinemann, 2016).

We document the evolution of a lead in the Central Arctic in spring 2020 by means of under-ice

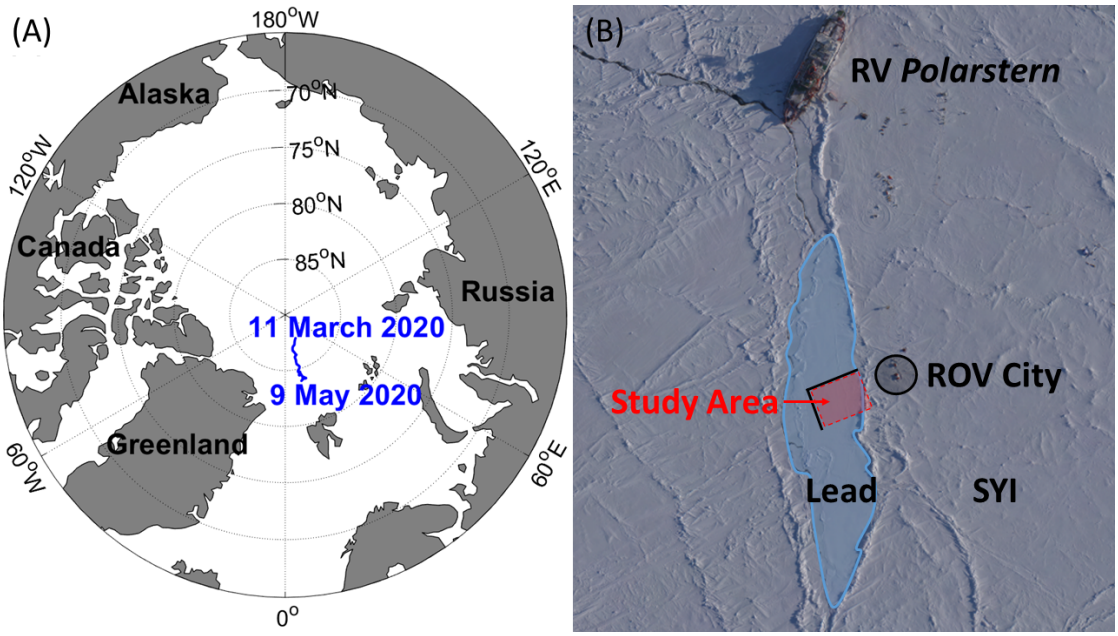

Figure 5.1: *(**A**) Geographic position of the MOSAiC ice floe from 11 March to 9 May 2020. The position was recorded by the Snow Buoy 2019S96. (**B**) Orthorectified aerial image of Polarstern and the study area on the refrozen lead as of 23 April (pers. communication Niklas Neckel, AWI).*

and aerial images, ice thickness/draft, and optical data gathered with an ROV. We present how the light transmittance of the lead ice gradually decreases with increasing ice draft and compare it with the light transmittance of adjacent much thicker SYI. We further combine results from a simple 1D FDD thermodynamic ice growth model with ice draft and optical measurements from the ROV.

5.3 Material and methods

5.3.1 Study site

The data presented in this study were collected during the Leg 3 of the Multidisciplinary drifting Observatory for the Study of the Arctic Climate (MOSAiC) drift expedition onboard the German research vessel *Polarstern* (AWI, 2017). A temporary ice camp was set up on drifting SYI (**Figure 5.1**). On 11 March, a lead opened close to *Polarstern* and ROV City. This lead refroze and collected a snow cover in the course of the Leg 3.

In-situ snow depth and sea-ice thickness as well as ROV-based sea-ice draft and transmitted irradiance were measured between 14 March and 9 May. The study focus was on the lead area of approximately 50 m x 50 m (study area) and adjacent SYI (**Figure 5.1B**). Marker poles (M0, M21-M34) were deployed under the ice to facilitate ROV navigation and to obtain a better co-location of the data (**Figure 5.1B**, black lines around the study site).

5.3.2 Under-ice transmittance

Horizontal transects of under-ice spectral irradiance were measured by a RAMSES-ACC hyperspectral radiometer (320-950 nm, TriOS GmbH, Rastede, Germany). The radiometer was mounted on a M500 ROV (Ocean Modules, Åtvidaberg, Sweden, Katlein et al., 2017). The ROV was lowered into the water through a 1.5 m x 1.5 m hole in the ice. The light transmittance was calculated by wavelength-integrating the transmitted irradiance from 350 nm to 920 nm (Nicolaus et al., 2010) and normalizing by the incident downwelling planar irradiance recorded by an upward-looking reference sensor at the surface. The data were filtered for ROV pitch, roll ($0 \pm 10^{\circ}$) and distance to ice bottom (0-2.5 m), and noise was filtered from the spectra. For the lead data, only measurements between M24 and M32 were used for the analyses because of the influence of the ridge close to M23 and cracks that opened now and then close to M33 and M34.

5.3.3 Snow depth, sea-ice thickness and draft

In-situ snow depth was repeatedly measured at drill holes at the marker locations using a tape measure on 6, 16, 18, 25, 29 April and 2 May (**Table 5.1**). Between 11 and 22 March and between 22 and 6 April, the snow depth was assumed to be 0.01 m and 0.02 m, respectively. Ice thickness was measured only on 6 and 16 April when the markers and transponders were set-up on the lead (**Figure 5.2**).

The distance between the ROV and the ice bottom was recorded using a sonar altimeter (PA-500 High Precision Altimeter, Tritech, UK) with a measurement range between 0.1 m and 10 m and a frequency of 500 kHz. The depth of the ROV was measured by a pressure sensor (Keller A-21Y, Keller AG, Jestetten, Germany) included in the main electronics housing and by a CTD (pumped SBE GPCTD, Seabird Scientific, USA) mounted on the ROV. The sea-ice draft was calculated from the distance to the ice bottom and the cross-calibrated depth using ROV and CTD depth. Data collected under the lead ice were identified by drafts between 0.1 m and 1.0 m and SYI data by drafts between 1.0 m and 3.0 m. Very thin ice with drafts < 0.10 m and open water were excluded from the analyses. This was necessary to focus on the continually refreezing lead as from time to time new cracks opened and very thin ice formed. Besides, the altimeter is unable to give a reasonable distance to thin ice and open water. An error of 0.04 m in sea ice draft arises from the maximum pitch and roll of $\pm 10^{\circ}$ and the maximum distance to the ice bottom of 2.5 m. The data were not corrected for varying sound speed.

Table 5.1: *Statistics of transmittance (%) and sea-ice draft (m) measurements of lead ice and SYI. N is the number of measurements. The modes were read from histograms with bin widths of 0.5% and 0.05 m, respectively. Pitch and roll filter ± 10°. Classified using sea-ice draft: lead > 0.10 m & <= 1 m, SYI > 1 m & <= 3 m. 2.5 m distance to ice bottom, depth cross-calibrated using vehicle depth and CTD, negative draft discarded.*

Parameter	Ice type	Date	N	Min	Max	Mean	Std	Median	Mode
Transmittance [%]	Lead	22.03.	54	3.1	22.6	15.5	4.6	16.7	16.5 - 17.0
		28.03.	38	1.9	4.1	3.0	0.7	2.9	2.0 - 2.5
		07.04.	59	1.4	4.9	3.0	0.9	2.9	2.5 - 3.0
		11.04.	24	1.6	3.9	2.7	0.9	2.5	1.5 - 2.0
		18.04.	41	1.5	2.9	2.2	0.4	2.1	1.5 - 2.0
		25.04.	20	1.4	2.5	1.8	0.4	1.7	1.5 - 2.0
		01.05.	120	1.2	2.4	1.7	0.3	1.7	1.5 - 2.0
		02.05.	370	1.1	2.3	1.6	0.3	1.6	1.5 - 2.0
		09.05.	364	0.4	4.5	2.6	0.6	2.6	2.5 - 3.0
	SYI	22.03.	770	0	15.8	0.2	0.7	0.1	0 - 0.5
		28.03.	80	0	4.3	0.2	0.6	0	0 - 0.5
		07.04.	-	-	-	-	-	-	-
		11.04.	235	0	15.1	0.5	1.3	0.1	0 - 0.5
		18.04.	89	0	15.4	0.4	1.7	0	0 - 0.5
		25.04.	181	0	9.2	0.7	1.3	0.3	0 - 0.5
		01.05.	11	0	1.4	0.7	0.4	0.7	0.5 – 1.0
		02.05.	180	0	5.7	0.1	0.5	0	0 - 0.5
		09.05.	296	0	2.0	0.2	0.3	0	0 - 0.5
Sea-ice draft [m]	Lead	22.03.	54	0.10	0.60	0.14	0.09	0.11	0.10 - 0.15
		28.03.	38	0.10	0.37	0.16	0.06	0.15	0.10 - 0.15
		07.04.	-	-	-	-	-	-	-
		11.04.	24	0.12	0.85	0.36	0.22	0.27	0.20 - 0.25
		18.04.	41	0.24	0.48	0.32	0.06	0.30	0.25 - 0.30
		25.04.	20	0.17	0.46	0.30	0.09	0.27	0.25 - 0.30
		01.05.	120	0.11	0.50	0.30	0.07	0.28	0.25 - 0.30
		02.05.	370	0.15	0.63	0.39	0.08	0.36	0.30-0.35
		09.05.	364	0.17	0.81	0.51	0.09	0.48	0.40 - 0.45
	SYI	22.03.	770	1.00	2.99	1.75	0.51	1.66	1.20 - 1.25
		28.03.	80	1.18	2.99	1.91	0.57	1.73	1.65 - 1.70, 1.75 – 1.80
		07.04.	-	-	-	-	-	-	-
		11.04.	235	1.01	2.99	1.85	0.58	1.74	1.05 - 1.10
		18.04.	89	1.00	2.88	1.71	0.55	1.44	1.30 - 1.35
		25.04.	181	1.01	2.72	1.51	0.44	1.35	1.25 - 1.30
		01.05.	11	1.19	2.93	1.90	0.10	1.86	1.85 - 1.90
		02.05.	180	1.00	2.97	1.85	0.56	1.61	1.30 - 1.35
		09.05.	296	1.01	3.00	1.98	0.62	1.79	1.50 - 1.55

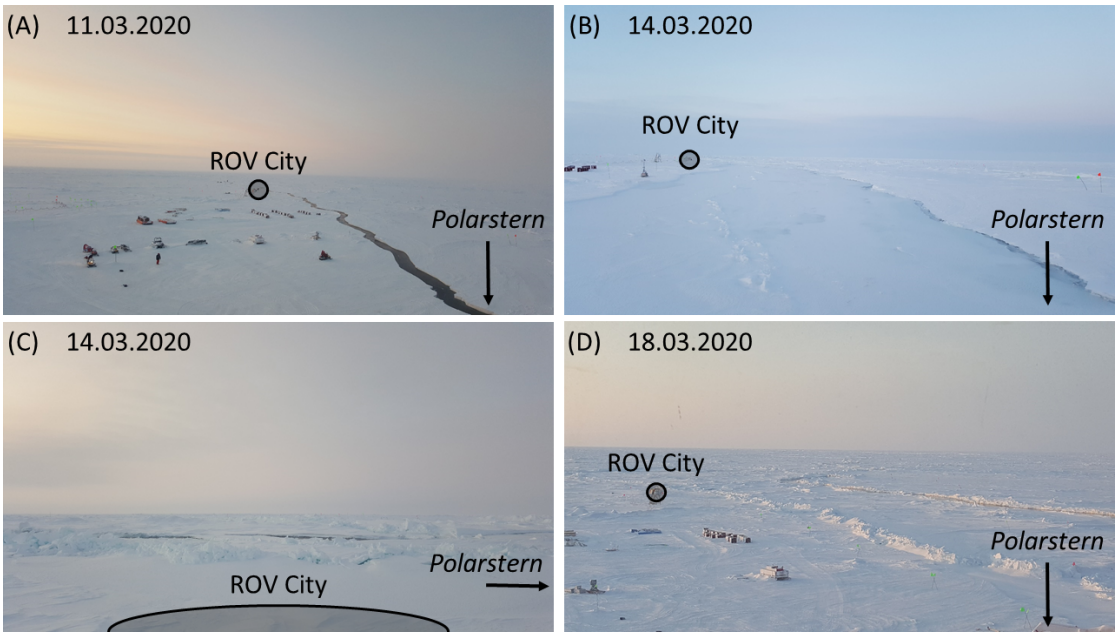

Figure 5.2: *Images of the lead evolution from the surface taken using a smartphone.*

5.3.4 Sea-ice growth model

A simple thermodynamic ice-growth model (Pfirman et al., 2004) based on the number of FDDs was used to simulate the ice thickness evolution of the refreezing lead. The change in ice thickness was calculated from a balance between latent heat of freezing/melting, the conductive heat loss, and ocean heat flux (**Equation 2.15**). The model was forced with air temperatures recorded by the Snow Buoy 2019S96 deployed about 1.8 km away from *Polarstern* and the lead. A freezing temperature of water of -1.9°C was used. The initial ice thickness was zero. We used thermal conductivities of ice κ_i and snow κ_s of 2.0 W m^{-1} K^{-1} and 0.2 W m^{-1} K^{-1}, respectively. Ice density ρ_i and latent heat of fusion L_i were set to 917 kg m^{-3} and 333.5 kJ kg^{-1}, respectively. The simulations were performed with a constant ocean heat flux of 2.0 W m^{-2} which is in agreement with earlier studies (e.g., Untersteiner, 1961; Meyer et al., 2017; Peeken et al., 2018). *In-situ* snow depth measurements d_s were used except for 16 April because only two measurements were collected (**Table 5.2**). The ice thickness was calculated at increments of 1 hour in accordance with the resolution of the air temperature measurements.

5.3.5 Aerial, surface-based, and underwater images

Oblique aerial images were obtained during helicopter flights on 17 and 23 April. The image taken on 17 April was corrected for camera perspective and georeferenced using the ROV markers (M0, M21, M23-M33). The image taken on 23 April was initially corrected for vignetting

Table 5.2: *In-situ sea-ice thickness, draft, and snow depth measurements on the lead. Bold values are shown in* ***Figure 5.10****.*

Marker M	Date	06.04.	06.04.	16.04.	16.04.	18.04.	25.04.	29.04.	02.05.
		Ice draft [m]	Snow depth [m]	Ice draft [m]	Snow depth [m]	Snow depth [m]	Snow depth [m]	Snow depth [m]	Snow depth [m]
0			0.23				0.37	0.33	0.38
21		-0.05	0.14			0.32	0.35	0.37	0.36
22						0.35	0.43	0.34	
23		0.52	0.05			0.35	0.08	0.08	0.42
24		0.47	0.04			0.08	0.05	0.06	0.10
25		0.54	0.04			0.07	0.07	0.07	0.08
26		0.33	0.04			0.07	0.08	0.07	0.08
27		0.32	0.05			0.07	0.07	0.08	0.09
28		0.32	0.03			0.08	0.05	0.05	0.09
29		0.32	0.04			0.05	0.07	0.07	0.07
30		0.32	0.07			0.06	0.08	0.10	0.08
31		0.33	0.06			0.08	0.05	0.09	0.10
32		0.32	0.06			0.07	0.08	0.08	0.10
33		0.32	0.05			0.08			
34			0			0.07			
T1				1.09	0.23				
T2				0.46	0.07				
T5				0.42	0.08				
Mean, M0-M34		0.34	0.06			0.13	0.14	0.14	0.16
Mean, M24-M32		**0.36**	**0.05**			**0.07**	**0.07**	**0.07**	**0.09**
Mean, T2+T5				**0.44**	**0.08**				

effects and precise GPS and INS (inertial navigation system) measurements were assigned to the image via the images time stamps. The initial position of the image was then corrected for ice drift effects with the help of the GPS position of *Polarstern* at the time of image acquisition. From these datasets, orthomosaics were generated from a structure-from-motion approach implemented in the commercial Agisoft metashape software package. The standard procedure includes (1) alignment of images (2) construction of a sparse point cloud (3) construction of a dense point cloud (4) generation of a Digital Elevation Model (DEM) (5) generation of an orthomosaic. Orthomosaics are routinely exported at a spatial resolution of 1 m (per. communication, Niklas Neckel, AWI).

Surface-based images were taken using a SAMSUNG Galaxy S6 edge (SM-G925F). Underwater images were extracted from high quality videos taken by the ROV high definition zoom camera (Surveyor WAHD, Bowtech).

5.4 Results and discussion

A lead opened just next to *Polarstern* and about 20 m from ROV City in response to severe sea-ice dynamic and wind events on 11 March (**Figure 5.2A**). The lead split apart an area of level FYI adjacent to SYI. The evolution of the lead was documented with aerial and surface images as well as with under-water images from the ROV camera. Between 11 and 28 March,

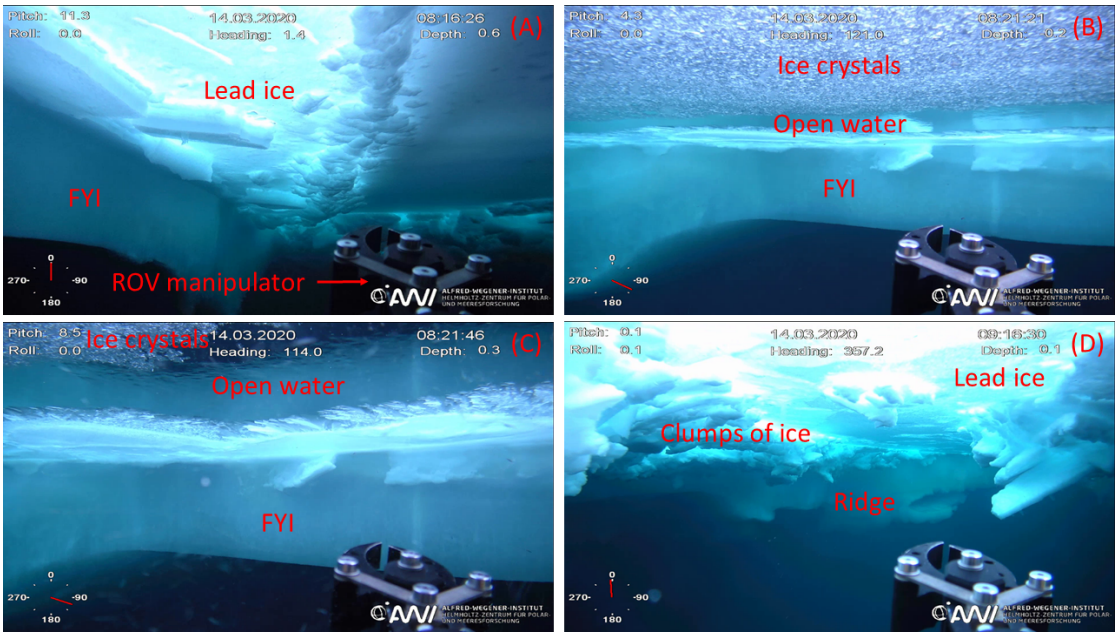

Figure 5.3: *ROV HD camera footage of the lead on 14 March.*

images are shown also for areas of the lead outside of the pristine study area in **Figure 5.1B**. In the beginning, the lead was about 5 m wide (**Figure 5.2A**). Over time it had increased in size and was partly refrozen, partly still open, and also new cracks opened, for example on 18 March (**Figures 5.2-5.4**).

Due to the dynamic events that led to the opening of the lead, the lead was filled with thick clumps of ice (**Figure 5.4**). Ridges have formed on either side of the lead (**Figures 5.2D**, **Figure 5.4B**, **C**). In the beginning, the ridges formed a narrow canyon (**Figure 5.4C**). Platelet ice had formed at some locations at the ridge keels.

By 22 March, the lead was completely frozen, reached a width of about 80 m, and developed into a uniform and smooth thin ice layer with a mean ice draft of 0.16 m (**Figure 5.5**, **Table 5.1**). Brine rejection from the growing lead ice was observed in form of brinicles (**Figure 5.5A**). However, it was not investigated whether gravity drainage (Notz and Worster, 2009), pressure fluctuations from below or volume expansion (Petrich and Eicken, 2017) was the dominate process for the brine rejection.

5.4.1 Evolution of lead-ice thickness

Since 22 March sea-ice draft measured using the ROV were considered reliable as the lead was stable and it was possible to collect data from roughly the same area. However, the structure of the underside of the lead ice varied also spatially (**Figure 5.6**). Occasionally, small areas of open water appeared (**Figure 5.6A**).

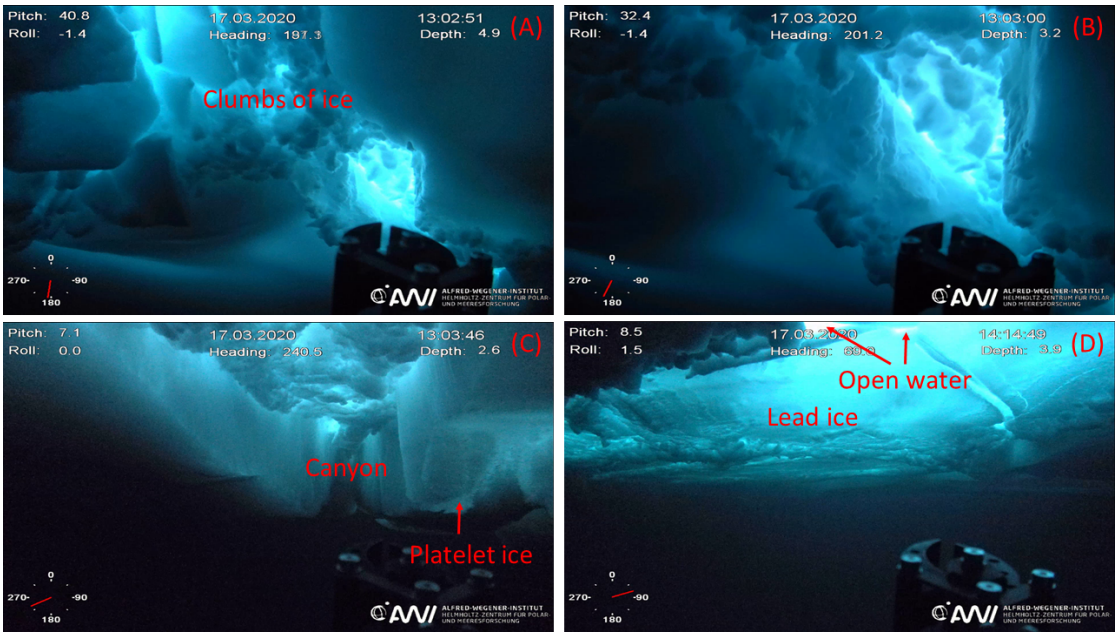

Figure 5.4: *ROV HD camera footage of the lead on 17 March.*

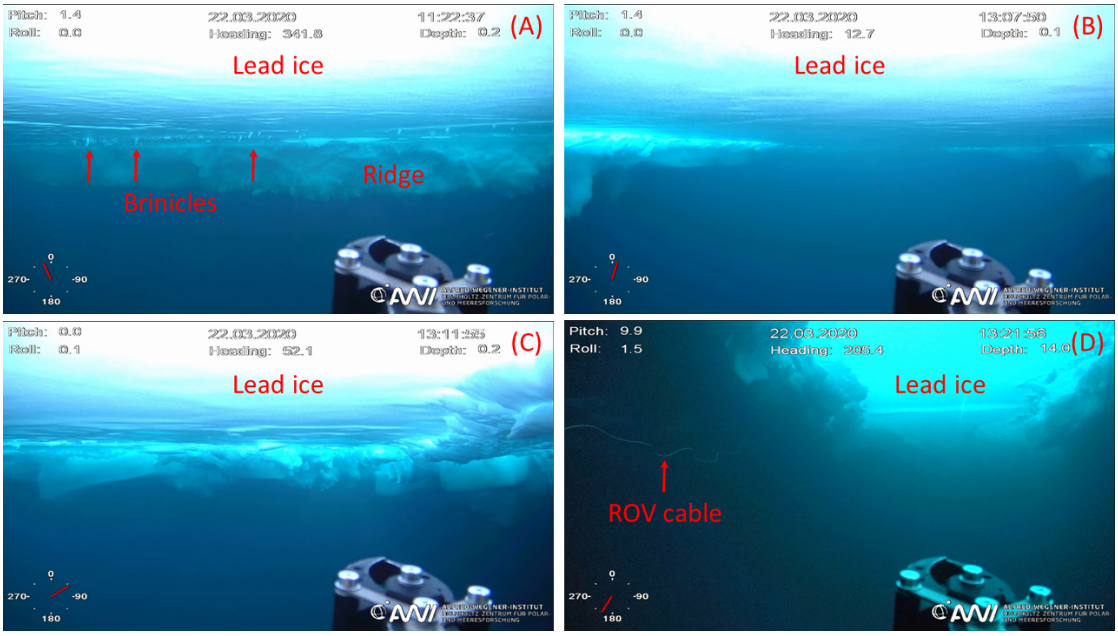

Figure 5.5: *ROV HD camera footage of the lead on 22 March.*

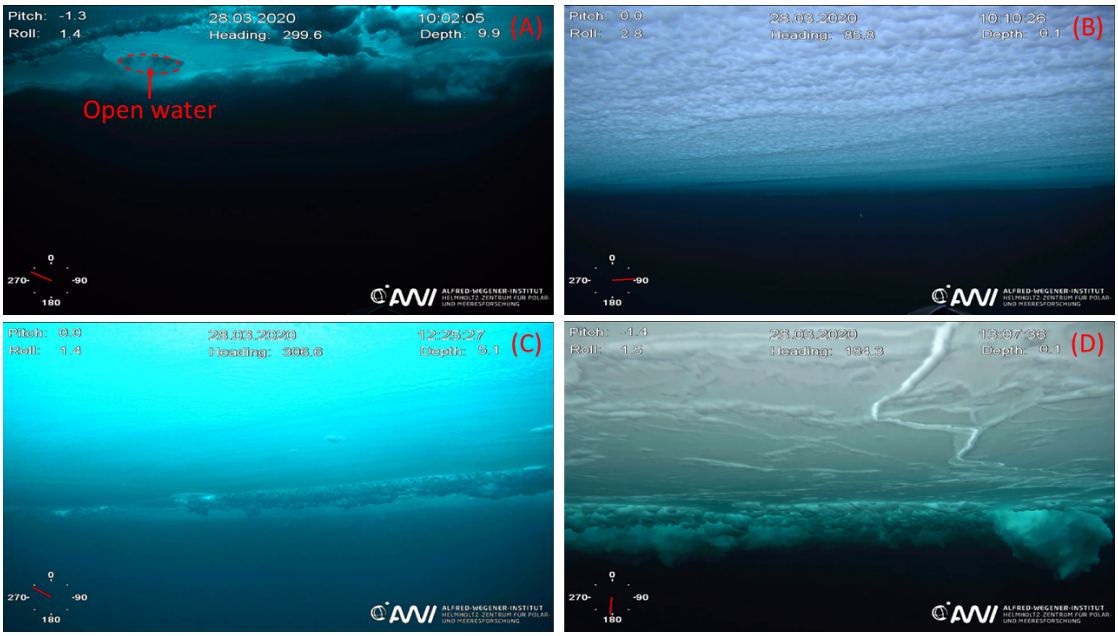

Figure 5.6: *ROV HD camera footage of the lead on 28 March.*

On 6 April, a grid system was established on the lead ice consisting of marker poles (M0, M21-M34) that were deployed in the water (**Figures 5.7** and **5.8**). The markers were very useful for navigation with the ROV as well as to orientate under the lead and enabled to perform measurements continuously at the same spots.

Since 7 April, sea-ice draft was measured along the marker pole transects. Consequently, since then the more or less same ice area was investigated and results can be assumed more reliable than on dates before. However, a crack opened along the lead close to M34 (**Figures 5.8B**, **C** and **5.9D**) which influenced the draft measurements between M32 and M34.

The sea-ice draft varied also spatially along the transect and across the lead study area (**Figure 5.7**). The draft between M0 and M23 close to the ridge between ROV City and the lead was higher. Near M23, the draft was still as high as 0.7-0.8 m compared to the mean draft of 0.39 m between M24 and M32 on 2 May (**Table 5.1**). Due to the influences of the crack close to M34 and of the ridge, the following analyses of the temporal evolution of sea-ice draft is restricted to measurements collected between M24 and M32.

The ridge partly blocked the acoustic signal from the ROV positioning system. A new set of transponders T1, T2, and T5 was deployed on the refrozen lead on 16 April to circumvent this issue (**Figure 5.7A**). A reliable position of the ROV was not available until 18 April, however due to the markers deployed on 6 April, measurements collected since then are considered reliable. Uncertainties remain in the measurements collected on 22 and 28 March and could not be reduced with the presented data.

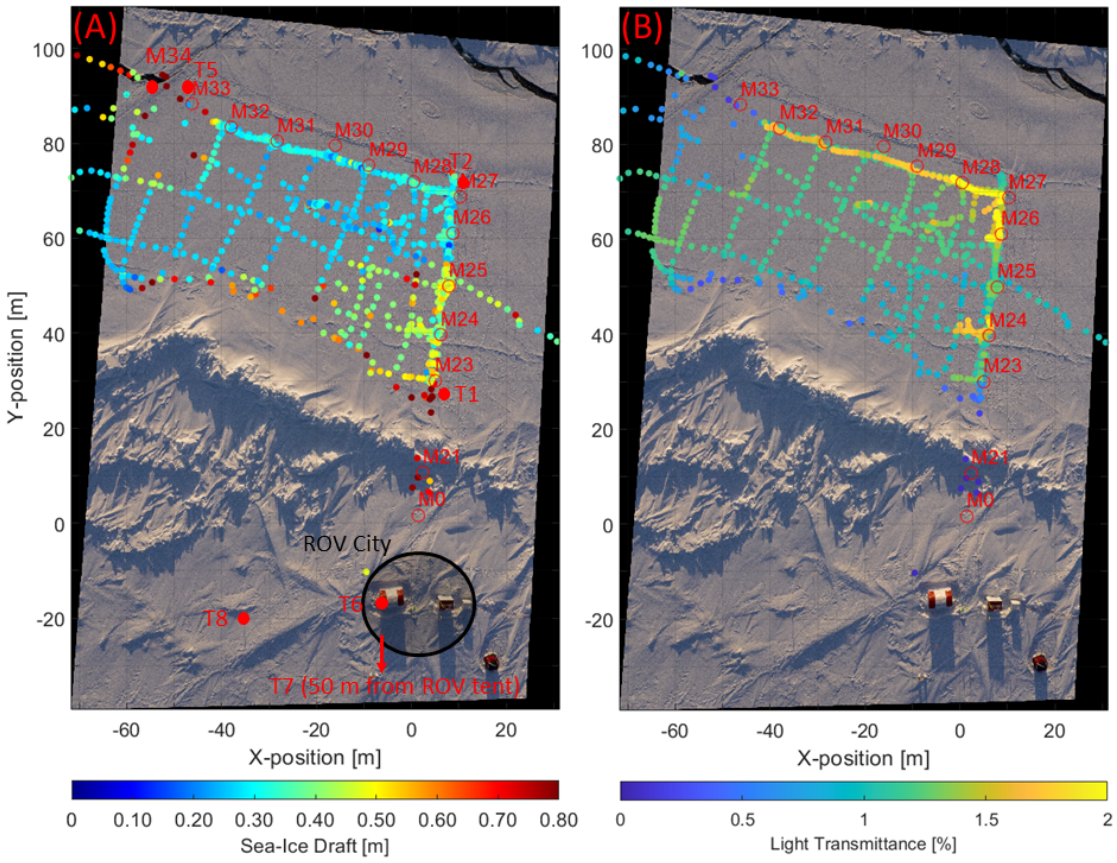

Figure 5.7: *(**A**) ROV-based sea-ice draft and (**B**) light transmittance of the lead ice as measured on 2 May 2020. The background image is an orthorectified aerial image acquired during a low helicopter flight on 17 April 2020 (pers. communication Manuel Ernst, UFA Show & Factual). The marker poles were set up on 6 April 2020. Red labels indicate the marker (M) and transponder locations (T) while filled circles were not used for the image registration. The ROV tent, control hut, and power hub are visible on the lower right corner of the image (ROV City).*

Sub-zero air temperatures prevailed almost throughout the sampling period (**Figure 5.10A**). During the first half of the sampling period, from 11 March until 13 April, air temperatures ranged between -30 °C and -20 °C with occasional peaks above -20 °C. In contrast, during the second half, the air temperatures significantly increased and oscillated between -20 °C and -10 °C with occasional peaks of near and above zero.

Due to the low air temperatures, sea ice formed quickly in the lead. The *in-situ* sea-ice draft measurements showed that on average the lead ice grew to 0.36 m by 6 April and to 0.44 m by 16 April, 3.5-5 weeks after the lead opened (**Table 5.2**, **Figure 5.10B**). The freeboard was only 0.01 m. The average snow depth on the lead increased from 0.05 m on 6 April to 0.09 m on 2 May (**Table 5.2**). Prior to 6 April, no snow depth measurements were performed, but snow depth values of 0.01 m between 11 and 22 March and 0.02 m between 22 March and 6 April were assumed.

The mean ROV sea-ice draft increased from zero on 11 March, the day when the lead opened,

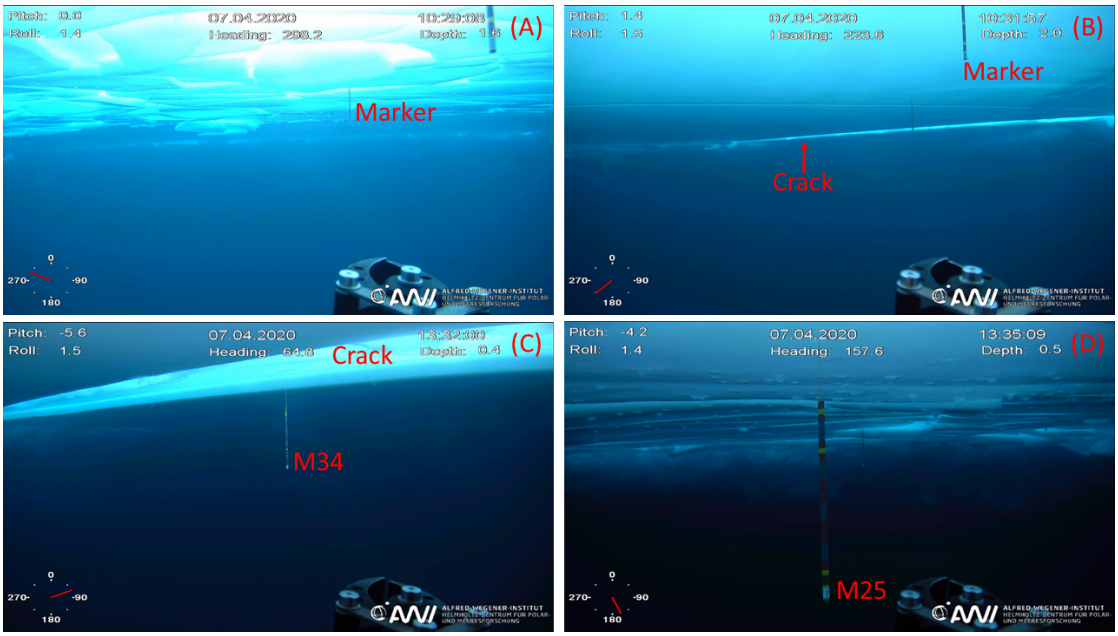

Figure 5.8: *ROV HD camera footage of the lead on 7 April.*

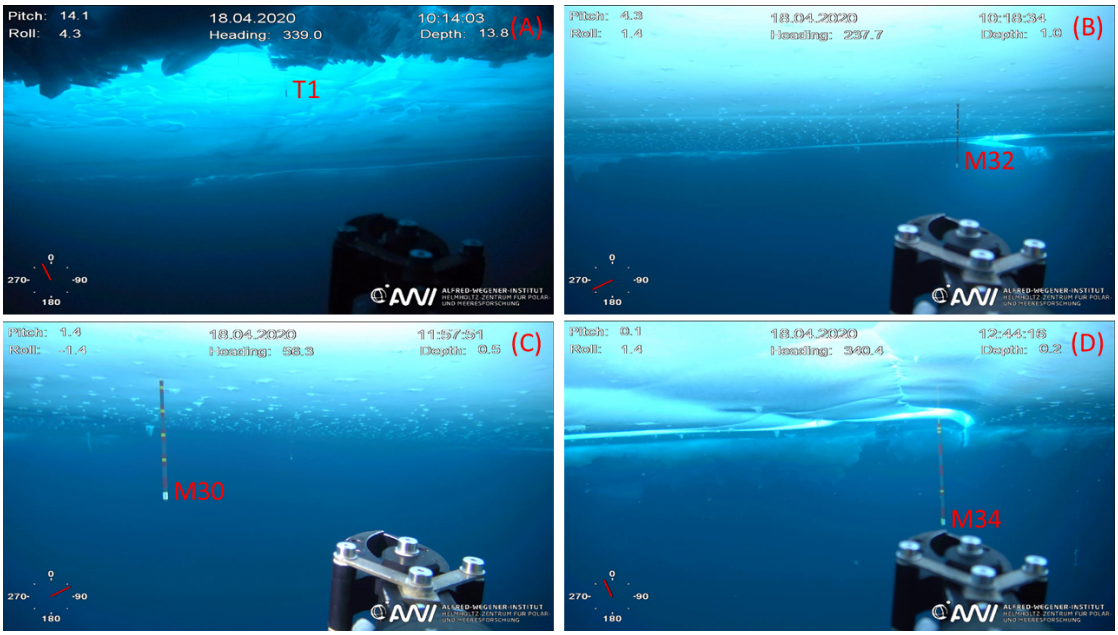

Figure 5.9: *ROV HD camera footage of the lead on 18 April.*

to 0.36 m on 11 April (**Figure 5.10B**, **Table 5.1**). Then, the draft decreased to 0.30 m and 0.32 m, however remained within one standard deviation of the draft from 11 April. The decrease in draft might imply short periods of melting fostered by air temperatures near and above zero. The temperature signal could have had an impact on the draft because the *in-situ* ice freeboard was only 0.01 m (not shown). However, the temperature signal was very unlikely to penetrate deep enough into the ice to initiate melting. Thus, the apparent decrease in draft

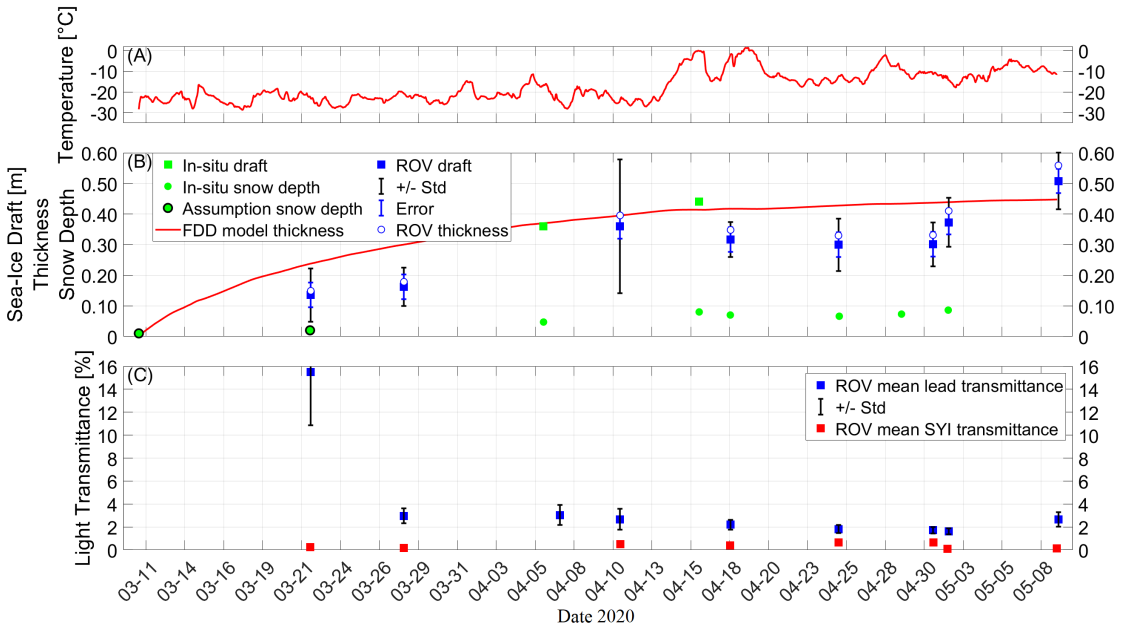

Figure 5.10: *Time series of (**A**) air temperature from the Snow Buoy 2019S96 (Nicolaus et al., 2020), (**B**) in-situ mean sea-ice draft and snow depth, modelled ice thickness, and ROV mean sea-ice draft and (**C**) ROV mean light transmittance of the refreezing lead ice and SYI. The error bars for the ROV draft in (**B**) are 0.04 m. The ROV thickness was converted from ROV draft using a conversion factor of 1.1.*

was attributed to measurement uncertainties. On 2 May, the draft increased again towards 0.39 m and continued to increase to the peak draft of 0.50 m on 9 May. On average, the draft of adjacent SYI ranged from 1.51 m to 1.95 m (**Table 5.1**) and the mean depth of the SYI snow cover increased from 0.27 m in March to 0.32 m in May (pers. communication, Stefanie Arndt, AWI). During the peaks of near and above zero air temperatures, the simulated conductive heat flux from the FDD model was smaller than the ocean heat flux, implying melting (not shown). This effect might have been amplified by a thickening snow layer from 0.05 m on 6 April to 0.09 m on 2 May which might have reduced the conductive heat flux and thus, hampered ice growth due to the high insulation properties of snow (e.g., Sturm et al., 1997).

The simulated ice thickness increased consistently from zero on 11 March to 0.45 m on 9 May (**Figure 5.10B**). Except for on 11 April and 9 May, the simulated ice thickness was higher than the ice thickness that resulted from converting the measured draft to thickness using a conversion factor of 1.1 (e.g., Katlein et al., 2019). Especially in the beginning on 28 March and between 18 April and 1 May the simulated ice thickness was 0.07 m to 0.12 m higher than the from draft converted ice thickness. This discrepancy could be explained by the still deforming lead between 14 and 17 March (**Figures 5.3** and **5.4**). During that period and also between 11 and 14 March, the lead experienced further deformation and reopened due to wind events where open water areas and very thin ice formed again. As a result, the converted ice thickness of the refrozen lead that was stable since 22 March (**Figure 5.5**) was naturally lower than the

simulated ice thickness which was represented by a continuously thickening ice layer without interruptions in its growing.
Taskjelle et al. (2016) observed an increase in thickness of lead ice in a fjord in Svalbard from 0.07 m to 0.15 m within nine days. The FDD model calculated such an increase within only four days which might be a result of different atmospheric conditions (**Figure 5.10B**, between 13 and 17 March).

5.4.2 Evolution of light transmittance

Spatial variations in light transmittance in the order of 0.5% to 1% were measured along the transect from M24 and M32 (**Figure 5.7B**). The light transmittance was significantly lower from near M24 to M26 than from M26 to M32. The *in-situ* snow depth measurements along the transect show no significant variability on any day of sampling that would explain the variability in light transmittance (**Table 5.2**). The mean snow depth at both M24-M26 and M27-M32 was 0.09 m on 2 May. Differences between the mean snow depths of prior measurements were not significant.
The mean ROV light transmittance of the lead ice decreased gradually from 15.5% on 22 March to 1.6% on 2 May with the exception on 9 May where the mean transmittance was with 2.6% higher than on 2 May (**Figure 5.10**, **Table 5.1**). Adjacent thick SYI covered by a thick snow cover transmitted only 0.1% to 0.7% of the light incident on the surface (**Figure 5.10C**, **Table 5.1**). Besides the much thinner lead ice, the mean transmittance of the lead was only 1.5% higher than that of SYI on 2 May (**Figure 5.10C**, **Table 5.1**). This indicates that the role of leads as a window into the underlying ocean can become less pronounced than documented in other studies (e.g., Kauko et al., 2017).
In contrast, Assmy et al. (2017) and Kauko et al. (2017) present transmittances ranging between 5% and 42% for a refreezing lead north of Svalbard, much higher than the transmittance of adjacent thicker ice which was below 0.3%. However, their lead ice was much thinner with a mean thickness between 0.20 m and 0.25 m. The mean snow depth ranged from 0.02 m to 0.06 m. Their thicker ice was as thick as 1.30 m and had a thick snow cover of 0.40 m.
Kauko et al. (2017) performed additionally an experiment where they removed the snow layer of the lead and measured a twofold to sevenfold increase in PAR transmittance to 28% to 49%. This underlies the strong effect of a thin snow layer on the PAR transmittance. Taskjelle et al. (2016) measured transmittances 65-76% of snow-free lead ice with thickness 0.07 m to 0.15 m a Svalbard fjord in April, respectively.

5.4.3 Influence of other constituents on the light transmittance

Other factors than sea-ice draft or generally thickness and snow depth might have influenced the light transmittance of the refreezing lead. The structure of the sea ice (**Figure 5.6**) such as the ratio of columnar to granular ice which depends on the conditions during freeze-up might explain some variations (Kauko et al., 2017).
In this study, brine and air bubble content that might be trapped in a significant high amount in the refreezing lead ice was not taken into account but is generally shown to have a strong impact on the transmittance (Taskjelle et al., 2016; Kauko et al., 2017). However, brine volume decreases with decreasing ice temperature. Brine might have been completely expelled by 9 May which might have resulted in lower albedo due to the ice being smoother (Perovich and Grenfell, 1981) and, thus, probably in higher transmittance (**Figure 5.10C**).
Assmy et al. (2017) observed a phytoplankton bloom underneath thin lead ice with a modal ice thickness of 0.20 m and a snow cover between 0.01 m and 0.06 m. Taskjelle et al. (2016) propose that biomass in the ice impact the transmittance of ultra violet radiation. Even though biomass was only identified under cracks (**Figure A.1D**), it cannot be ruled out that the transmittance was influenced through absorption by particulate matter in this study (Arrigo et al., 1991; Mundy et al., 2007; Wongpan et al., 2018).

5.4.4 Relationships between thermodynamics and optics

The relationship between ROV-based sea-ice draft and light transmittance of the refrozen lead could only be moderately described (**Figure 5.11**). The exponential relationship is of the form as **Equation 2.11** besides the wavelength-dependence of the transmittance t_m that is not considered in this study: $t_m(d_i, d_s) = i_0 \cdot exp(-k_i d_i - k_s d_s)$. The goodness of the fit (R^2) was 0.59 and the RMSE of the transmittance was as high as 3.3%. In the fit equation shown in **Figure 5.11**, the coefficient 0.48 is i_0 which is the fraction of the incident radiation that is not reflected at the surface or absorbed within the snow but penetrates into the sea ice. A widely used value for i_0 is 0.35 (Grenfell and Maykut, 1977). The coefficient -10.55 in the exponent of the fit is $-(k_i d_i + k_s d_s)$, where k_i and k_s are the broadband extinction coefficients of sea ice and snow, and d_i and d_s the ice thickness or draft and snow depth, respectively. Typical values for the broadband extinction coefficients of sea ice and freshly fallen snow are $k_i = 1.1\,m^{-1}$ (Grenfell and Maykut, 1977) and $k_s = 40\,m^{-1}$ (Thomas, 1963). Using those extinction coefficients and the measured ice draft and snow depth of $d_i = 0.39\,m$ and $d_s = 0.09\,m$ from 2 May (**Tables 5.1** and **5.2**), respectively, yields a coefficient in the exponent of the fit of -4.35. This value is 60% lower than that given by the fit. Further, a transmittance of 0.9% results, which is about 60% of the transmittance measured using the ROV on 2 May (**Figures 5.10** and **5.11**, **Table 5.1**). Clearly, the measurements that at least follow the fit are those measured on 28 March and 9 May.

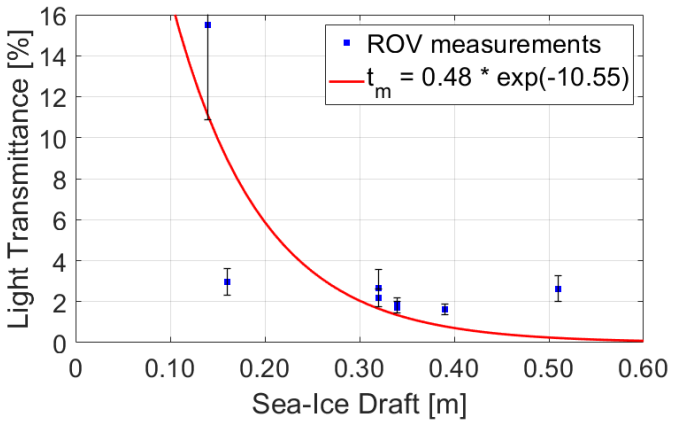

Figure 5.11: *Exponential fit of the relationship between ROV-based sea-ice draft and light transmittance of the refrozen lead. Note that the sea-ice draft measurements were adjusted according to their measurement error in such that they follow monotonically the exponential fit. t_m is the transmittance. The fit was created using the curve fitting toolbox in MATLAB^{TM}.*

This sample calculation demonstrates that the relationship between thermodynamics and optics of thin, growing ice is very complicated and might not be as easily described with bulk formulations of radiative transfer as applied for thicker ice. A main reason might be the neglected light source term in the radiative transfer formulation (**Equations 2.6** and **2.8**) which can only be neglected when boundaries are far away. Even though this is common practice, this condition is seldom met in sea ice. Unfortunately, including light sources complicates the retrieval of a solution of radiative transfer in sea ice dramatically and is far beyond the scope of this study.

5.5 Outlook

The analysis performed in this study would benefit from the extensive 3D under-ice topography data which were collected using a multi-beam attached to the ROV (**Figure 2.13A**). The multi-beam has a better horizontal and vertical resolution than the single sonar altimeter point measurements. Further, the multi-beam surveys were performed at a diving depth of 20 m for which the acoustic positon of the ROV was more reliable and showed rarely interruptions as no ridges or undulating SYI blocked the signal. Thus, ice draft derived from the multi-beam under-ice topography is expected to improve the classification of lead ice and thus, the relationships between thermodynamic and optics.

The uncertainty in the variability of transmittance could be reduced by including additional snow depth measurements derived from time series of surface elevation with a spatial resolution of 0.5 m from an airborne laser scanner.

Simulations using a sophisticated model might help to understand the radiative transfer in thin

ice which was not achieved by applying the bulk radiative transfer formulation (**Figure 5.11**). In the radiative transfer formulation (**Figure 5.11** and **Equation 2.11**), brine as well as air bubbles were not considered. However, air bubbles strongly scatter radiation and brine attenuates radiation through both scattering and absorption (**Sections 2.1.6** and **2.1.7**). Thus, their effect on the transmittance should be considered, especially as brine content in new, thin ice can be very high (Malmgren, 1927; Petrich and Eicken, 2017).
Lastly, considering spectral-dependencies of the transmittance as well as in sea-ice and snow extinction coefficients may improve this study.

5.6 Summary

Only few observational studies exist that focus on the connection between thermodynamics and optics of newly formed ice in the Central Arctic. We established relationships between sea-ice draft and transmittance of a refreezing lead in the Central Arctic during the Leg 3 of the MOSAiC expedition in spring 2020. The main finding shows that the connection between thermodynamic and optical properties of thin and refreezing lead ice could not be described by the common assumptions made in bulk formulations of radiative transfer. This might be due to additional light sources across the boundaries of thin ice which are not considered. However, this remains speculative until sophisticated radiative transfer computations are performed.
The transmittance of the refreezing lead ice dropped quickly to 3% once the ice had grown to 0.20 m thickness. Continuous thickening and a snow cover of 0.10 m resulted in a mean transmittance of only 1.5% higher than that of adjacent thick and heavily snow-covered SYI after two months of the lead's opening. This points toward a less pronounced role of a refreezing lead as a window into the underlying ocean.
This study could reduce uncertainties in how solar radiation is partitioned by the thin ice. The transmittance through thin ice is very high, highlighting the need to understand the connection between thermodynamics and optics for thin ice in detail. As the more dynamic and vulnerable sea-ice cover of the changing Arctic foster the formation of leads and subsequent formation of thin ice, potential impacts on the total solar energy budget, the heat input into the ocean, and the ice- and ocean-associated ecosystem arise.

5.7 Data availability statement

Data presented in this study are publicly available at the PANGAEA or will be in the near future under the following DOIs:
ROV: doi:10.1594/PANGAEA.935688 (dataset in review)
Snow Buoy 2019S96: doi:10.1594/PANGAEA.925326 (dataset in review)

In-situ: Preparation for data upload to PANGAEA
Aerial images: pers. communications Niklas Neckel (AWI) and Manuel Ernst (UFA Show & Factual)

5.8 Acknowledgments

Special thanks for the support in the field goes to Stefanie Arndt, Serdar Sakinan, Susanne Saphic, Falk Pätzold, David Clemens-Sewall, Steven Fons, Robert Ricker, Amy MacFarlane, Jennifer Hutchings, Igor Sheikin, Alexey Niubom, Frederik Tardeck, Reza Naderpour, Lars Kaleschke, Christian Katlein, Marcel Nicolaus, Clara Hoppe, the polar bear guide team as well as to Niklas Neckel and Manuel Ernst for providing aerial images.

6. Key findings and outlook

Due to the ongoing environmental changes in the Arctic, the dominant sea-ice types, surface properties and conditions are expected to shift to a more seasonal ice cover. This will lead to a decline in sea-ice extent and thus, a decrease in snow-covered sea ice, as well as an increase in melt pond coverage and occurrence of leads. As a result, the sea-ice cover will be more vulnerable and experience more frequent dynamic events. These changes will strongly influence the partitioning of the solar radiation, including implications on the sea-ice energy and mass balance through the ice-albedo feedback, on the heat input into the ocean, and on the ice- and ocean-associated ecosystem. The relationships of the changing Arctic sea-ice types and solar radiation open a new key knowledge gap and increase uncertainties in our current understanding of those relationships. Thus, our knowledge of direct relationships of the surface conditions and solar radiation need to be broadened and deepened. This will enable us to monitor and assess how the changes in the Arctic sea-ice cover and thus, partitioning of solar radiation evolve in and affect the new Arctic. Therefore, the studies in this dissertation broaden and deepen our knowledge of direct relationships of the surface conditions and solar radiation. This will enable us to monitor and assess how the changes in the Arctic sea-ice cover and thus, partitioning of solar radiation evolve in and affect the changing Arctic.

6.1 Relationships between sea-ice surface conditions and solar radiation

This dissertation constitutes a step forward toward monitoring and understanding impacts of the snow and surface conditions on the solar radiation flux through Arctic sea ice during different seasons. It focusses on the sea-ice surface conditions and properties that are observed and predicted to dominate in the changing Arctic due to the ongoing environmental changes. In particular, relationships between the surface conditions and the under-ice radiation during the shoulder seasons spring and autumn are established. In spring and autumn, especially the timing of the seasonal progression in under-ice radiation can have significant impacts on the total annual energy budget. While measurements of the optical properties of sea ice are

abundant in summer in the central Arctic, gaps exist in particular for spring and in areas outside the central Arctic. This emphasizes the need for a better understanding of spring and autumn sea-ice processes.

The research carried out in **Chapters 3**, **4**, and **5** successfully achieved the **overarching goal**: To broaden and deepen our knowledge of the relationships between sea-ice surface conditions and properties that are predicted to dominate in the future Arctic Ocean and under-ice radiation during spring and autumn. This goal was addressed by analysing field measurements using common and new measuring systems and methods (**Figure 2.13**). In particular, under-ice radiation measurements were collected using an ROV and autonomous radiation stations. Snow depth was measured *in-situ*, using a Magnaprobe, by Snow Buoys, and was derived from surface topography measurements using a terrestrial laser scanner. Ice thickness was measured *in-situ* at drilling holes and using electromagnetic induction sounding devices. Ice draft measurements were also performed *in-situ* and using a sonar altimeter attached to the ROV. The location and coverage of melt ponds were extracted from aerial images. Combining those measurements enabled to establish relationships between the sea-ice surface properties and conditions and under-ice radiation in detail and thus, to achieve the objectives of this dissertation.

Snow depth on FYI and MYI

Relationships between snow depth and under-ice radiation for snow-covered FYI and MYI in late spring and in the summer/autumn transition were established (**Chapter 3**). New approaches were introduced to parameterize the snow depth d_s using a statistical relationship between magnitude and spectral shape of under-ice radiation, NDI, as the predictor variable: $d_s = -0.58 \cdot NDI(651:616) - 0.04$ and $d_s = 1.21 \cdot NDI(440:403) + 0.11$ (**Equation 3.1** and **Figure 3.4**). The parameterizations have Pearson correlation coefficients of 0.69 and 0.78 and resulted in snow depth retrievals of combined RMSE of 6.1 cm. A second result of this chapter is a snow depth retrieval of a combined RMSE of 5.2 cm using a RT model: $t_m(d_i, d_s) = i_0 \cdot exp(-k_i d_i - k_s d_s)$ (**Equation 3.2** or **2.11**). Both methods reproduced spatial and temporal variabilities in snow depth well (**Figures 3.6**, **3.7**, and **3.8**). To this date, the analysis is limited to level landfast FYI in the Lincoln Sea in late spring and to level, melt-pond covered MYI in the central Arctic in the summer/autumn transition. The suitability of the parameterizations is hampered by certain atmospheric conditions and a lower limit in absolute light levels. Hence, a retrieval of snow depth during winter is not possible. Nevertheless, the radiation analysis (Chapter 3) resulted in relationships between snow depth and spectral under-ice radiation, which were applied and validated to retrieve snow depth from spatial and continuous measurements of under-ice radiation (**first objective**).

While satellite-based snow depth retrievals provide snow depth estimates over large regions

in the Arctic, the spatial and temporal resolutions are not applicable to floe-scale and simultaneously under-ice radiation measurements. The research performed here allows to retrieve snow depth directly from under-ice radiation measurements and thus, direct relationships for example the spatial and temporal variability in under-ice radiation can be investigated. Such a data set is very valuable for biological studies. This enables to better monitor and assess changes in sea-ice energy and mass balance, as well as the ice- and ocean-associated ecosystem and primary productivity.

Snow-covered melt ponds

Snow depth, under-ice radiation, and melt pond location allowed to investigate the effect of the snow cover on the melt ponds on the under-ice radiation for MYI in the summer/autumn transition (Chapter 4). A thicker snow cover accumulated on the melt ponds owing their recessed topography compared to bare ice (**Figures 4.3** and **4.6**). While such a thicker snow cover on melt ponds was observed before, coincident observations of under-ice radiation and the effect of the thicker snow cover on the under-ice radiation do not exist to this date. The 0.03-0.04 m thicker snow cover on the melt ponds led to lower levels of under-ice radiation of the melt ponds than that of adjacent bare ice (**Figure 4.1**). This finding can have consequences for the oceanic heat budget, thermodynamic ice growth, and autumn ecosystem activity as discussed and demonstrated in this chapter. Despite the small study area and melt ponds, the results are likely representative for other sea-ice floes within the entire Arctic Ocean. Thus, the established theory of high levels of under-ice radiation underneath melt ponds in both summer and autumn and how this is described in most computer models should be adapted in such that they include the observed situation which is currently not the case. With this study (Chapter 4), it was successfully accomplished to document and investigate the effect of refrozen and snow-covered melt ponds on the under-ice radiation and to compare results to the situation for adjacent bare ice (**second objective**).

The area where snow can deposit and accumulate shrinks both due to the declining sea-ice cover and the increase in the occurrence of open water areas such as leads. With the melt pond coverage on sea ice increasing, also the coverage of snow-covered melt ponds increases. Thus, the situation presented in Chapter 4 gains relevance in a changing Arctic and points to the need of further investigations on the effects of snow-covered melt ponds of different size, depth, and location on the energy budget of sea ice.

Refreezing lead and thin ice

The evolution of a refreezing lead with a focus on the relationships between sea-ice draft and under-ice radiation during spring was documented (Chapter 5). As a main result, the connection

between thermodynamics and optics could not be satisfactorily described by the commonly used exponential decay law of radiation in sea ice: $t_m(d_i, d_s) = i_0 \cdot exp(-k_i d_i - k_s d_s)$) (**Figure 5.11** and **Equation 3.2** or **2.11**). However, it remains unclear whether this is due to the simplistic approach to describe radiative transfer in thin ice, the neglected wavelength-dependency, or uncertainties and gaps of the applied measurements. This might be clarified by including additional data with better resolutions such as ice draft from a multi-beam attached to the ROV and surface elevation from an airborne laser scanner. Another result is that the under-ice radiation of the refreezing lead ice approached a level of only 1.5% above that of adjacent thick and heavily snow-covered SYI. This indicates that the lead's role as a bright window into the underlying ocean can be quickly limited. This study (Chapter 5) examined the connection between thermodynamics and optics of a refreezing lead and thin ice in comparison to the under-ice radiation of thick and heavily snow-covered SYI (**third objective**).

In the changing Arctic, the occurrence of open water areas such as leads increases due to the decrease in mechanical strength of the sea-ice cover. The levels of under-ice radiation under a refreezing lead are very high, at least in the beginning of its formation and evolution. Thus, the relationships between thermodynamics and optics of a refreezing lead need to be investigated and understood in detail to assess the changes in the Arctic, especially for sea-ice energy budgets and RT modelling of thin ice.

6.2 Perspectives for future field campaigns and research

This section gives examples and ideas for future research on the impacts of snow and surface conditions on the sea-ice energy and mass balance. Such work could continue the studies along the objectives of this dissertation and extend them.

Applications and transfer to additional field data sets

In-situ ice thickness and snow depth measurements are generally difficult to collect on very thin ice and heavily deformed ice. Most measurements can only be performed on ice that is accessible by walking which thin ice is mostly not. Thin ice plays a key role in the energy and mass balance of Arctic sea ice due to high levels of radiation underneath. Its role is expected to receive more attention as its fraction is likely to increase in a changing Arctic. The snow depth retrieval derived in **Chapter 3** has the potential to close this gap. However, validating and testing the retrieval with measurements from thin ice is necessary. This can be achieved by applying the retrieval to the measurements of the refreezing lead and thin ice presented in **Chapter 5**.

During the recently completed MOSAiC drift expedition (**Section 1.4**, **Publication 9**) year-round observations of snow depth, melt ponds, leads, and under-ice radiation were collected

for different ice types using well established as well as new instruments and methods. This comprehensive data set is well suited to generalize the three studies presented in this dissertation (**Chapters 3**, **4**, and **5**). Examples are giving in the following paragraphs. Beyond the MOSAiC data set, other more targeted *in-situ* observations could help to extend the findings to other sea-ice, snow, and surface conditions.

The findings achieved in **Chapter 4** are limited to a small study area (100 m x 100 m) and to small melt ponds (**Figure 4.1**). During MOSAiC, observations of melt ponds were made from their formation in early summer to their refreezing and snow-cover in early autumn and from different sizes ranging from narrow and shallow to wide and deep. The hypothesis of a thicker snow-cover on melt ponds and the resulting lower levels of under-ice radiation could be validated and supported. This can strengthen the hypothesis that such a situation is wide-spread in the Arctic, possibly resulting in strong implications for ocean heat content, thermodynamic ice growth, and ice-and ocean-associated ecosystem.

Time series of surface elevation from the airborne laser scanner with a spatial resolution of 0.5 m might help to constrain the uncertainty in the variability of under-ice radiation, in particular of the measurements presented in **Chapter 5**, and hence, aid a better analysis. From such a data set, especially snow re-distribution can be investigated which if present have a strong effect on the under-ice radiation.

The combination of new ice draft and surface elevation time series measurements would complement the ROV under-ice radiation data. During spring (Leg 3), weekly optics and multi-beam surveys were performed which were separated by three days. Hence, adding the multi-beam data would fill gaps of draft measurements and possible result in a more reliable and robust relationship between thermodynamics and optics.

In addition, a panoramic camera was attached to the crow´s nest of *Polarstern*. Including its high temporal resolution images of the surface can close gaps in the documentation of the evolution of the surface conditions of the refreezing lead. Additional, more orthorectified aerial images are currently being processed which can be used in the future.

Advancing analytical methods and numerical simulations

The snow depth retrieval methods (**Chapter 3**) were only applied to the FYI area in the Lincoln Sea (**Figure 3.1**). However, snow depth and under-ice radiation measurements were also collected for an adjacent snow-covered MYI area. The acoustic signal for the ROV position system was heavily and frequently disturbed due to the undulating bottom topography of the MYI. Thus, only few usable data exist and analyses were not further performed. Nevertheless, it would be worth to investigate whether the few reliable measurements result in a meaningful snow depth retrieval.

The snow depth retrieved could be upscaled to floe-, regional- or Arctic-basin-scales using aerial or satellite images such as Sentinel-2 images together with huge collections of under-ice radiation measurements from ROVs (e.g., Katlein et al., 2019; Castellani et al., 2020) and radiation stations (Nicolaus et al., 2010b). Such data products could ideally be complemented in the near future using AUVs (e.g, Wulff et al., 2016).

The snow depth retrieval could be applied to refrozen, snow-covered melt ponds. It could be validated whether the retrieval achieves a satisfactory accuracy of the snow depth on the melt ponds. Suitable data consist of ROV-based under-ice radiation, and Magnaprobe and laser scanner derived snow depth from, e.g., the AO18 campaign (**Chapter 4**).

The radiative transfer model (**Chapter 3**, **Equation 3.2** or **2.11**) yields also estimates of ice thickness. Even though under-ice radiation is very low underneath pressure ridges (e.g., Katlein et al., 2021), it might be worth to extend this study in such that it attempts to retrieve the ice thickness of ridges. The maximum thickness of ridges is generally underestimated due to their porosity and the lateral extent of the electromagnetically induced secondary magnetic fields (Section 2.3, Haas et al., 2008). This results in a deviation in ice thickness measurements as much as 50% from the true thickness (Haas et al., 2008). The method to estimate the ice thickness using under-ice spectral radiation might be useful in estimating ice thickness of ridges.

Light sources across boundaries are usually neglected in RT modelling of sea ice (**Equations 2.6** and **2.8**). Using a sophisticated RT model (e.g., AccuRT) might reduce the uncertainties in the connection between the thermodynamics and optics of the refreezing lead and thin ice and under-ice radiation (**Chapter 5**). Unfortunately, including light sources across boundaries complicates radiative transfer in sea ice dramatically.

The water and biomass absorption was neglected due clear water conditions and low in-ice chl *a* concentrations (Lange et al., 2019) (**Figure 3.3**, **Equations 3.1** and **3.2**). However, seawater and biomass influence the spectral shape of under-ice radiation through absorption at specific wavelengths (**Figure 2.6**, e.g., Smith and Baker, 1981, Mundy et al., 2007). Measurements of ice-algae chl *a* concentration and spectral absorption coefficients are usually available from ice cores and laboratory measurements. Water absorption can be measured with a hyperspectral extinction sensor attached to the ROV (**Figure 2.13A**, Katlein et al., 2017). Extending the methods as such would make the developed methods applicable to a situation where algae blooms and phytoplankton in the water are present. This would establish interdisciplinary links to biological and ocean optics research.

Possible technological advances

Besides satellite- and airborne-based snow depth retrievals (e.g., Guerreiro et al., 2016; Lawrence et al., 2018; Rostosky et al., 2018; Jutila et al., 2021), the snow depth retrieval developed in

Chapter 3 add another reliable method to estimate snow depth remotely. In case AUVs can start mapping the under-ice radiation on regional scales in the Arctic Ocean, snow depth can be derived and mapped simultaneously. This would be a great asset because measuring snow depth and drilling ice thickness holes at 10-m intervals over large areas is neither appealing nor practical. Nevertheless, high spatial resolution snow depth measurements are crucial because snow depth variability is very heterogeneous.

Year-round snow depth retrieval for small enough scales do not exist because during late autumn, winter, and early spring solar radiation is not sufficient or zero. An option to circumvent this limitation is to explore the possibility to actively illuminate the snow cover. A light source with at least the wavelengths 440 nm, 403 nm, 616 nm, and 651 nm should be used as those were identified to be the key wavelengths for snow depth retrieval using under-ice radiation (**Chapter 3**, **Figure 3.3**). Attached to an autonomous measuring system (e.g., radiation station) and co-deployed with a Snow Buoy for reference, such a light source could automatically illuminate the snow and sea-ice surface (e.g., every hour for 5 minutes). The under-ice radiation could be measured using an ROV, AUV, or a radiation station. There exist prototypes of a reflectance probe that uses a laser to actively illuminate the sea-ice and snow interior to investigate the in-ice light field and thus, characterize the spatially and temporally varying IOPs (Perron et al., 2021).

A. Appendix to Chapter 5

This appendix lists the figures of additional under-water images of the refreezing lead not shown in Chapter 5.

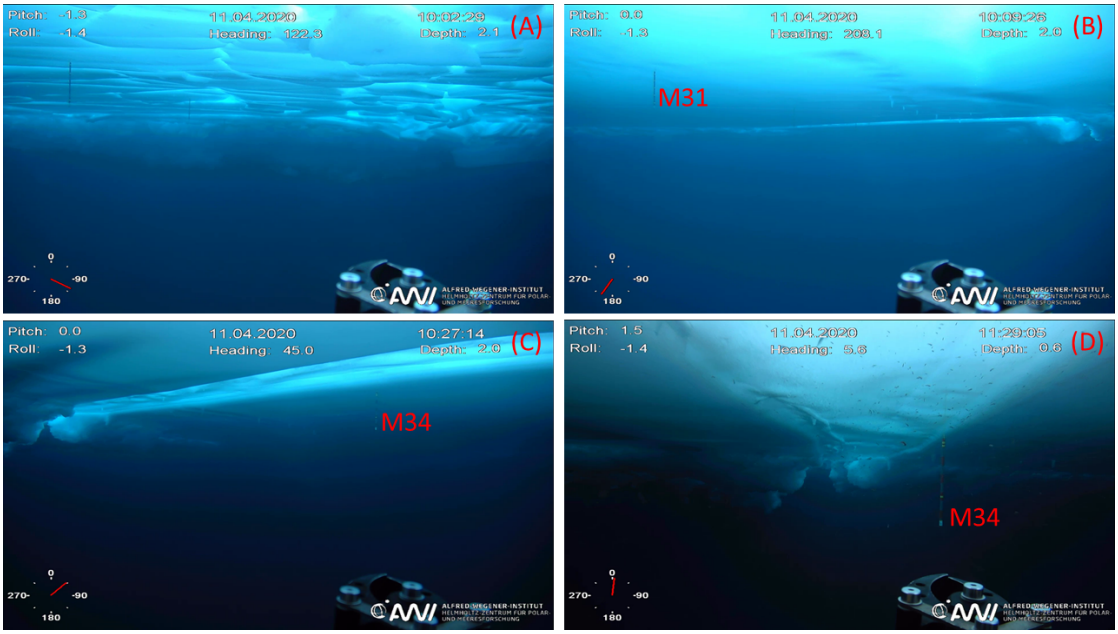

Figure A.1: *ROV HD camera footage of the lead on 11 April.*

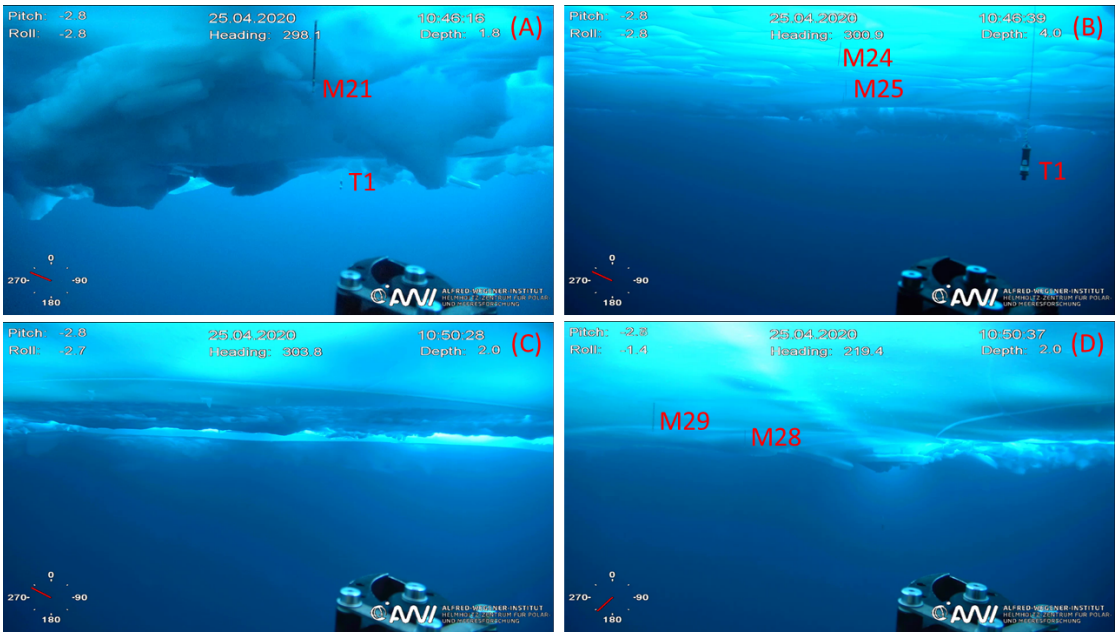

Figure A.2: *ROV HD camera footage of the lead on 25 April.*

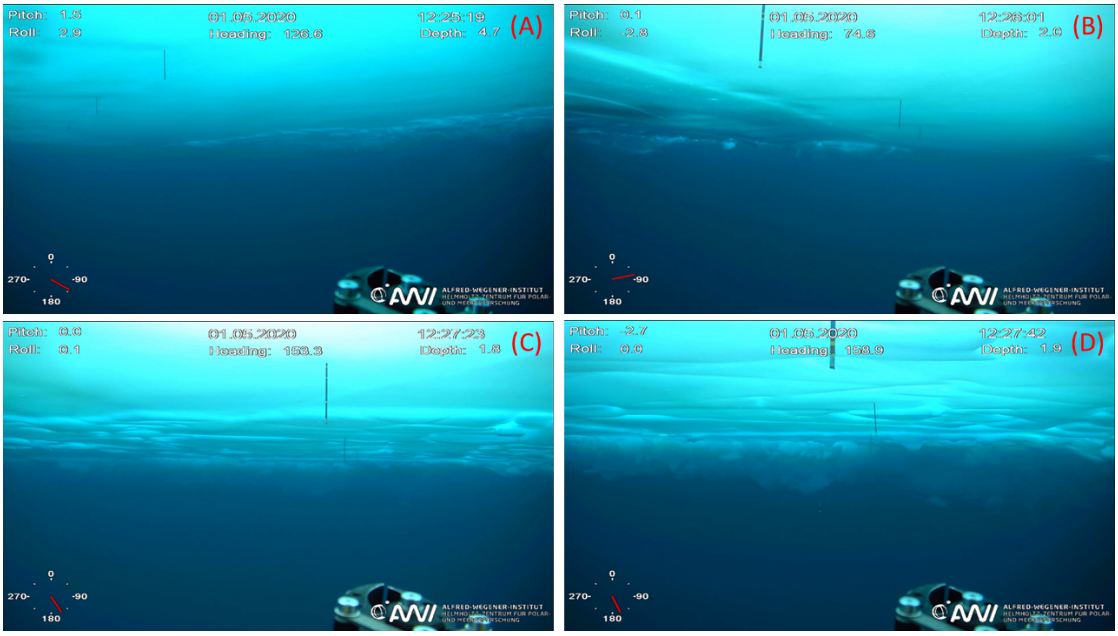

Figure A.3: *ROV HD camera footage of the lead on 1 May.*

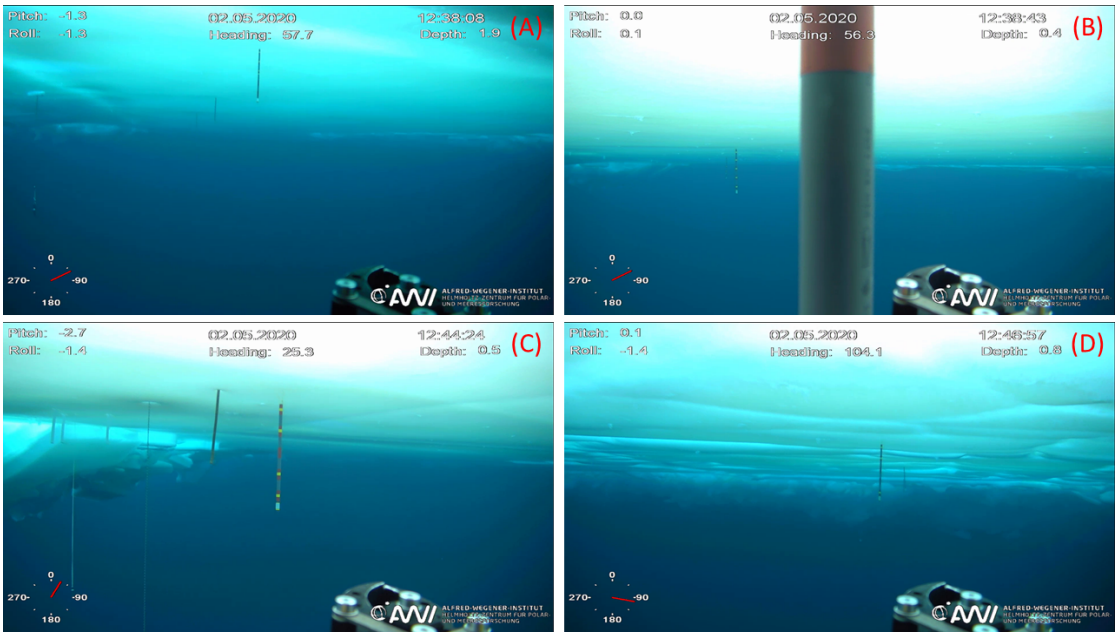

Figure A.4: *ROV HD camera footage of the lead on 2 May.*

Figure A.5: *ROV HD camera footage of the lead on 9 May.*

B. Data sets and other publications

B.1 Data sets

This dissertation has resulted in publication and submission of several data sets that are listed in the following subsections.

Used in Chapter 3

Anhaus, P., Katlein, C., Jutila, A., and Haas, C. Total sea-ice thickness (ice + snow) and snow depth measurements on First-Year-Ice during the ALERT2018 campaign (MAP Last Ice) in May 2018, doi:10.1594/PANGAEA.932594, 2021.

Anhaus, P., Katlein, C., and Nicolaus, M. Updated solar radiation over and under sea ice during the ALERT2018 campaign (MAP Last Ice) in May 2018, doi:10.1594/PANGAEA.930289, 2021.

Nicolaus, M., **Anhaus, P.**, Katlein, C. Solar radiation over and under sea ice and drift of sea ice from autonomous measurements from radiation station 2018R23, deployed during Alert_MAPLI18, doi:10.1594/PANGAEA.936597, in review, 2021.

Anhaus, P., Katlein, C., and Nicolaus, M. Solar radiation over and under sea ice during the ALERT2018 campaign (MAP Last Ice) in May 2018, doi:10.1594/PANGAEA.901247, 2019.

Used in Chapter 4

Anhaus, P., Katlein, C., and Hoppmann, M. Total sea-ice thickness (ice + snow) and snow depth measurements on melt-pond covered Multi-Year-Ice during the Oden AO2018 campaign (Arctic Ocean 2018: MOCCHA - ACAS - ICE) Central Arctic / North Pole, doi:10.1594/PANGAEA.934431, 2021.

Anhaus, P., Katlein, C., Hoppmann, M., and Lehnert, L. Aerial images of sea ice during the Oden AO2018 campaign (Arctic Ocean 2018: MOCCHA - ACAS - ICE) Central Arctic / North Pole drift station in 2018 on IB ODEN, doi:10.5281/zenodo.5119094, 2021.

Anhaus, P., Katlein, C., Hoppmann, M., and Nicolaus, M. Solar radiation over and under sea ice during the Oden AO2018 campaign (Arctic Ocean 2018: MOCCHA - ACAS - ICE) Central Arctic / North Pole drift station in 2018 on IB ODEN, doi:10.1594/PANGAEA.925698, 2020.

Used in Chapter 5

Nicolaus, M., **Anhaus, P.**, Arndt, S., Katlein, C., Krampe, D., Lange, B. A., Matero, I., Regnery, J., Rohde, J., Schiller, M. Spectral solar radiation over and under sea ice during the MOSAiC campaign 2019/20, doi:10.1594/PANGAEA.935688, in review, 2021.

Not used within this dissertation

Bliss, A., Hutchings, J., Anderson, P., **Anhaus, P.**, Belter, H. J. et al. Raw files for sea ice drift tracks from the Distributed Network of autonomous buoys deployed during the Multidisciplinary drifting Observatory for the Study of Arctic Climate (MOSAiC) expedition 2019 - 2021. Arctic Data Center, doi:10.18739/A2KD1QM54, 2021.

Smith, M., Light, B., Perovich, D. K., Webster, M., **Anhaus, P.** et al. Broadband albedo measurements of the sea ice surface during the Multidisciplinary drifting Observatory for the Study of Arctic Climate (MOSAiC) campaign in the Central Arctic Ocean, April – September 2020. Arctic Data Center, doi:10.18739/A2KK94D36, 2021.

Smith, M., Light, B., Perovich, D. K., Webster, M., **Anhaus, P.** et al. Spectral albedo measurements of the sea ice surface during the Multidisciplinary drifting Observatory for the Study of Arctic Climate (MOSAiC) campaign in the Central Arctic Ocean, April – September 2020. Arctic Data Center, doi:10.18739/A2FT8DK8Z, 2021.

Smith, M., Light, B., Perovich, D. K., Webster, M., **Anhaus, P.** et al. Photos of the sea ice surface corresponding to surface albedo datasets collected during the Multidisciplinary drifting Observatory for the Study of Arctic Climate (MOSAiC) campaign in the Central Arctic Ocean, April – September 2020. Arctic Data Center, doi:10.18739/A2B27PS3N, 2021.

Katlein, C., **Anhaus, P.**, Matero, I., and Nicolaus, M. Secchi depths measured during the MOSAiC expedition, doi:10.1594/PANGAEA.929535, 2021.

Katlein, C., **Anhaus, P.**, Matero, I., and Nicolaus, M. Sea ice draft and acoustic backscatter (240kHz) raw data derived from multibeam sonar during the ROV BEAST dive PS122/2_18-19, doi:10.1594/PANGAEA.917498, 2020.

B.2 Other publications

The following publications represent co-author contributions and are not included in this dissertation. Nonetheless, the research carried out in those publications help to understand the relationships between surface and optical properties of Arctic sea ice in more detail. In particular, measurements of under-ice radiation collected by myself provided auxiliary data for biological studies and strengthened interdisciplinary links to physical and biological oceanography.

Publication 4

Lange, B. A., Haas, C., Charette, J., Katlein, C., Campbell, K., Duerksen, S., Coupel, P., **Anhaus, P.**, Jutila, A., Tremblay, P. O. G., Carlyle, C. G., and Michel, C. (2019): Contrasting ice algae and snow-dependent irradiance relationships between first-year and multiyear sea ice, *Geophysical Research Letters*, 46, doi:10.1029/2019GL082873.

Contribution: I participated in the field work and collected and processed under-ice radiation measurements using a remotely operated vehicle (ROV). Those measurements are central for this publication. I provided feedback, commented, and edited text, in particular paragraphs concerning under-ice radiation.

Abstract: During the 2018 Multidisciplinary Arctic Program-Last Ice in the Lincoln Sea, we sampled 45 MYI and 34 FYI cores, combined with snow depth, ice thickness, and transmittance surveys from adjacent level FYI and undeformed MYI. FYI sites show a decoupling between bottom-ice chl *a* and snow depth; however, MYI showed a significant correlation between ice-algal chl *a* biomass and snow depth. Topographic control of the snow cover resulted in greater spatiotemporal variability of the snow over the level FYI, and consequently transmittance, compared to MYI with an undulating surface. The coupled patterns of snow depth, transmittance, and chl *a* indicate that MYI provides an environment with more stable light conditions for ice algal growth. The importance of sea ice surface topography for ice algal habitat underpins the potential ecological changes associated with projected increased ice dynamics and deformation.

Publication 5

Schanke, N. L., Bolinesi, F., Mangoni, O., Katlein, C., **Anhaus, P.**, Hoppmann, M., Lee, P. A., and DiTullio, G. R. (2020): Biogeochemical and ecological variability during the late summer–early autumn transition at an ice-floe drift station in the Central Arctic Ocean, *Limnology and Oceanography*, 66, doi:10.1002/lno.11676.

Contribution: I participated in the field work and collected and processed under-ice radiation measurements using an ROV. I provided feedback, commented, and edited text, in particular paragraphs concerning under-ice radiation.

Abstract: As the annual expanse of Arctic summer ice-cover steadily decreases, concomitant biogeochemical and ecological changes in this region are likely to occur. Because the central Arctic Ocean is often nutrient and light limited, it is essential to understand how environmental changes will affect productivity, phytoplankton species composition, and ensuing changes in biogeochemistry in the region. During the transition from late summer to early autumn, water column sampling of various biogeochemical parameters was conducted along an ice-floe drift station near the North Pole. Our results show that as the upper water column stratification weakened during the late summer–early autumn transition, nutrient concentrations, particulate dimethylsulfoniopropionate ($DMSP_p$) levels, photosynthetic efficiency, and biological productivity, as estimated by $\Delta O_2/Ar$ ratios, all decreased. Chemotaxonomic (CHEMTAX) analysis of phytoplankton pigments revealed a taxonomically diverse picoautotrophic community, with Chl c_3-containing flagellates and the prasinophyte, *Pyramimonas* spp., as the most abundant groups, comprising $\sim$ 30% and 20% of the total Chl *a* (TChl *a*) biomass, respectively. In contrast to previous studies, the picoprasinophyte, *Micromonas* spp., represented only 5% to 10% of the TChl *a* biomass. Of the nine taxonomic groups identified, DMSPp was most closely associated with *Pyramimonas* spp., a Chl *b*-containing species not usually considered a high DMSP producer. As the extent and duration of open, ice-free waters in the central Arctic Ocean progressively increases, we suggest that enhanced light transmission could potentially expand the ecological niche of *Pyramimonas* spp. in the region.

Publication 6

Katlein, C., Mohrholz, V., Sheikin, I., Itkin, P., Divine, D. V., Stroeve, J., Jutila, A., Krampe, D., Shimanchuk, E., Raphael, I., Rabe, B., Kuznetov, I., Mallet, M., Liu, H., Hoppmann, M., Fang, Y.-C., Dumitrascu, A., Arndt, S., **Anhaus, P.**, Nicolaus, M., Matero, I., Oggier, M., Eicken, H., and Haas, C. (2020): Platelet Ice Under Arctic Pack Ice in Winter, *Geophysical Research Letters*, 47, doi:10.1029/2020GL088898.

Contribution: I assisted in preparing the ROV for the field work and contributed to data acquisition. I provided feedback, commented, and edited text.

Abstract: The formation of platelet ice is well known to occur under Antarctic sea ice, where subice platelet layers form from supercooled ice shelf water. In the Arctic, however, platelet ice formation has not been extensively observed, and its formation and morphology currently remain enigmatic. Here, we present the first comprehensive, long-term in situ observations of a decimeter thick subice platelet layer under free-drifting pack ice of the central Arctic in winter. Observations carried out with an ROV during the midwinter Leg of the MOSAiC drift expedition provide clear evidence of the growth of platelet ice layers from supercooled water present in the ocean mixed layer. This platelet formation takes place under all ice types present during the surveys. Oceanographic data from autonomous observing platforms lead us to

the conclusion that platelet ice formation is a widespread but yet overlooked feature of Arctic winter sea ice growth.

Publication 7

Campbell, K., Matero, I., Bellas, C., Turpin-Jelfs, T., **Anhaus, P.**, Graeve, M. Fripiat, F., Tranter, M., Landy, J. C., Sanchez-Baracaldo, P., Leu, E., Katlein, C., Mundy, C. J., Rysgaard, S., Tedesco, L., Haas, C., and Nicolaus, M. (2022). Monitoring a changing Arctic: Recent advancements in the study of sea ice microbial communities, *Ambio*, doi:10.1007/s13280-021-01658-z.

Contribution: I provided the ROV-based radiation data which are key for this publication. I provided feedback, commented, and edited text.

Abstract: Sea ice continues to decline across many regions of the Arctic, with remaining ice becoming increasingly younger and more dynamic. These changes alter the habitats of microbial life that live within the sea ice, which support healthy functioning of the marine ecosystem and provision of resources for human-consumption, in addition to influencing biogeochemical cycles (e.g. air–sea CO_2 exchange). With the susceptibility of sea ice ecosystems to climate change, there is a pressing need to fill knowledge gaps surrounding sea ice habitats and their microbial communities. Of fundamental importance to this goal is the development of new methodologies that permit effective study of them. Based on outcomes from the DiatomARCTIC project, this paper integrates existing knowledge with case studies to provide insight on how to best document sea ice microbial communities, which contributes to the sustainable use and protection of Arctic marine and coastal ecosystems in a time of environmental change.

Publication 8

Campbell, K., Lange, B. A., Landy, J. C., Katlein, C., Nicolaus, M., **Anhaus, P.**, Matero, I., Gradinger, R., Charette, J., Duerksen, S., Tremblay, P., Rysgaard, S., Tranter, M., Haas, C., and Michel, C. (2022): Net heterotrophy in High Arctic first-year and multi-year spring sea ice, *Elementa: Science of the Anthropocene*, 10(1), doi:10.1525/elementa.2021.00040.

Contribution: I participated in the field work and collected and processed under-ice radiation measurements using an ROV. Those measurements are central for this publication. I provided feedback, commented, and edited text, in particular paragraphs concerning under-ice radiation.

Abstract: The net productivity of sea ice is determined by the physical and geochemical characteristics of the ice–ocean system and the activity of organisms inhabiting the ice. Differences in habitat suitability between first-year and multi-year sea ice can affect the ice algal community composition and acclimation state, introducing considerable variability to primary production within each ice type. In this study, we characterized the biogeochemical variability between adjacent first-year and multi-year sea ice floes in the Lincoln Sea of the Canadian High Arctic, during the May 2018 Multidisciplinary Arctic Program—Last Ice sampling campaign. Com-

bining measurements of transmitted irradiance from a remotely operated underwater vehicle with laboratory-based oxygen optode incubations, this work shows widespread heterotrophy (net oxygen uptake) in the bottom 10 cm of both ice types, particularly in thick multi-year ice (>2.4 m) and early morning of the 24-h day. Algal acclimation state and species composition varied between ice types despite similar net community production due to widespread light and nutrient limitation. The first-year ice algal community was increasingly dominated over spring by the potentially toxin-producing genus *Pseudonitzschia* that was acclimated to high and variable light conditions characteristic of a thinner ice habitat with mobile snow cover. In comparison, the multi-year ice harbored more shade-acclimated algae of mixed composition. This work highlights the potential for heterotrophy in sea ice habitats of the High Arctic, including first measurements of such O_2-uptake in multi-year ice floes. Observed differences in photophysiology between algae of these sea ice types suggests that a shift toward higher light availability and a younger sea ice cover with climate change does not necessarily result in a more productive system. Instead, it may favor future sea ice algal communities of different species composition, with lower photosynthetic potential but greater resilience to stronger and more variable light conditions.

Publication 9

Nicolaus, M., Perovich, D. K., Spreen, G., Granskog, M. A., Albedyll L., Angelopoulos M., **Anhaus, P.**, et al. (2022): Overview of the MOSAiC expedition: Snow and sea ice, *Elementa: Science of the Anthropocene*, 9(1), doi:10.1525/elementa.2021.000046.

Contribution: I participated in the field work and collected key data. I provided input for text and figures mainly related to ROV-based optical and ice draft measurements. I provided feedback, commented, and edited text, in particular paragraphs describing and presenting optical measurements.

Abstract: Year-round observations of the snow and ice properties and processes that govern the ice pack evolution and its interaction with the atmosphere and the ocean were conducted during the Multidisciplinary drifting Observatory for the Study of Arctic Climate (MOSAiC) expedition of the research vessel Polarstern in the Arctic Ocean from October 2019 to September 2020. The overall aim of the snow and sea ice observations during MOSAiC was to characterize the physical properties of the snow and ice cover in the inner Arctic over an entire annual cycle. This objective was achieved by detailed observations of physical properties, and of energy and mass balance of snow and ice. By studying snow and sea ice dynamics over nested spatial scales from centimetres to tens of kilometres, the variability across scales is considered. Overall, the snow and sea ice observational program during MOSAiC was the most comprehensive so far. The collected data will help to improve numerical process and climate models, and to establish and validate novel satellite remote sensing methods. Here, we focus on

describing the measurements conducted within the Central Observatory, which extended up to three kilometres from Polarstern. Linkages to accompanying airborne measurements, satellite observations, and results of numerical models are discussed. It is concluded that the highly variable snow cover needs to be considered in more detail (in observations and models) to better understand feedback processes. Furthermore, a number of critical ice-ocean interface processes were observed in detail, likely guiding upcoming research with respect to the changing Arctic sea ice.

Publication 10

Light, B., Smith, M. M., Perovich, D. K., Webster, M. A., Holland, M., Linhardt, F., Raphael, I. A., Clemens-Sewall, D., MacFarlane, A., **Anhaus, P.**, and Bailey, D. (2020): Arctic sea ice albedo: spectral composition, spatial heterogeneity, and temporal evolution observed during the MOSAiC drift, *Elementa: Science of the Anthropocene*, in review.

Contribution: I participated in the field work and collected broadband albedo measurements.

Abstract: The albedo of the Arctic sea ice cover is key to understanding and simulating Earth's shortwave energy budget. Spectral and broadband albedos of Arctic sea ice were spatially and temporally sampled by surface observers along individual survey lines throughout the sunlit season (April - September, 2020) during the Multidisciplinary drifting Observatory for the Study of Arctic Climate (MOSAiC) experiment. The seasonal evolution of albedo for the MOSAiC year was constructed from spatially averaged broadband albedo values for each line. Specific locations were identified as representative of individual ice surface types, including accumulated dry snow, melting snow, bare and melting ice, melting and refreezing ponded ice, and sediment-laden ice. Compared with results from previous field efforts, the spectral albedo of thick, bare, melting sea ice showed invariance across location, decade, and ice type. In particular, the albedo of bare, melting seasonal ice was indistinguishable from that of second-year ice, suggesting that highly scattering surface layers are a robust and stabilizing feature of bare, melting ice. In contrast, the albedo of ponded ice was highly variable at visible wavelengths. Notable temporal changes in albedo were documented during melt and freeze onset, the formation of melt ponds on ice, and the summer melt evolution of sediment-laden ice. The areal-averaged seasonal progression of total albedo recorded during MOSAiC showed remarkable similarity to that recorded 22 years prior on multiyear ice during the Surface Heat Budget of the Arctic Ocean (SHEBA) expedition. While model simulations show considerable agreement with the observed seasonal albedo progression, disparities suggest the need to improve how the albedo of both ponded ice and a thinner melting ice cover are simulated.

Acknowledgments

First and foremost, I want to thank Dr. Marcel Nicolaus and Dr. Christian Katlein for their outstanding supervision and support throughout these last years. I have learned so much from you professionally. I am also thankful to Prof. Dr. Christian Haas, who took me on as his PhD student, agreed to be the first reviewer of my dissertation, and gave critical and constructive comments whenever they were needed. You also gave me the freedom to develop this project for myself, for which I am extremely grateful. Prof. Dr. Torsten Kanzow is very much acknowledged for agreeing to be the second reviewer of this dissertation.

I am most thankful for several great opportunities to participate in field work, cruises, a summer school, workshops, and conferences without those this dissertation would not have been possible and would have only be half as much fun.

For sharing offices, cabins, and hotel rooms, I want to thank Arttu Jutila, Louisa von Hülsen, Daniela Krampe, Christian Katlein, Mario Hoppmann, Matthieu Labaste, Niels Fuchs, Ilkka Matero, Lars Kaleschke, Robert Ricker, Marc-Antoine Bansept, and Emiliano Cimoli.

Special thanks goes to Arttu Jutila in particular and to Jakob Belter for taking their time to provide constructive feedback on parts of this dissertation. Very helpful were also discussions on spectral radiation measurements with Ran Tao. Thanks also to Kathrin Riemann-Campe for her support in preparing and uploading buoy data.

A profound thank you to all my former and current colleagues. I was very comfortable at AWI and I want to thank you for it! I am thankful for the great people who supported the expeditions I was fortunate enough to join: the station staff of the Canadian Forces Station in Alert, the Swedish ship and helicopter crews on RV *Oden*, the German ship and Dutch, French, Italian helicopter crews on RV *Polarstern*, and the numerous people involved in the organisation and planning of these campaigns. I enjoyed in particular the PhD summer school on the Canadian icebreaker CCGS *Amundsen* in Baffin Bay supported by Sentinel North and University Laval, Quebec City, Quebec, Canada. During this time, I had not only the opportunity to get deep insights into Arctic marine ecosystems, but also to get in touch and learn about indigenous cultures in the Arctic.

I am very grateful for the financial support and the great opportunities for further education

provided by the POLMAR graduate school. My thank goes also to the DiatomARCTIC community.
Lastly, I want to express my deepest gratitude to my family and especially to my girlfriend, Linda. Thank you!

Nomenclature

Acronyms

ACAS Arctic Climate Across Scales

ACC Advanced cosine collector

ALS Airborne laser scanner

AO18 Arctic Ocean 2018 MOCCHA – ACAS – ICE campaign

AOP Apparent optical property

ARC Advanced radiance collector

AUV Automatic underwater vehicle

AWI Alfred-Wegener-Institut Helmholtz-Zentrum für Polar- und Meeresforschung

BB Broadband

BMBF Bundesministerium für Bildung und Forschung

CAO Changing Arctic Ocean

Chl *a* Chlorophyll *a*

CTD Conductivity, temperature, depth

Diatom-ARCTIC Diatom Autecological Responses with Changes To Ice Cover

EM31-SH Electromagnetic induction sounding device

FDD Freezing-degree day

FYI First-Year Ice

GEM Ground-based electromagnetic induction sounding device

ICE International Cooperative Effort, on ice work

IOP Inherent optical property

IPCC Intergovernmental Panel for Climate Change

MAPLI18 Multidisciplinary Arctic Program – Last Ice Area 2018 campaign

MATLAB Matrix laboratory

MBS Multi-beam sonar

MOCCHA Microbiology-Ocean-Cloud-Coupling in the High Arctic

MOSAiC Multidisciplinary drifting Observatory for the Study of Arctic Climate

MYI Multi-year ice

NDI Normalized difference indices

NERC Natural Environment Research Council

PAR Photosynthetically active radiation

RMSE Root mean square error

ROV Remotely operated vehicle

RT Radiative transfer

RV Research vessel

SSL Surface-scattering layer

SYI Second-year ice

TLS Terrestrial laser scanner

Symbols

α Albedo

β Opening angle of radiometer

Γ Freezing-degree days

κ_i Thermal conductivity of sea ice

κ_s Thermal conductivity of snow

λ Wavelength

σ Scattering coefficient

Θ	Nadir angle
a	Absorption coefficient
D	Distance to the sea-ice bottom
$d\Omega$	Differential element of solid angle
d_i	Sea-ice thickness
d_s	Snow depth
dA	Differential element of area
E_S	Incident solar irradiance
f	Frequency
F_C	Conductive heat flux
$F_L \downarrow$	Incident solar longwave flux
$F_L \uparrow$	Outgoing solar longwave flux
F_{OHF}	Ocean heat flux
k_i	Extinction coefficient of sea ice
k_s	Extinction coefficient of snow
N	Number of measurements
n	Refractive index
R, r	Radius
R_P	Pearson correlation coefficient
S	Salinity
T	Temperature
T_f	Freezing temperature of seawater
t_f	Transflectance
t_m	Transmittance

List of Figures

List of Tables

Bibliography

Aagaard, K., Swift, J., and Carmack, E.: Thermohaline Circulation in the Arctic Mediterranean Seas, Journal of Geophysical Research: Oceans, 90, doi: 10.1029/JC090iC03p04833, 1985.

Aksenov, Y., Popova, E. E., Yool, A., Nurser, A. J. G., Williams, T. D., Bertino, L., and Bergh, J.: On the future navigability of Arctic sea routes: High-resolution projections of the Arctic Ocean and sea ice, Marine Policy, 75, doi: 10.1016/j.marpol.2015.12.027, 2017.

Ardyna, M., Mundy, C. J., Mills, M. M., Oziel, L., Grondin, L. L., Verin, G., van Dijken, G., Ras, J., Alou-Font, E., Babin, M., Gosselin, M., Tremblay, J., Raimbault, P., Assmy, P., Nicolaus, M., Claustre, H., and Arrigo, K. R.: Environmental drivers of under-ice phytoplankton bloom dynamics in the Arctic Ocean, Elementa: Science of the Anthropocene, 8, doi: 10.1525/elementa.430, 2020.

Arndt, S. and Nicolaus, M.: Seasonal cycle and long-term trend of solar energy fluxes through Arctic sea ice, The Cryosphere, 8, doi: 10.5194/tc-8-2219-2014, 2014.

Arndt, S., Meiners, K. M., Ricker, R., Krumpen, T., Katlein, C., and Nicolaus, M.: Influence of snow depth and surface flooding on light transmission through Antarctic pack ice, Journal of Geophysical Research: Oceans, 122, doi: 10.1002/2016jc012325, 2017.

Arrigo, K. R.: Sea ice ecosystems, Annual Review of Marine Science, 6, doi: 10.1146/annurev-marine-010213-135103, 2014.

Arrigo, K. R., Sullivan, C. W., and Kremer, J. N.: A bio-optical model of Antarctic sea ice, Journal of Geophysical Research, 96, doi: 10.1029/91jc00455, 1991.

Assmy, P., Fernandez-Mendez, M., Duarte, P., Meyer, A., Randelhoff, A., Mundy, C. J., Olsen, L. M., Kauko, H. M., Bailey, A., Chierici, M., Cohen, L., Doulgeris, A. P., Ehn, J. K., Fransson, A., Gerland, S., Hop, H., Hudson, S. R., Hughes, N., Itkin, P., Johnsen, G., King, J. A., Koch, B. P., Koenig, Z., Kwasniewski, S., Laney, S. R., Nicolaus, M., Pavlov, A. K., Polashenski, C. M., Provost, C., Rosel, A., Sandbu, M., Spreen, G., Smedsrud, L. H., Sundfjord, A., Taskjelle, T., Tatarek, A., Wiktor, J., Wagner, P. M., Wold, A., Steen, H., and Granskog, M. A.: Leads in

Arctic pack ice enable early phytoplankton blooms below snow-covered sea ice, Scientific Reports, 7, doi: 10.1038/srep40850, 2017.

AWI: Polar Research and Supply Vessel POLARSTERN operated by the Alfred-Wegener-Institute, Journal of large-scale research facilities JLSRF, 3, doi: 10.17815/jlsrf-3-163, 2017.

Baker, K. S. and Smith, R. C.: Bio-optical classification and model of natural waters, Limnology and Oceanography, 27, doi: 10.4319/lo.1982.27.3.0500, 1982.

Belter, H. J., Krumpen, T., Janout, M. A., Ross, E., and Haas, C.: An Adaptive Approach to Derive Sea Ice Draft from Upward-Looking Acoustic Doppler Current Profilers (ADCPs), Validated by Upward-Looking Sonar (ULS) Data, Remote Sensing, 13, doi: 10.3390/rs13214335, 2021.

Bintanja, R.: On the glaciological, meteorological, and climatological significance of Antarctic blue ice areas, Reviews of Geophysics, 37, doi: 10.1029/1999rg900007, 1999.

Campbell, K., Mundy, C. J., Barber, D. G., and Gosselin, M.: Remote Estimates of Ice Algae Biomass and Their Response to Environmental Conditions during Spring Melt, Arctic, 67, doi: 10.14430/arctic4409, 2014.

Carmack, E., Polyakov, I., Padman, L., Fer, I., Hunke, E., Hutchings, J., Jackson, J., Kelley, D., Kwok, R., Layton, C., Melling, H., Perovich, D., Persson, O., Ruddick, B., Timmermans, M., Toole, J., Ross, T., Vavrus, S., and Winsor, P.: Toward quantifying the increasing role of oceanic heat in sea ice loss in the new Arctic, Bulletin of the American Meteorological Society, 96, doi: 10.1175/BAMS-D-13-00177.1, 2015.

Castellani, G., Schaafsma, F. L., Arndt, S., Lange, B. A., Peeken, I., Ehrlich, J., David, C., Ricker, R., Krumpen, T., Hendricks, S., Schwegmann, S., Massicotte, P., and Flores, H.: Large-Scale Variability of Physical and Biological Sea-Ice Properties in Polar Oceans, Frontiers in Marine Science, 7, doi: 10.3389/fmars.2020.00536, 2020.

Chandrasekhar, S.: Radiative Transfer, Dover Publications, Inc., New York, NY, USA, 1960.

Church, J. A., White, N. J., Konikow, L. F., Domingues, C. M., Cogley, J. G., Rignot, E., Gregory, J. M., Van Den Broeke, M. R., Monaghan, A. J., and Velicogna, I.: Revisiting the Earth's sea-level and energy budgets from 1961 to 2008, Geophysical Research Letters, 38, doi: 10.1029/2011GL048794, 2011.

Cimoli, E., Lucieer, V., Meiners, K. M., Chennu, A., Castrisios, K., Ryan, K. G., Lund-Hansen, L. C., Martin, A., Kennedy, F., and Lucieer, A.: Mapping the in situ microspatial distribution of ice algal biomass through hyperspectral imaging of sea-ice cores, Scientific Reports, 10, doi: 10.1038/s41598-020-79084-6, URL https://www.ncbi.nlm.nih.gov/pubmed/33318636, 2020.

Colbeck, S. C.: Sintering and compaction of snow containing liquid water, Philosophical Magazine A, 39, doi: 10.1080/01418617908239272, 1979.

Craig, S. E., Jones, C. T., Li, W. K. W., Lazin, G., Horne, E., Caverhill, C., and Cullen, J. J.: Deriving optical metrics of coastal phytoplankton biomass from ocean colour, Remote Sensing of Environment, 119, doi: 10.1016/j.rse.2011.12.007, 2012.

Dadic, R., Mott, R., Horgan, H. J., and Lehning, M.: Observations, theory, and modeling of the differential accumulation of Antarctic megadunes, Journal of Geophysical Research: Earth Surface, 118, doi: 10.1002/2013jf002844, 2013.

Edström, P.: A Fast and Stable Solution Method for the Radiative Transfer Problem, Society for Industrial and Applied Mathematics Review, 47, doi: 10.1137/S0036144503438718, 2005.

Eguiluz, V. M., Fernandez-Gracia, J., Irigoien, X., and Duarte, C. M.: A quantitative assessment of Arctic shipping in 2010-2014, Scientific Reports, 6, doi: 10.1038/srep30682, 2016.

Ehn, J. K., Papakyriakou, T. N., and Barber, D. G.: Inference of optical properties from radiation profiles within melting landfast sea ice, Journal of Geophysical Research, 113, doi: 10.1029/2007jc004656, 2008.

Ehn, J. K., Mundy, C. J., Barber, D. G., Hop, H., Rossnagel, A., and Stewart, J.: Impact of horizontal spreading on light propagation in melt pond covered seasonal sea ice in the Canadian Arctic, Journal of Geophysical Research, 116, doi: 10.1029/2010jc006908, 2011.

Fetterer, F. and Untersteiner, N.: Observations of melt ponds on Arctic sea ice, Journal of Geophysical Research: Oceans, 103, doi: 10.1029/98jc02034, 1998.

Flocco, D., Feltham, D. L., Bailey, E., and Schroeder, D.: The refreezing of melt ponds on Arctic sea ice, Journal of Geophysical Research: Oceans, 120, doi: 10.1002/2014jc010140, 2015.

Ford, J. D. and Goldhar, C.: Climate change vulnerability and adaptation in resource dependent communities: a case study from West Greenland, Climate Research, 54, doi: 10.3354/cr01118, 2012.

Frey, K. E., Perovich, D. K., and Light, B.: The spatial distribution of solar radiation under a melting Arctic sea ice cover, Geophysical Research Letters, 38, doi: 10.1029/2011gl049421, 2011.

Frezzotti, M., Gandolfi, S., and Urbini, S.: Snow megadunes in Antarctica: Sedimentary structure and genesis, Journal of Geophysical Research, 107, doi: 10.1029/2001jd000673, 2002a.

Frezzotti, M., Gandolfi, S., La Marca, F., and Urbini, S.: Snow dunes and glazed surfaces in Antarctica: new field and remote-sensing data, Annals of Glaciology, 34, doi: 10.3189/172756402781817851, 2002b.

Graversen, R. G., Mauritsen, T., Tjernstrom, M., Kallen, E., and Svensson, G.: Vertical structure of recent Arctic warming, Nature, 451, doi: 10.1038/nature06502, URL https://www.ncbi.nlm.nih.gov/pubmed/18172495, 2008.

Grenfell, T. C.: A theoretical model of the optical properties of sea ice in the visible and near infrared, Journal of Geophysical Research: Oceans, 88, doi: 10.1029/JC088iC14p09723, 1983.

Grenfell, T. C.: A radiative transfer model for sea ice with vertical structure variations, Journal of Geophysical Research, 96, doi: 10.1029/91jc01595, 1991.

Grenfell, T. C. and Maykut, G. A.: The optical properties of ice and snow in the Arctic Basin, Journal of Glaciology, 18, doi: 10.3189/S0022143000021122, 1977.

Grenfell, T. C. and Perovich, D. K.: Radiation absorption coefficients of polycrystalline ice from 400–1400 nm, Journal of Geophysical Research: Oceans, 86, doi: https://doi.org/10.1029/JC086iC08p07447, 1981.

Grenfell, T. C. and Perovich, D. K.: Spectral albedos of sea ice and incident solar irradiance in the southern Beaufort Sea, Journal of Geophysical Research, 89, doi: 10.1029/JC089iC03p03573, 1984.

Grosfeld, K., Treffeisen, R., Asseng, J., Bartsch, A., Bräuer, B., Fritsch, B., Gerdes, R., Hendricks, S., Hiller, W., Heygster, G., Krumpen, T., Lemke, P., Melsheimer, C., Nicolaus, M., Ricker, R., and Weigelt, M.: Online Sea-Ice Knowledge and Data Platform <www.meereisportal.de>, Polarforschung, 85, doi: 10.2312/polfor.2016.011, 2016.

Guerreiro, K., Fleury, S., Zakharova, E., Rémy, F., and Kouraev, A.: Potential for estimation of snow depth on Arctic sea ice from CryoSat-2 and SARAL/AltiKa missions, Remote Sensing of Environment, 186, doi: 10.1016/j.rse.2016.07.013, 2016.

Haas, C.: Sea ice thickness distribution, in: Sea Ice, edited by Thomas, D. N., John Wiley & Sons, Ltd, doi: 10.1002/9781118778371.ch2, 2017.

Haas, C. and Druckenmiller, M.: Ice thickness and roughness measurements, in: Field Techniques for Sea Ice Research, edited by Eicken, H., University of Alaska Press, URL https://epic.awi.de/id/eprint/22664/, 2009.

Haas, C., Gerland, S., Eicken, H., and Miller, H.: Comparison of sea-ice thickness measurements under summer and winter conditions in the Arctic using a small electromagnetic induction device, Geophysics, 62, doi: 10.1190/1.1444184, 1997.

Haas, C., Hendricks, S., and Doble, M.: Comparison of the sea-ice thickness distribution in the Lincoln Sea and adjacent Arctic Ocean in 2004 and 2005, Annals of Glaciology, 44, doi: 10.3189/172756406781811781, 2006.

Haas, C., Pfaffling, A., Hendricks, S., Rabenstein, L., Etienne, J.-L., and Rigor, I.: Reduced ice thickness in Arctic Transpolar Drift favors rapid ice retreat, Geophysical Research Letters, 35, doi: 10.1029/2008gl034457, 2008.

Haas, C., Hendricks, S., Eicken, H., and Herber, A.: Synoptic airborne thickness surveys reveal state of Arctic sea ice cover, Geophysical Research Letters, 37, doi: 10.1029/2010gl042652, 2010.

Haas, C., Beckers, J., King, J., Silis, A., Stroeve, J., Wilkinson, J., Notenboom, B., Schweiger, A., and Hendricks, S.: Ice and Snow Thickness Variability and Change in the High Arctic Ocean Observed by In Situ Measurements, Geophysical Research Letters, 44, doi: 10.1002/2017gl075434, 2017.

Haas, C., Langhorne, P. J., Rack, W., Leonard, G. H., Brett, G. M., Price, D., Beckers, J. F., and Gough, A. J.: Airborne mapping of the sub-ice platelet layer under fast ice in McMurdo Sound, Antarctica, The Cryosphere, 15, doi: 10.5194/tc-15-247-2021, 2021.

Hanson, A.: Studies of the Mass Budget of Arctic Pack-Ice Floes, Journal of Glaciology, 5, doi: 10.3189/S0022143000018694, 1965.

Hendricks, S., Paul, S., and Rinne, E.: ESA Sea Ice Climate Change Initiative (Sea_Ice_cci): Northern hemisphere sea ice thickness from the CryoSat-2 satellite on a monthly grid (L3C), v2.0, Centre for Environmental Data Analysis, doi: 10.5285/ff79d140824f42dd92b204b4f1e9e7c2, 2018.

Henyey, L. G. and Greenstein, J. L.: Diffuse radiation in the galaxy, The Astrophysical Journal, 93, doi: 10.1086/144246, 1941.

Horvat, C., Jones, D. R., Iams, S., Schroeder, D., Flocco, D., and Feltham, D.: The frequency and extent of sub-ice phytoplankton blooms in the Arctic Ocean, Science Advances, 3, doi: 10.1126/sciadv.1601191, 2017.

Hovelsrud, G. K., McKenna, M., and Huntington, H. P.: Marine mammal harvests and other interactions with humans, Ecological Applications, 18, doi: 10.1890/06-0843.1, 2008.

Hunkeler, P. A.: Sea-ice thickness and porosity from multi-frequency electromagnetic induction sounding: Application to the sub-ice platelet layer in Atka Bay, Antarctica, Ph.D. thesis, Jacobs University Bremen, URL `http://nbn-resolving.de/urn:nbn:de:gbv:579-opus-1005381`, 2016.

Hunkeler, P. A., Hoppmann, M., Hendricks, S., Kalscheuer, T., and Gerdes, R.: A glimpse beneath Antarctic sea ice: Platelet layer volume from multifrequency electromagnetic induction sounding, Geophysical Research Letters, 43, doi: 10.1002/2015gl065074, 2016.

Iacozza, J. and Barber, D. G.: Ablation patterns of snow cover over smooth first-year sea ice in the Canadian Arctic, Hydrological Processes, 15, doi: 10.1002/hyp.1037, 2001.

Itkin, P., Spreen, G., Cheng, B., Doble, M., Girard-Ardhuin, F., Haapala, J., Hughes, N., Kaleschke, L., Nicolaus, M., and Wilkinson, J.: Thin ice and storms: Sea ice deformation from buoy arrays deployed during N-ICE2015, Journal of Geophysical Research: Oceans, 122, doi: 10.1002/2016jc012403, 2017.

Jahn, A., Sterling, K., Holland, M. M., Kay, J. E., Maslanik, J. A., Bitz, C. M., Bailey, D. A., Stroeve, J., Hunke, E. C., Lipscomb, W. H., and Pollak, D. A.: Late-Twentieth-Century Simulation of Arctic Sea Ice and Ocean Properties in the CCSM4, Journal of Climate, 25, doi: 10.1175/jcli-d-11-00201.1, 2012.

Jutila, A., King, J., Paden, J., Ricker, R., Hendricks, S., Polashenski, C., Helm, V., Binder, T., and Haas, C.: High-Resolution Snow Depth on Arctic Sea Ice From Low-Altitude Airborne Microwave Radar Data, IEEE Transactions on Geoscience and Remote Sensing, doi: 10.1109/tgrs.2021.3063756, 2021.

Kaartokallio, H., Granskog, M. A., Kuosa, H., and Vainio, J.: Ice in subarctic seas, in: Sea Ice, edited by Thomas, D. N., John Wiley & Sons, Ltd, doi: 10.1002/9781118778371.ch27, 2017.

Katlein, C.: ROV basierte Untersuchung der räumlichen Variabilität der Lichttransmission durch arktisches Meereis im Sommer, Master's thesis, Eberhard-Karls Universität Tübingen, URL `https://epic.awi.de/id/eprint/31748/`, 2012.

Katlein, C., Arndt, S., Nicolaus, M., Perovich, D. K., Jakuba, M. V., Suman, S., Elliott, S., Whitcomb, L. L., McFarland, C. J., Gerdes, R., Boetius, A., and German, C. R.: Influence of ice thickness and surface properties on light transmission through Arctic sea ice, Journal of Geophysical Research: Oceans, 120, doi: 10.1002/2015JC010914, 2015.

Katlein, C., Perovich, D. K., and Nicolaus, M.: Geometric Effects of an Inhomogeneous Sea Ice Cover on the under Ice Light Field, Frontiers in Earth Science, 4, doi: 10.3389/feart.2016.00006, 2016.

Katlein, C., Schiller, M., Belter, H. J., Coppolaro, V., Wenslandt, D., and Nicolaus, M.: A New Remotely Operated Sensor Platform for Interdisciplinary Observations under Sea Ice, Frontiers in Marine Science, 4, doi: 10.3389/fmars.2017.00281, 2017.

Katlein, C., Arndt, S., Belter, H. J., Castellani, G., and Nicolaus, M.: Seasonal Evolution of Light Transmission Distributions Through Arctic Sea Ice, Journal of Geophysical Research: Oceans, 124, doi: 10.1029/2018jc014833, 2019.

Katlein, C., Langelier, J., Ouellet, A., Lévesque-Desrosiers, F., Hisette, Q., Lange, B. A., Lambert-Girard, S., Babin, M., and Thibault, S.: The three-dimensional light field within sea ice ridges, Geophysical Research Letters, 48, doi: 10.1029/2021gl093207, 2021.

Katlein, C., Valcic, L., Lambert-Girard, S., and Hoppmann, M.: New insights into radiative transfer within sea ice derived from autonomous optical propagation measurements, The Cryosphere, 15, doi: 10.5194/tc-15-183-2021, 2021a.

Kauko, H. M., Taskjelle, T., Assmy, P., Pavlov, A. K., Mundy, C. J., Duarte, P., Fernández-Méndez, M., Olsen, L. M., Hudson, S. R., Johnsen, G., Elliott, A., Wang, F., and Granskog, M. A.: Windows in Arctic sea ice: Light transmission and ice algae in a refrozen lead, Journal of Geophysical Research: Biogeosciences, 122, doi: 10.1002/2016jg003626, 2017.

Kovacs, K. M. and Lydersen, C.: Climate change impacts on seals and whales in the North Atlantic Arctic and adjacent shelf seas, Science Progress, 91, doi: 10.3184/003685008X324010, 2008.

Kovacs, K. M., Aguilar, A., Aurioles, D., Burkanov, V., Campagna, C., Gales, N., Gelatt, T., Goldsworthy, S. D., Goodman, S. J., Hofmeyr, G. J. G., Härkönen, T., Lowry, L., Lydersen, C., Schipper, J., Sipilä, T., Southwell, C., Stuart, S., Thompson, D., and Trillmich, F.: Global threats to pinnipeds, Marine Mammal Science, 28, doi: 10.1111/j.1748-7692.2011.00479.x, 2012.

Krishfield, R. A., Proshutinsky, A., Tateyama, K., Williams, W. J., Carmack, E. C., McLaughlin, F. A., and Timmermans, M. L.: Deterioration of perennial sea ice in the Beaufort Gyre from 2003 to 2012 and its impact on the oceanic freshwater cycle, Journal of Geophysical Research: Oceans, 119, doi: 10.1002/2013jc008999, 2014.

Kwok, R.: Arctic sea ice thickness, volume, and multiyear ice coverage: losses and coupled variability (1958–2018), Environmental Research Letters, 13, doi: 10.1088/1748-9326/aae3ec, 2018.

Kwok, R. and Rothrock, D. A.: Decline in Arctic sea ice thickness from submarine and ICESat records: 1958–2008, Geophysical Research Letters, 36, doi: 10.1029/2009GL039035, 2009.

Kwok, R., Cunningham, G. F., Wensnahan, M., Rigor, I., Zwally, H. J., and Yi, D.: Thinning and volume loss of the Arctic Ocean sea ice cover: 2003–2008, Journal of Geophysical Research, 114, doi: 10.1029/2009jc005312, 2009.

Lange, B. A., Katlein, C., Nicolaus, M., Peeken, I., and Flores, H.: Sea ice algae chlorophyll a concentrations derived from under-ice spectral radiation profiling platforms, Journal of Geophysical Research: Oceans, 121, doi: 10.1002/2016jc011991, 2016.

Lange, B. A., Flores, H., Michel, C., Beckers, J. F., Bublitz, A., Casey, J. A., Castellani, G., Hatam, I., Reppchen, A., Rudolph, S. A., and Haas, C.: Pan-Arctic sea ice-algal chl a biomass and suitable habitat are largely underestimated for multiyear ice, Global Change Biology, 23, doi: 10.1111/gcb.13742, 2017.

Lange, B. A., Haas, C., Charette, J., Katlein, C., Campbell, K., Duerksen, S., Coupel, P., Anhaus, P., Jutila, A., Tremblay, P. O. G., Carlyle, C. G., and Michel, C.: Contrasting ice algae and snow-dependent irradiance relationships between landfast first-year and multi-year sea ice, Geophysical Research Letters, 46, doi: 10.1029/2019gl082873, 2019.

Langleben, M. P.: Albedo Measurements of an Arctic Ice Cover From High Towers, Journal of Glaciology, 7, doi: 10.3189/S0022143000031051, 1968.

Lawrence, I. R., Tsamados, M. C., Stroeve, J. C., Armitage, T. W. K., and Ridout, A. L.: Estimating snow depth over Arctic sea ice from calibrated dual-frequency radar freeboards, The Cryosphere, 12, doi: 10.5194/tc-12-3551-2018, 2018.

Lee, S. H., McRoy, C. P., Joo, H. M., Gradinger, R., Cui, H., Yun, M. S., Chung, K. H., Kang, S.-H., Kang, C.-K., Choy, E. J., Son, S., Carmack, E., and Whitledge, T.: Holes in Progressively Thinning Arctic Sea Ice Lead to New Ice Algae Habitat, Oceanography, 24, doi: 10.5670/oceanog.2011.81, 2011.

Leppäranta, M.: A Review of Analytical Models of Sea-Ice Growth, Atmosphere-Ocean, 31, doi: 10.1080/07055900.1993.9649465, 1993.

Light, B., Maykut, G. A., and Grenfell, T. C.: A temperature-dependent, structural-optical model of first-year sea ice, Journal of Geophysical Research, 109, doi: 10.1029/2003jc002164, 2004.

Light, B., Grenfell, T. C., and Perovich, D. K.: Transmission and absorption of solar radiation by Arctic sea ice during the melt season, Journal of Geophysical Research, 113, doi: 10.1029/2006jc003977, 2008.

Light, B., Perovich, D. K., Webster, M. A., Polashenski, C., and Dadic, R.: Optical properties of melting first-year Arctic sea ice, Journal of Geophysical Research: Oceans, 120, doi: 10.1002/2015jc011163, 2015.

Lindsay, R. W., Zhang, J., Schweiger, A., Steele, M., and Stern, H.: Arctic Sea Ice Retreat in 2007 Follows Thinning Trend, Journal of Climate, 22, doi: 10.1175/2008jcli2521.1, 2009.

Lu, P., Leppäranta, M., Cheng, B., Li, Z., Istomina, L., and Heygster, G.: The color of melt ponds on Arctic sea ice, The Cryosphere, 12, doi: 10.5194/tc-12-1331-2018, 2018a.

Lu, P., Cao, X., Wang, Q., Leppäranta, M., Cheng, B., and Li, Z.: Impact of a Surface Ice Lid on the Optical Properties of Melt Ponds, Journal of Geophysical Research: Oceans, 123, doi: 10.1029/2018jc014161, 2018b.

Makshtas, A. P., Shoutilin, S. V., and Andreas, E. L.: Possible dynamic and thermal causes for the recent decrease in sea ice in the Arctic Basin, Journal of Geophysical Research: Oceans, 108, doi: 10.1029/2001JC000878, 2003.

Malmgren, F.: On the properties of sea-ice. Norwegian North Polar Expedition "Maud" 1918–1925, 1927.

Markus, T., Stroeve, J. C., and Miller, J.: Recent changes in Arctic sea ice melt onset, freezeup, and melt season length, Journal of Geophysical Research: Oceans, 114, doi: 10.1029/2009JC005436, 2009.

Maslanik, J. A., Fowler, C., Stroeve, J., Drobot, S., Zwally, J., Yi, D., and Emery, W.: A younger, thinner Arctic ice cover: Increased potential for rapid, extensive sea-ice loss, Geophysical Research Letters, 34, doi: 10.1029/2007gl032043, 2007.

Massom, R. A., Drinkwater, M. R., and Haas, C.: Winter snow cover on sea ice in the Weddell Sea, Journal of Geophysical Research: Oceans, 102, doi: 10.1029/96jc02992, 1997.

Maykut, G. A.: Energy exchange over young sea ice in the central Arctic, Journal of Geophysical Research, 83, doi: 10.1029/JC083iC07p03646, 1978.

Maykut, G. A.: Large-scale heat exchange and ice production in the central Arctic, Journal of Geophysical Research, 87, doi: 10.1029/JC087iC10p07971, 1982.

Maykut, G. A.: The Surface Heat and Mass Balance, in: The Geophysics of Sea Ice, edited by Untersteiner, N., Springer US, Boston, MA, doi: 10.1007/978-1-4899-5352-0_6, 1986.

Maykut, G. A. and Light, B.: Refractive-index measurements in freezing sea-ice and sodium chloride brines, Applied Optics, 34, doi: 10.1364/AO.34.000950, 1995.

McDonald, S., Koulis, T., Ehn, J., Campbell, K., Gosselin, M., and Mundy, C. J.: A functional regression model for predicting optical depth and estimating attenuation coefficients in sea-ice covers near Resolute Passage, Canada, Annals of Glaciology, 56, doi: 10.3189/2015AoG69A004, 2015.

Meier, W. N., Hovelsrud, G. K., van Oort, B. E. H., Key, J. R., Kovacs, K. M., Michel, C., Haas, C., Granskog, M. A., Gerland, S., Perovich, D. K., Makshtas, A., and Reist, J. D.: Arctic sea ice in transformation: A review of recent observed changes and impacts on biology and human activity, Reviews of Geophysics, 52, doi: 10.1002/2013rg000431, 2014.

Meiners, K. M., Arndt, S., Bestley, S., Krumpen, T., Ricker, R., Milnes, M., Newbery, K., Freier, U., Jarman, S., King, R., Proud, R., Kawaguchi, S., and Meyer, B.: Antarctic pack ice algal distribution: Floe-scale spatial variability and predictability from physical parameters, Geophysical Research Letters, 44, doi: 10.1002/2017gl074346, 2017.

Melbourne-Thomas, J., Meiners, K. M., Mundy, C. J., Schallenberg, C., Tattersall, K. L., and Dieckmann, G. S.: Algorithms to estimate Antarctic sea ice algal biomass from under-ice irradiance spectra at regional scales, Marine Ecology Progress Series, 536, doi: 10.3354/meps11396, 2015.

Meredith, M., Sommerkorn, S., Cassotta, C., Derksen, A., and Ekaykin, A.: Polar Regions, in: IPCC Special Report on the Ocean and Cryosphere in a Changing Climate, edited by Pörtner, H.-O., Roberts, D. C., Masson-Delmotte, D. ., Zhai, P., Tignor, M., Poloczanska, E., Mintenbeck, K., Alegría, A., Nicolai, M., Okem, A., Petzold, J., Rama, B., and Weyer, N., in press, URL `https://www.ipcc.ch/srocc/chapter/chapter-3-2/`, 2019.

Merkouriadi, I., Cheng, B., Graham, R. M., Rösel, A., and Granskog, M. A.: Critical Role of Snow on Sea Ice Growth in the Atlantic Sector of the Arctic Ocean, Geophysical Research Letters, 44, doi: 10.1002/2017gl075494, 2017.

Meyer, A., Fer, I., Sundfjord, A., and Peterson, A. K.: Mixing rates and vertical heat fluxes north of Svalbard from Arctic winter to spring, Journal of Geophysical Research: Oceans, 122, doi: 10.1002/2016jc012441, 2017.

Mobley, C. D.: Light and Water: Radiative Transfer in Natural Waters, Academic Press, San Diego, CA, USA, URL `https://www.oceanopticsbook.info/packages/iws_12h/conversion/files/LightandWater.zip`, 1994.

Mundy, C. J., Barber, D. G., and Michel, C.: Variability of snow and ice thermal, physical and optical properties pertinent to sea ice algae biomass during spring, Journal of Marine Systems, 58, doi: 10.1016/j.jmarsys.2005.07.003, 2005.

Mundy, C. J., Ehn, J. K., Barber, D. G., and Michel, C.: Influence of snow cover and algae on the spectral dependence of transmitted irradiance through Arctic landfast first-year sea ice, Journal of Geophysical Research, 112, doi: 10.1029/2006jc003683, 2007.

Nicolaus, M. and Katlein, C.: Mapping radiation transfer through sea ice using a remotely operated vehicle (ROV), The Cryosphere, 7, doi: 10.5194/tc-7-763-2013, 2013.

Nicolaus, M., Hudson, S. R., Gerland, S., and Munderloh, K.: A modern concept for autonomous and continuous measurements of spectral albedo and transmittance of sea ice, Cold Regions Science and Technology, 62, doi: 10.1016/j.coldregions.2010.03.001, 2010a.

Nicolaus, M., Gerland, S., Hudson, S. R., Hanson, S., Haapala, J., and Perovich, D. K.: Seasonality of spectral albedo and transmittance as observed in the Arctic Transpolar Drift in 2007, Journal of Geophysical Research, 115, doi: 10.1029/2009jc006074, 2010b.

Nicolaus, M., Katlein, C., Maslanik, J., and Hendricks, S.: Changes in Arctic sea ice result in increasing light transmittance and absorption, Geophysical Research Letters, 39, doi: 10.1029/2012gl053738, 2012.

Nicolaus, M., Petrich, C., Hudson, S. R., and Granskog, M. A.: Variability of light transmission through Arctic land-fast sea ice during spring, The Cryosphere, 7, doi: 10.5194/tc-7-977-2013, 2013.

Nicolaus, M., Hoppmann, M., Lei, R., Belter, H. J., Fang, Y.-C., and Rohde, J.: Snow height on sea ice, meteorological conditions and drift of sea ice from autonomous measurements from buoy 2019S96, deployed during MOSAiC 2019/20, PANGAEA, doi: 10.1594/PANGAEA.925326, in: Nicolaus et al. (2021): Snow height on sea ice, meteorological conditions and drift of sea ice from autonomous Snow Buoys during MOSAiC 2019/20. PANGAEA, doi: 10.1594/PANGAEA.933742 (dataset in review), 2020.

Nicolaus, M., Hoppmann, M., Arndt, S., Hendricks, S., Katlein, C., Nicolaus, A., Rossmann, L., Schiller, M., and Schwegmann, S.: Snow Depth and Air Temperature Seasonality on Sea Ice Derived From Snow Buoy Measurements, Frontiers in Marine Science, 8, doi: 10.3389/fmars.2021.655446, 2021.

Notz, D. and Worster, M. G.: Desalination processes of sea ice revisited, Journal of Geophysical Research, 114, doi: 10.1029/2008jc004885, 2009.

Olsen, L. M., Laney, S. R., Duarte, P., Kauko, H. M., Fernández-Méndez, M., Mundy, C. J., Rösel, A., Meyer, A., Itkin, P., Cohen, L., Peeken, I., Tatarek, A., Różańska-Pluta, M., Wiktor, J., Taskjelle, T., Pavlov, A. K., Hudson, S. R., Granskog, M. A., Hop, H., and Assmy, P.: The seeding of ice algal blooms in Arctic pack ice: The multiyear ice seed repository hypothesis, Journal of Geophysical Research: Biogeosciences, 122, doi: 10.1002/2016jg003668, 2017.

Overland, J. E., Wang, M., and Salo, S.: The recent Arctic warm period, Tellus A, 60, doi: 10.1111/j.1600-0870.2008.00327.x, 2008.

Pearce, T., Smit, B., Duerden, F., Ford, J. D., Goose, A., and Kataoyak, F.: Inuit vulnerability and adaptive capacity to climate change in Ulukhaktok, Northwest Territories, Canada, Polar Record, 46, doi: 10.1017/s0032247409008602, 2010.

Peeken, I., Primpke, S., Beyer, B., Gütermann, J., Katlein, C., Krumpen, T., Bergmann, M., Hehemann, L., and Gerdts, G.: Arctic sea ice is an important temporal sink and means of transport for microplastic, Nature Communications, 9, doi: 10.1038/s41467-018-03825-5, 2018.

Perovich, D. and Grenfell, T. C.: A theoretical model of radiative transfer in young sea ice, Journal of Glaciology, 28, doi: 10.3189/S0022143000011680, 1982.

Perovich, D. K.: Theoretical Estimates of Light Reflection and Transmission by Spatially Complex and Temporally Varying Sea Ice Covers, Journal of Geophysical Research, 95, doi: 10.1029/JC095iC06p09557, 1990.

Perovich, D. K.: A theoretical model of ultraviolet light transmission through Antarctic Sea ice, Journal of Geophysical Research, 98, doi: 10.1029/93jc02563, 1993.

Perovich, D. K.: The optical properties of sea ice, Monograph, 96-1, URL https://erdc-library.erdc.dren.mil/jspui/bitstream/11681/2648/1/CRREL-Mono-96-1.pdf, 1996.

Perovich, D. K.: On the aggregate-scale partitioning of solar radiation in Arctic sea ice during the Surface Heat Budget of the Arctic Ocean (SHEBA) field experiment, Journal of Geophysical Research: Oceans, 110, doi: 10.1029/2004jc002512, 2005.

Perovich, D. K.: Light reflection and transmission by a temperate snow cover, Journal of Glaciology, 53, doi: 10.3189/172756507782202919, 2007.

Perovich, D. K.: The Changing Arctic Sea Ice Cover, Oceanography, 24, doi: 10.5670/oceanog.2011.68, 2011.

Perovich, D. K.: Sea ice and sunlight, in: Sea Ice, edited by Thomas, D. N., John Wiley & Sons, Ltd, doi: 10.1002/9781118778371.ch4, 2017.

Perovich, D. K. and Govoni, J. W.: Absorption coefficients of ice from 250 to 400 nm, Geophysical Research Letters, 18, doi: https://doi.org/10.1029/91GL01642, 1991.

Perovich, D. K. and Grenfell, T. C.: Laboratory Studies of the Optical Properties of Young Sea Ice, Journal of Glaciology, 27, doi: 10.3189/S0022143000015410, 1981.

Perovich, D. K. and Polashenski, C.: Albedo evolution of seasonal Arctic sea ice, Geophysical Research Letters, 39, doi: 10.1029/2012GL051432, 2012.

Perovich, D. K., Roesler, C. S., and Pegau, W. S.: Variability in Arctic sea ice optical properties, Journal of Geophysical Research: Oceans, 103, doi: 10.1029/97jc01614, 1998.

Perovich, D. K., Grenfell, T. C., Light, B., and Hobbs, P. V.: Seasonal evolution of the albedo of multiyear Arctic sea ice, Journal of Geophysical Research, 107, doi: 10.1029/2000jc000438, 2002a.

Perovich, D. K., Tucker III, W. B., and Ligett, K. A.: Aerial observations of the evolution of ice surface conditions during summer, Journal of Geophysical Research, 107, doi: 10.1029/2000jc000449, 2002b.

Perovich, D. K., Grenfell, T. C., Richter-Menge, J. A., Light, B., Tucker III, W. B., and Eicken, H.: Thin and thinner: Sea ice mass balance measurements during SHEBA, Journal of Geophysical Research, 108, doi: 10.1029/2001jc001079, 2003.

Perovich, D. K., Richter-Menge, J. A., Jones, K. F., and Light, B.: Sunlight, water, and ice: Extreme Arctic sea ice melt during the summer of 2007, Geophysical Research Letters, 35, doi: 10.1029/2008gl034007, 2008.

Perovich, D. K., Grenfell, T. C., Light, B., Elder, B. C., Harbeck, J. P., Polashenski, C., Tucker, W. B., and Stelmach, C.: Transpolar observations of the morphological properties of Arctic sea ice, Journal of Geophysical Research, 114, doi: 10.1029/2008jc004892, 2009.

Perovich, D. K., Jones, K. F., Light, B., Eicken, H., Markus, T., Stroeve, J., and Lindsay, R.: Solar partitioning in a changing Arctic sea-ice cover, Annals of Glaciology, 52, doi: 10.3189/172756411795931543, 2011a.

Perovich, D. K., Richter-Menge, J. A., Jones, K. F., Light, B., Elder, B. C., Polashenski, C., Laroche, D., Markus, T., and Lindsay, R.: Arctic sea-ice melt in 2008 and the role of solar heating, Annals of Glaciology, 52, doi: 10.3189/172756411795931714, 2011b.

Perron, C., Katlein, C., Lambert-Girard, S., Leymarie, E., Guinard, L.-P., Marquet, P., and Babin, M.: Development of a diffuse reflectance probe for in situ measurement of inherent optical properties in sea ice, The Cryosphere, 15, doi: 10.5194/tc-15-4483-2021, 2021.

Persson, O. and Vihma, T.: The atmosphere over sea ice, in: Sea Ice, edited by Thomas, D. N., John Wiley & Sons, Ltd, doi: 10.1002/9781118778371.ch6, 2017.

Petrich, C. and Eicken, H.: Overview of sea ice growth and properties, in: Sea Ice, edited by Thomas, D. N., John Wiley & Sons, Ltd, doi: 10.1002/9781118778371.ch1, 2017.

Petrich, C., Nicolaus, M., and Gradinger, R.: Sensitivity of the light field under sea ice to spatially inhomogeneous optical properties and incident light assessed with three-dimensional Monte Carlo radiative transfer simulations, Cold Regions Science and Technology, 73, doi: 10.1016/j.coldregions.2011.12.004, 2012a.

Petrich, C., Eicken, H., Polashenski, C. M., Sturm, M., Harbeck, J. P., Perovich, D. K., and Finnegan, D. C.: Snow dunes: A controlling factor of melt pond distribution on Arctic sea ice, Journal of Geophysical Research: Oceans, 117, doi: 10.1029/2012jc008192, 2012b.

Pfirman, S., Haxby, W. F., Eicken, H., Jeffries, M., and Bauch, D.: Drifting Arctic sea ice archives changes in ocean surface conditions, Geophysical Research Letters, 31, doi: 10.1029/2004gl020666, 2004.

Polashenski, C., Perovich, D. K., and Courville, Z.: The mechanisms of sea ice melt pond formation and evolution, Journal of Geophysical Research: Oceans, 117, doi: 10.1029/2011jc007231, 2012.

Polyakov, I. V., Timokhov, L. A., Alexeev, V. A., Bacon, S., Dmitrenko, I. A., Fortier, L., Frolov, I. E., Gascard, J.-C., Hansen, E., Ivanov, V. V., Laxon, S., Mauritzen, C., Perovich, D., Shimada, K., Simmons, H. L., Sokolov, V. T., Steele, M., and Toole, J.: Arctic Ocean Warming Contributes to Reduced Polar Ice Cap, Journal of Physical Oceanography, 40, doi: 10.1175/2010jpo4339.1, URL https://journals.ametsoc.org/view/journals/phoc/40/12/2010jpo4339.1.xml, 2010.

Pope, R. M. and Fry, E. S.: Absorption spectrum (380-700 nm) of pure water. II. Integrating Cavity Measurements, Applied Optics, 36, doi: 10.1364/AO.36.008710, 1997.

Rabenstein, L., Hendricks, S., Martin, T., Pfaffhuber, A., and Haas, C.: Thickness and surface-properties of different sea-ice regimes within the Arctic Trans Polar Drift: Data from summers 2001, 2004 and 2007, Journal of Geophysical Research, 115, doi: 10.1029/2009jc005846, 2010.

Rampal, P., Weiss, J., and Marsan, D.: Positive trend in the mean speed and deformation rate of Arctic sea ice, 1979–2007, Journal of Geophysical Research, 114, doi: 10.1029/2008jc005066, 2009.

Richter-Menge, J., Perovich, D., Elder, B. C., Claffey, K., Rigor, I., and Ortmeyer, M.: Ice mass-balance buoys: a tool for measuring and attributing changes in the thickness of the Arctic sea-ice cover, Annals of Glaciology, 44, doi: 10.3189/172756406781811727, 2006.

RIEGL: Operating Processing Software RiSCAN PRO for RIEGL 3D Laser Scanners, RIEGL LMS GmbH, URL http://www.geomaqhen.cl/wp-content/uploads/2016/02/RiSCAN_PRO.pdf, 2013.

Roedel, W. and Wagner, T.: Physik unserer Umwelt: Die Atmosphäre, Springer-Verlag Berlin Heidelberg, doi: 10.1007/978-3-642-15729-5, 2011.

Rostosky, P., Spreen, G., Farrell, S. L., Frost, T., Heygster, G., and Melsheimer, C.: Snow Depth Retrieval on Arctic Sea Ice From Passive Microwave Radiometers—Improvements and Extensions to Multiyear Ice Using Lower Frequencies, Journal of Geophysical Research: Oceans, 123, doi: 10.1029/2018jc014028, 2018.

Röhrs, J., Kaleschke, L., Bröhan, D., and Siligam, P. K.: An algorithm to detect sea ice leads by using AMSR-E passive microwave imagery, The Cryosphere, 6, doi: 10.5194/tc-6-343-2012, 2012.

Rösel, A., Kaleschke, L., and Birnbaum, G.: Melt ponds on Arctic sea ice determined from MODIS satellite data using an artificial neural network, The Cryosphere, 6, doi: 10.5194/tc-6-431-2012, 2012.

Sahanatien, V. and Derocher, A. E.: Monitoring sea ice habitat fragmentation for polar bear conservation, Animal Conservation, 15, doi: 10.1111/j.1469-1795.2012.00529.x, 2012.

Schanke, N. L., Bolinesi, F., Mangoni, O., Katlein, C., Anhaus, P., Hoppmann, M., Lee, P. A., and DiTullio, G. R.: Biogeochemical and ecological variability during the late summer–early autumn transition at an ice-floe drift station in the Central Arctic Ocean, Limnology and Oceanography, 66, doi: 10.1002/lno.11676, 2021.

Schröder, D., Feltham, D. L., Flocco, D., and Tsamados, M.: September Arctic sea-ice minimum predicted by spring melt-pond fraction, Nature Climate Change, 4, doi: 10.1038/nclimate2203, 2014.

Schweiger, A. J., Zhang, J., Lindsay, R. W., and Steele, M.: Did unusually sunny skies help drive the record sea ice minimum of 2007?, Geophysical Research Letters, 35, doi: 10.1029/2008gl033463, 2008.

Serreze, M. C. and Maslanik, J. A.: Arctic precipitation as represented in the NCEPNCAR reanalysis, Annals of Glaciology, 25, doi: 10.3189/S0260305500014403, 1997.

Serreze, M. C., Holland, M. M., and Stroeve, J.: Perspectives on the Arctic's shrinking sea-ice cover, Science, 315, doi: 10.1126/science.1139426, 2007.

Smith, R. C. and Baker, K. S.: Optical properties of the clearest natural waters (200-800 nm), Applied Optics, 20, doi: 10.1364/AO.20.000177, 1981.

SooHoo, J. B., Palmisano, A. C., Kottmeier, S. T., Lizotte, M. P., SooHoo, S. L., and Sullivan, C. W.: Spectral light absorption and quantum yield of photosynthesis in sea ice microalgae and a bloom of Phaeocystis pouchetii from McMurdo Sound, Antarctica, Marine Ecology Progress Series, 39, doi: 10.3354/meps039175, 1987.

Sorensen, D. C.: Newton's Method with a Model Trust-Region Modification, SIAM Journal on Numerical Analysis, 19, doi: 10.1137/0719026, 1982.

Spreen, G., Kaleschke, L., and Heygster, G.: Sea ice remote sensing using AMSR-E 89-GHz channels, Journal of Geophysical Research: Oceans, 113, doi: 10.1029/2005JC003384, 2008.

Spreen, G., Kwok, R., and Menemenlis, D.: Trends in Arctic sea ice drift and role of wind forcing: 1992-2009, Geophysical Research Letters, 38, doi: 10.1029/2011gl048970, 2011.

Steele, M., Zhang, J., and Ermold, W.: Mechanisms of summertime upper Arctic Ocean warming and the effect on sea ice melt, Journal of Geophysical Research, 115, doi: 10.1029/2009JC005849, 2010.

Stroeve, J. and Notz, D.: Changing state of Arctic sea ice across all seasons, Environmental Research Letters, 13, doi: 10.1088/1748-9326/aade56, 2018.

Stroeve, J., Holland, M. M., Meier, W., Scambos, T., and Serreze, M.: Arctic sea ice decline: Faster than forecast, Geophysical Research Letters, 34, doi: https://doi.org/10.1029/2007GL029703, 2007.

Stroeve, J. C., Kattsov, V., Barrett, A., Serreze, M. C., Pavlova, T., Holland, M. M., and Meier, W. N.: Trends in Arctic sea ice extent from CMIP5, CMIP3 and observations, Geophysical Research Letters, 39, doi: 10.1029/2012gl052676, 2012.

Sturm, M. and Holmgren, J.: An Automatic Snow Depth Probe for Field Validation Campaigns, Water Resources Research, 54, doi: 10.1029/2018wr023559, 2018.

Sturm, M. and Massom, R. A.: Snow in the sea ice system: friend or foe?, in: Sea Ice, edited by Thomas, D. N., John Wiley & Sons, Ltd, doi: 10.1002/9781118778371.ch3, 2017.

Sturm, M., Holmgren, J., König, M., and Morris, K.: The thermal conductivity seasonal snow, Journal of Glaciology, 43, doi: 10.3189/S0022143000002781, 1997.

Sturm, M., Morris, K., and Massom, R.: The Winter Snow Cover of the West Antarctic Pack Ice: Its Spatial and Temporal Variability, in: Antarctic Sea Ice: Physical Processes, Interactions and Variability, American Geophysical Union (AGU), doi: 10.1029/AR074p0001, 1998.

Sturm, M., Holmgren, J., and Perovich, D. K.: Winter snow cover on the sea ice of the Arctic Ocean at the Surface Heat Budget of the Arctic Ocean (SHEBA): Temporal evolution and spatial variability, Journal of Geophysical Research, 107, doi: 10.1029/2000jc000400, 2002.

Sturm, M., Maslanik, J. A., Perovich, D., Stroeve, J. C., Richter-Menge, J., Markus, T., Holmgren, J., Heinrichs, J. F., and Tape, K.: Snow Depth and Ice Thickness Measurements From the Beaufort and Chukchi Seas Collected During the AMSR-Ice03 Campaign, IEEE Transactions on Geoscience and Remote Sensing, 44, doi: 10.1109/tgrs.2006.878236, 2006.

Taskjelle, T., Hudson, S. R., Granskog, M. A., Nicolaus, M., Lei, R., Gerland, S., Stamnes, J. J., and Hamre, B.: Spectral albedo and transmittance of thin young Arctic sea ice, Journal of Geophysical Research: Oceans, 121, doi: 10.1002/2015jc011254, 2016.

Taskjelle, T., Granskog, M. A., Pavlov, A. K., Hudson, S. R., and Hamre, B.: Effects of an Arctic under-ice bloom on solar radiant heating of the water column, Journal of Geophysical Research: Oceans, 122, doi: 10.1002/2016JC012187, 2017.

Taylor, B. B., Taylor, M. H., Dinter, T., and Bracher, A.: Estimation of relative phycoerythrin concentrations from hyperspectral underwater radiance measurements–A statistical approach, Journal of Geophysical Research: Oceans, 118, doi: 10.1002/jgrc.20201, 2013.

Thomas, C. W.: On the Transfer of Visible Radiation through Sea Ice and Snow, Journal of Glaciology, 4, doi: 10.3189/S0022143000027921, 1963.

Tyler, J. E. and Smith, R.: Measurements of Spectral Irradiance Underwater, Gordon and Breach, New York, NY, USA, 1970.

Untersteiner, N.: On the Mass and Heat Budget of Arctic Sea Ice, Archiv für Meteorologie, Geophysik und Bioklimatologie, Serie A, 12, doi: 10.1007/BF02247491, 1961.

Van den Broeke, M. and Bintanja, R.: Summertime Atmospheric Circulation in the Vicinity of a Blue Ice Area in Queen Maud Land, Antarctica, Boundary-Layer Meteorology, 72, doi: 10.1007/BF00709002, 1995.

Vaughan, D., Comiso, J., Allison, I., Carrasco, J., Kaser, G., Kwok, R., Mote, P., Murray, T., Paul, F., Ren, J., Rignot, E., Solomina, O., Steffen, K., and Zhang, T.: Observations: Cryosphere, in: Climate Change 2013: The Physical Science Basis. Contribution of Working Group I to the Fifth Assessment Report of the Intergovernmental Panel on Climate Change, edited by Stocker, T., Qin, D., Plattner, G.-K., Tignor, M., Allen, S. K., Boschung, J., Nauels, A., Xia, Y., Bex, V., and Midgley, P., Cambridge University Press, Cambridge, United Kingdom and New York, NY, USA., URL `https://www.ipcc.ch/report/ar5/wg1/`, 2013.

Vüllers, J., Achtert, P., Brooks, I. M., Tjernström, M., Prytherch, J., Burzik, A., and Neely III, R.: Meteorological and cloud conditions during the Arctic Ocean 2018 expedition, Atmospheric Chemistry and Physics, 21, doi: 10.5194/acp-21-289-2021, 2021.

Walsh, J. E.: Cryosphere and Hydrology, in: Arctic Climate Impact Assessment, ACIA Overview report, edited by Symon, C., Cambridge University Press, URL `https://www.amap.no/documents/doc/arctic-arctic-climate-impact-assessment/796`, 2005.

Warren, S. G.: Optical properties of snow, Reviews of Geophysics, 20, doi: 10.1029/RG020i001p00067, 1982.

Warren, S. G., Rigor, E. G., Untersteiner, N., Radionov, V. F., Bryazgin, N. N., Aleksandrov, Y., and Colony, R.: Snow Depth on Arctic Sea Ice, Journal of Climate, 12, doi: 10.1175/1520-0442(1999)012<1814:SDOASI>2.0.CO;2, 1999.

Webster, M. A., Rigor, I. G., Nghiem, S. V., Kurtz, N. T., Farrell, S. L., Perovich, D. K., and Sturm, M.: Interdecadal changes in snow depth on Arctic sea ice, Journal of Geophysical Research: Oceans, 119, doi: 10.1002/2014jc009985, 2014.

Webster, M. A., Rigor, I. G., Perovich, D. K., Richter-Menge, J. A., Polashenski, C. M., and Light, B.: Seasonal evolution of melt ponds on Arctic sea ice, Journal of Geophysical Research: Oceans, 120, doi: 10.1002/2015jc011030, 2015.

Webster, M. A., Gerland, S., Holland, M. M., Hunke, E., Kwok, R., Lecomte, O., Massom, R. A., Perovich, D., and Sturm, M.: Snow in the changing sea-ice systems, Nature Climate Change, 8, doi: 10.1038/s41558-018-0286-7, 2018.

Weller, G.: Radiation flux investigations, in: AIDJEX Bulletin Arctic Ice Dynamics Joint Experiment, URL `http://psc.apl.washington.edu/nonwp_projects/aidjex/toc.html`, 1972.

Weller, G. and Schwerdtfeger, P.: Radiation penetration in antarctic plateau and sea ice, in: Polar Meteorology, World Meteorological Organization Technical Note, 1967.

Willmes, S. and Heinemann, G.: Sea-Ice Wintertime Lead Frequencies and Regional Characteristics in the Arctic, 2003–2015, Remote Sensing, 8, doi: 10.3390/rs8010004, 2016.

Wongpan, P., Meiners, K. M., Langhorne, P. J., Heil, P., Smith, I. J., Leonard, G. H., Massom, R. A., Clementson, L. A., and Haskell, T. G.: Estimation of Antarctic Land-Fast Sea Ice Algal Biomass and Snow Thickness From Under-Ice Radiance Spectra in Two Contrasting Areas, Journal of Geophysical Research: Oceans, 123, doi: 10.1002/2017jc013711, 2018.

Wulff, T., Bauerfeind, E., and von Appen, W.-J.: Physical and ecological processes at a moving ice edge in the Fram Strait as observed with an AUV, Deep Sea Research Part I: Oceanographic Research Papers, 115, doi: 10.1016/j.dsr.2016.07.001, 2016.

Zampieri, L., Kauker, F., Fröhle, J., Sumata, H., Hunke, E. C., and Goessling, H. F.: Impact of Sea-Ice Model Complexity on the Performance of an Unstructured-Mesh Sea-Ice/Ocean Model under Different Atmospheric Forcings, Journal of Advances in Modeling Earth Systems, 13, doi: 10.1029/2020ms002438, 2021.

Declaration – Erklärung

I, Philipp Anhaus, herewith declare, that I

1. have formulated this thesis myself and without the help of others,
2. have not used sources and tools other than those indicated nor aids other than those permissible,
3. have marked the literal or textual taken part of the used words.

I hereby declare that I have not qualified or applied for a doctorate procedure in the past.

I agree to the reviewing of my doctoral thesis with qualified software during the investigation of t e pretence of plagiarism.

Hiermit erkläre ich, Philipp Anhaus, dass ich

1. die vorliegende Dissertation ohne unerlaubte fremde Hilfe angefertigt habe,
2. keine anderen als die von mir angegebenen Quellen und Hilfsmittel benutzt habe,
3. die, den benutzten Werken wörtlich oder inhaltlich entnommenen Stellen als solche kenntlich gemacht hat.

Hiermit versichere ich, dass ich mich keinem Promotionsverfahren unterzogen bzw. ein solches beantragt habe.

Ich bin damit einverstanden, dass eine Überprüfung meiner Dissertation mit qualifizierter Software im Rahmen der Untersuchung von Plagiatsvorwürfen gestattet ist.

Bremerhaven, 11. Oktober 2021 Philipp Anhaus